

# **The synthesis and characterisation of pyrochlore zirconates**

A dissertation submitted to the Faculty of Science, University of the Witwatersrand, in fulfilment of the requirements for the degree Master of Science in Chemistry

**By**

**Thabang Jazyqueen Chiya**

University of the Witwatersrand, Johannesburg. June 2017



## **Declaration**

I declare that this dissertation is my own, unaided work. It is being submitted for the degree Master of Science at the University of the Witwatersrand, Johannesburg. It has not been submitted before for any degree or examination at any other University

---

Thabang Jazyqueen Chiya

June 2017

Supervisor: Prof Dave G. Billing

Co-supervisor: Dr Stuart Miller

# ABSTRACT

In this research project, the synthesis, chemistry and thermoresponsive behavior of pyrochlorates of the structure type  $A_2Zr_2O_7$  (A= La, Sm, Y) were investigated. The materials synthesized were coupled with doped analogues of the structure type  $AA'Zr_2O_7$  where A and A' were 1:1 mixture of La, Sm, Y. Investigating the structural dynamics and thermal behavior of the materials revealed high thermal stability of the materials while some of the doped analogues were unstable with increasing temperatures. The materials were synthesized using the sol-gel route and were all characterized using powder X-ray diffraction (PXRD) coupled with Rietveld refinement for structural refinement and solution. The thermoresponsive behavior was investigated using variable temperature PXRD along with Rietveld refinement for the measurement of thermal expansion coefficients. The doped analogues were also characterized using electron probe micro-analyzer (EPMA) for mapping studies.

The mechanochemical synthesis route was also employed in the synthesis of  $La_2Zr_2O_7$  using a planetary ball mill. This material was also characterized using PXRD both for structure determination and thermoresponsive studies. The ball mill consisted of a stainless steel jar and this had implications on the final product, this is an observation which has never been explored before.

This dissertation consists of 6 chapters. Chapter 1 reviews the scientific literature of pyrochlore type structures, chapter 2 best describes the methods of synthesis and characterization of the materials. Chapter 3 was an investigation of pyrochlore zirconates of the structure type  $A_2Zr_2O_7$  (A= La, Sm, Y), their phase composition, structural determination and thermoresponsive behavior. Chapter 4 describes  $La_2Zr_2O_7$  as synthesized by the wet mechanochemical route; the method was efficient and gave products with a higher percentage yield while showing that the use of a stainless steel pot or balls in a planetary ball mill extracts  $Fe_2O_3$  from the pot or balls. This led to the  $Fe_2O_3$  reacting with  $La_2O_3$  and leading to a perovskite structure type which was present in the final product. Chapter 5 was the investigation of  $LaSmZr_2O_7$ ,  $LaYZr_2O_7$  and  $Sm_YZr_2O_7$ . These were all synthesized using the sol-gel route and characterized using PXRD with Rietveld refinement for structural determination and thermoresponsive behavior studies.

LaSmZr<sub>2</sub>O<sub>7</sub> and LaYZr<sub>2</sub>O<sub>7</sub> were unstable at high temperature while SmYZr<sub>2</sub>O<sub>7</sub> was the only material that possessed stability at high temperatures. The phase compositions of the materials were investigated using EPMA which gave a better overview of what single powder crystals of each of the materials contained. LaSmZr<sub>2</sub>O<sub>7</sub> and LaYZr<sub>2</sub>O<sub>7</sub> which were unstable; revealed that the A<sup>3+</sup> cations were not evenly distributed on the crystals. SmYZr<sub>2</sub>O<sub>7</sub> revealed an even distribution of Sm and Y throughout the crystals. This material was then investigated using variable temperature PXRD and the thermal expansion coefficient (TEC) was determined, this was a first report of the TEC of SmYZr<sub>2</sub>O<sub>7</sub>.

## **DEDICATION**

To my mother and daughter,

Brenda Nomgqibelo Chiya

And

Lonwabo Rethabile Chiya

# ACKNOWLEDGEMENTS

I would like to extend my sincerest thanks and gratitude to my supervisor Professor Dave Billing, you were more than a supervisor and your support will forever echo in the universe.

To Dr Stuart Miller, many thanks for your guidance and support. Live long and prosper!

A big thank you to all my siblings who were present at all times; Sizwe, Pfunzo, Tumelo, Ayanda and Gugu.

I'm grateful to my partner, Nondumiso Magagula, you were awesome throughout the journey of my M.Sc and I thank the universe for you.

To Amogelang for the smile she kept on my face in hard times.

I am thankful to the NRF and DST-CoE for their financial support.

To all my friends and extended family who were part of my life and continue to support me, I thank you.

To the C112 group, many thanks and gratitude

# TABLE OF CONTENTS

DECLARATION.....	I
ABSTRACT.....	II
DEDICATION.....	IV
ACKNOWLEDGEMENTS.....	V
LIST OF FIGURES.....	IX
LIST OF TABLES.....	XII
<b>Chapter 1: Introduction.....</b>	<b>1</b>
<b>1.1 Pyrochlore structure.....</b>	<b>1</b>
<b>1.2 Defect fluorite.....</b>	<b>8</b>
<b>1.3 Properties and applications of pyrochlores and defect fluorites.....</b>	<b>10</b>
<b>1.4 Thermal expansion in pyrochlores and defect fluorites.....</b>	<b>13</b>
<b>1.5 Synthesis of pyrochlores.....</b>	<b>16</b>
<b>1.6 Aims and objectives.....</b>	<b>17</b>
<b>1.7 References.....</b>	<b>18</b>
<b>Chapter 2: Experimental Approach.....</b>	<b>21</b>
<b>2.1 Synthesis.....</b>	<b>21</b>
<b>2.1.1 Sol-gel synthesis.....</b>	<b>21</b>

2.1.2 Wet mechanochemical synthesis.....	22
2.2 Characterization techniques.....	24
2.2.1 Powder X-Ray Diffraction.....	24
2.2.2 Powder X-ray Diffraction instruments.....	26
2.2.3 Energy-dispersive X-ray spectroscopy.....	28
2.3 Data Analysis.....	29
2.3.1 Rietveld refinement.....	30
2.4 References.....	31
<b>Chapter 3: Synthesis and characterization of intrinsic pyrozoirconates of the form <math>A_2Zr_2O_7</math> (A=La, Sm, Y).....</b>	<b>32</b>
3.1 Introduction.....	32
3.2 Experimental.....	33
3.2.1 Materials.....	33
3.2.2 Sol-gel synthesis.....	33
3.3 Results and discussion.....	34
3.4 General conclusions.....	51
3.5 References.....	51
<b>Chapter 4: Mechanochemical synthesis and characterization of <math>La_2Zr_2O_7</math> .....</b>	<b>53</b>
4.1 Introduction.....	53
4.2 Experimental.....	53
4.2.1 Materials.....	53

4.2.2 Wet mechanochemical synthesis .....	54
4.2.3 Characterization techniques .....	54
4.3 Results and discussion .....	55
4.4 General conclusions .....	66
4.5 References .....	66
<b>Chapter 5: Effects of annealing temperature in LaSmZr<sub>2</sub>O<sub>7</sub>, LaYZr<sub>2</sub>O<sub>7</sub> and SmYZr<sub>2</sub>O<sub>7</sub> doped pyrochlores .....</b>	<b>68</b>
5.1 Introduction .....	68
5.2 Experimental approach .....	68
5.2.1 Materials .....	68
5.2.2 Sol-gel synthesis of the doped analogues .....	69
5.2.3 Characterization techniques .....	69
5.3 Results and discussion .....	70
5.4 General conclusions .....	88
5.5 References .....	88
<b>Chapter 6: General conclusions and future work .....</b>	<b>89</b>
6.1 Conclusions .....	89
6.2 Future work .....	90

## List of figures

Figure 1.1: Cubic 1/8 unit cell of a pyrochlore with the Wyckoff positions of the atoms.....	3
Figure 1.2: fluorite unit cell where the red spheres are anions and the yellow spheres represent a cation.....	4
Figure 1.3: The cubic unit cell of an ordered pyrochlore viewed along the a-axis, positional parameter $x=0.375$ . The blue spheres represent the A cation, yellow represents the smaller B cation while the red spheres represent the oxygen anions.....	5
Figure 1.4: Disordered pyrochlore structure viewed along the a-axis, oxygen positional parameter $x=0.3125$ .....	5
Figure 1.5: Visual aids showing the $\text{BO}_6$ polyhedron and their differences for varying $x$ positional parameters Yellow spheres represent the B cation while the red ones represent oxide anions. Part a) shows the $\text{BO}_6$ polyhedron for $x=0.375$ while b) shows the polyhedron for $x=0.3125$ .....	6
Figure 1.6: Unit cell of a defect fluorite. The red spheres represent the $\text{O}^{2-}$ anions occupying the 8c site and the yellow and white spheres represent the A and B cations which occupy the same position.....	8
Figure 1.7: Powder X-Ray diffraction patterns of a pyrochlore (Pyr) and a defect fluorite (DF) obtained using $\text{CuK}_\alpha$ radiation.....	9
Figure 1.8: Stability map of pyrochlores and defect fluorites as predicted by Minervini <i>et al.</i> ....	11
Figure 1.9: Diagram of a solid oxide fuel cell (SOFC) that conducts oxygen ions.....	13
Figure 2.1: Schematic diagram showing how the sol-gel synthesis route works.....	22
Figure 2.2 Planetary ball mill used for mechanochemical synthesis.....	23
Figure 2.3: Schematic diagram showing a zirconia pot and the constituents.....	23
Figure 2.4: Schematic representation that is used for deriving Bragg's law from two parallel planes.....	25
Figure 2.5: Bruker D2 phaser diffractometer equipped with cobalt radiation.....	27
Figure 2.6: The Anton Paar XRK 900 reaction chamber used in a D8 Advance.....	28

Figure 2.7: The CAMECA SX-5-FE Electron Probe Micro-Analyzer.....	29
Figure 3.1 Powder X-ray diffraction pattern of $\text{La}_2\text{Zr}_2\text{O}_7$ at ambient temperature measured at $\lambda = 1.78897 \text{ \AA}$ .....	34
Figure 3.2 PXRD profile plots of $\text{La}_2\text{Zr}_2\text{O}_7$ as refined by Rietveld using TOPAS; the blue plot represents the observed pattern, red shows the calculated plot and grey is the difference plot...35	
Figure 3.3 Cubic unit cell of $\text{La}_2\text{Zr}_2\text{O}_6\text{O}'$ viewed along the a-axis, the 48f x positional parameter is 0.34399. Green spheres represent $\text{La}^{3+}$ the blue spheres are $\text{Zr}^{4+}$ and the red spheres are $\text{O}^{2-}$ ..37	
Figure 3.4: Powder X-ray diffraction pattern of $\text{Sm}_2\text{Zr}_2\text{O}_7$ measured at room temperature, $\lambda= 1.78897 \text{ \AA}$ .....	38
Figure 3.5: PXRD profile plots of $\text{Sm}_2\text{Zr}_2\text{O}_7$ as refined using TOPAS; the blue line is the measured pattern, red is the calculated and grey is the difference between the measured and calculated.....	39
Figure 3.6: Cubic unit cell of $\text{Sm}_2\text{Zr}_2\text{O}_7$ viewed along the a-axis. Green spheres are $\text{Zr}^{4+}$ , yellow spheres represent $\text{Sm}^{3+}$ and red spheres are $\text{O}^{2-}$ ions.....	40
Figure 3.7: Powder X-ray diffraction pattern of $\text{Y}_2\text{Zr}_2\text{O}_7$ at ambient temperature, $\lambda= 1.78897 \text{ \AA}$ .....	41
Figure 3.8 PXRD pattern profile of $\text{Y}_2\text{Zr}_2\text{O}_7$ as refined using TOPAS; blue peak represents the observed pattern, red is the calculated and grey is the difference.....	42
Figure 3.9 Cubic unit cell of $\text{Y}_2\text{Zr}_2\text{O}_7$ with the defect fluorite structure type showing the Wyckoff positions of the ions. For the two toned sphere the blue color represents $\text{Zr}^{4+}$ and the grey part is $\text{Y}^{3+}$ , the red sphere represents $\text{O}^{2-}$ .....	44
Figure 3.10 Variable-temperature patterns of $\text{La}_2\text{Zr}_2\text{O}_7$ recorded from 303 K to 1123 K. This was recorded at 50 K increments using Cu $\text{K}\alpha$ radiation.....	45
Figure 3.11 Lattice parameter against temperature plot for $\text{La}_2\text{Zr}_2\text{O}_7$ with the line used to fit the points.....	46
Figure 3.12 Variable temperature patterns of $\text{Sm}_2\text{Zr}_2\text{O}_7$ measured from 303 K to 1123 K.....	47
Figure 3.13 Lattice parameter against temperature plot of $\text{Sm}_2\text{Zr}_2\text{O}_7$ with the line used to fit the points.....	47
Figure 3.14 Variable temperature patterns of $\text{Y}_2\text{Zr}_2\text{O}_7$ measured from 303 K to 1123 K.....	49
Figure 3.15 Lattice parameter vs temperature line scatter plot for $\text{Y}_2\text{Zr}_2\text{O}_7$ .....	50

Figure 4.1 PXRD pattern of $\text{La}_2\text{Zr}_2\text{O}_7$ as-synthesized before heat treatment, $\lambda = 1.78897 \text{ \AA}$ .....	55
Figure 4.2 PXRD pattern of $\text{La}_2\text{Zr}_2\text{O}_7$ after heat treatment at $1200 \text{ }^\circ\text{C}$ , $\lambda = 1.78897 \text{ \AA}$ .....	56
Figure 4.3 PXRD profile plots of $\text{La}_2\text{Zr}_2\text{O}_7$ with $R_{\text{wp}} = 7.29\%$ , this was fitted with the impurities present.....	57
Figure 4.4 Graphic representations of the materials present in the final product. The structures in alphabetic order represent a) $\text{La}_2\text{Zr}_2\text{O}_7$ with a pyrochlore structure type, b) $\text{ZrO}_2$ , c) $\text{LaFeO}_3$ and d) $\text{La}_2\text{O}_3$ . Red spheres are O atoms, yellow represents Zr, green represents La and brown represents Fe.....	58
Figure 4.5 Variable temperature plots of $\text{La}_2\text{Zr}_2\text{O}_7$ with traces of $\text{ZrO}_2$ , $\text{LaFeO}_3$ and $\text{La}_2\text{O}_3$ measured from $303 \text{ K}$ to $943 \text{ K}$ , $\lambda = 1.5406 \text{ \AA}$ .....	60
Figure 4.6 Zoomed in peaks of all the phases to show peak shifting during the heat treatment...61	
Figure 4.7 Lattice parameter obtained by Rietveld refinement against temperature plot for $\text{La}_2\text{Zr}_2\text{O}_7$ .....	62
Figure 4.8 Variation of the $48f$ x positional parameter as a function of temperature for $\text{La}_2\text{Zr}_2\text{O}_7$ .....	63
Figure 4.9 Bond lengths between Zr and O atoms as a function of the $48f$ x positional parameter.....	64
Figure 4.10 Percentage composition of each phase as a function of temperature.....	65
Figure 5.1 PXRD pattern of $\text{LaSmZr}_2\text{O}_7$ after calcining at $900 \text{ }^\circ\text{C}$ .....	70
Figure 5.2 Structure of $\text{LaSmZr}_2\text{O}_7$ viewed along the a-axis. Sm (pink), La (white), Zr (green) and O (red).....	71
Figure 5.3 PXRD pattern of $\text{LaSmZr}_2\text{O}_7$ after annealing at $1200 \text{ }^\circ\text{C}$ .....	72
Figure 5.4 Rietveld refinement profile of $\text{LaSmZr}_2\text{O}_7$ annealed at $1200 \text{ }^\circ\text{C}$ , $R_{\text{wp}} = 8.156\%$ .....	73
Figure 5.5 PXRD pattern of $\text{LaYZr}_2\text{O}_7$ calcined at $900 \text{ }^\circ\text{C}$ .....	74
Figure 5.6 Structural model of $\text{LaYZr}_2\text{O}_7$ as viewed from the (100) face. La (white), Y (blue), Zr (green) and O (red).....	75
Figure 5.7 PXRD pattern of $\text{LaYZr}_2\text{O}_7$ after annealing at $1200 \text{ }^\circ\text{C}$ .....	77
Figure 5.8 Rietveld refinement profile of $\text{LaYZr}_2\text{O}_7$ annealed at $1200 \text{ }^\circ\text{C}$ , $R_{\text{wp}} = 10.99 \%$ .....	77
Figure 5.9 PXRD pattern of $\text{SmYZr}_2\text{O}_7$ calcined at $900 \text{ }^\circ\text{C}$ .....	78

Figure 5.10 Structural model of SmYZr <sub>2</sub> O <sub>7</sub> showing the unit cell and bonding of the atoms. Oxygen (red) and Sm, Y and Zr (green randomly filled sphere).....	79
Figure 5.11 PXRD pattern of single phase SmYZr <sub>2</sub> O <sub>7</sub> after annealing at 1200 °C.....	80
Figure 5.12 Rietveld refinement profile of SmYZr <sub>2</sub> O <sub>7</sub> annealed at 1200 °C, Rwp = 8.016% and a = 5.234 Å.....	81
Figure 5.13 Variable temperatures PXRD pattern of SmYZr <sub>2</sub> O <sub>7</sub> from 303 K to 1053 K.....	82
Figure 5.14 Variable temperature PXRD pattern showing (311) and (222) peaks.....	83
Figure 5.15 Lattice parameter obtained from Rietveld refinement as a function of temperature plot for SmYZr <sub>2</sub> O <sub>7</sub> .....	83
Figure 5.16 Elemental maps for a chosen crystal of LaSmZr <sub>2</sub> O <sub>7</sub> structure.....	85
Figure 5.17 Elemental maps for a chosen crystal of LaYZr <sub>2</sub> O <sub>7</sub> structure.....	86
Figure 5.18 Elemental maps for a chosen crystal of SmYZr <sub>2</sub> O <sub>7</sub> structure.....	87

### List of Tables

Table 1.1: Positional parameters of A <sub>2</sub> B <sub>2</sub> O <sub>6</sub> O' pyrochlore type structure.....	2
Table 3.1 Structural model of La <sub>2</sub> Zr <sub>2</sub> O <sub>6</sub> O'.....	36
Table 3.2 Structural model of Sm <sub>2</sub> Zr <sub>2</sub> O <sub>7</sub> .....	39
Table 3.3 Structural model of Y <sub>2</sub> Zr <sub>2</sub> O <sub>7</sub> .....	42
Table 5.1 Structural model of LaSmZr <sub>2</sub> O <sub>7</sub> pyrochlore type.....	71
Table 5.2 Structural model for LaYZr <sub>2</sub> O <sub>7</sub> as a pyrochlore structure type.....	75
Table 5.3 Structural model of SmYZr <sub>2</sub> O <sub>7</sub> as a defect fluorite.....	79

# Chapter 1

## Introduction

The need for cleaner energy generation has gained momentum due to environmental concerns. Coal and oil reserves are decreasing and this means renewable energy is the path that the world will follow in meeting the global energy demand. This is an indication that the materials world is of utmost importance because these materials are used in cleaner technologies. As a result many countries have embarked on this journey of finding materials that will improve performances of new energy systems such as batteries, solar cells and fuel cells to name a few. Functional materials therefore are major ones in these growing technologies because of their chemical and physical properties. These materials possess different classes of properties that make them a viable option in the aforementioned technological applications. Pyrochlore structured materials make up part of these functional materials and they have now been extensively studied because of their properties. These materials will therefore be studied throughout this dissertation.

### 1.1 Pyrochlore structure

Pyrochlore  $(\text{Na,Ca})_2\text{Nb}_2\text{O}_6(\text{OH,F})$  is a mineral that occurs naturally and was first described in 1826 in Norway <sup>1</sup>. Mixed metal oxides with the general formula,  $\text{A}_2\text{B}_2\text{O}_7$  (in this case A and B are metals), are potentially isostructural to the pyrochlore mineral <sup>2-3</sup>. The A metal is normally a trivalent rare earth cation but in other rarer examples it can be a monovalent or divalent cation. The B metal can be a 3d, 4d or 5d transition metal with an oxidation state which gives a neutral molecule for the  $\text{A}_2\text{B}_2\text{O}_7$  compositional formula <sup>4</sup>. The two most common forms are (3+, 4+) and (2+, 5+) and have the following representative formulae  $\text{A}^{3+}\text{B}^{4+}\text{O}_7$  (e.g  $\text{Y}_2\text{Zr}_2\text{O}_7$ ,  $\text{La}_2\text{Sn}_2\text{O}_7$ ) and  $\text{A}^{2+}\text{B}^{5+}\text{O}_7$  (e.g  $\text{Mn}_2\text{Sb}_2\text{O}_7$ ,  $\text{Sn}_2\text{Nb}_2\text{O}_7$ ) <sup>5-7</sup>. Pyrochlore structures of the form  $\text{A}_2^{(3+)}\text{B}_2^{(4+)}\text{O}_7$  are the most common forms mainly due to a large occurrence of  $\text{A}^{3+}$  and  $\text{B}^{4+}$  cations that have a required ionic radii size for forming stable pyrochlore structures. Doping of parent compounds can occur as long as the averaged ionic size and charge does not exceed the stability regions for the phase existence.

An ideal pyrochlore adopts  $Fd-3m$  as its space group and has eight formula units per unit cell ( $Z=8$ ) <sup>8,9</sup>. The generalised structural formula of a pyrochlore structured material can be

written as  $A_2B_2O_6O'$ . The Wyckoff positions, site symmetry and fractional coordinates are listed in Table 1.1 with the B site set as the origin.

Table 1.1: Positional parameters of  $A_2B_2O_6O'$  pyrochlore type structure.

Site	Site symmetry	Wyckoff position	Fractional coordinates
A	-3m	16d	0.5, 0.5, 0.5
B	-3m	16c	0, 0, 0
O	Mm	48f	x, 0.125, 0.125
O'	-43m	8b	0.375, 0.375, 0.375

The A ion has a larger cationic radius of about  $1\text{\AA}$  or larger and sits at the 16d position. This is coordinated by 8 oxygen (O) atoms (six from the 48f site and two from the 8b site), this makes the A ion located within a scalenohedron. This scalenohedron is formed in an environment that has a coordination number of eight where the oxygen's form distorted cubes and this is referred to as a scalenohedra with twelve faces and each face representing a scalene triangle. The B ion has a smaller cationic radius which is  $\sim 0.6\text{\AA}$ , which sits at the 16c position and is coordinated by 6 oxygen atoms (six from the 48f site) to the B ion located within a trigonal antiprism. The oxygen atoms at the 8b position are tetrahedrally coordinated by the A cations whilst those at the 48f position are coordinated by two A cations and two B cations respectively<sup>4, 10</sup>. An eighth of a unit cell of a pyrochlore is shown in Figure 1.1 with Wyckoff positions for the A, B cations and the oxygen atoms. Site 8a is vacant, which serves as the origin for some of the physical properties exhibited by pyrochlore structured materials. This will be discussed further in the coming sections. The unit cell parameter of a cubic pyrochlore is typically around  $10\text{\AA}$ , being double that of a cubic fluorite structured material. Comparisons are normally made between the two structures as pyrochlores can be thought of as supercells of cubic fluorites<sup>11</sup>.

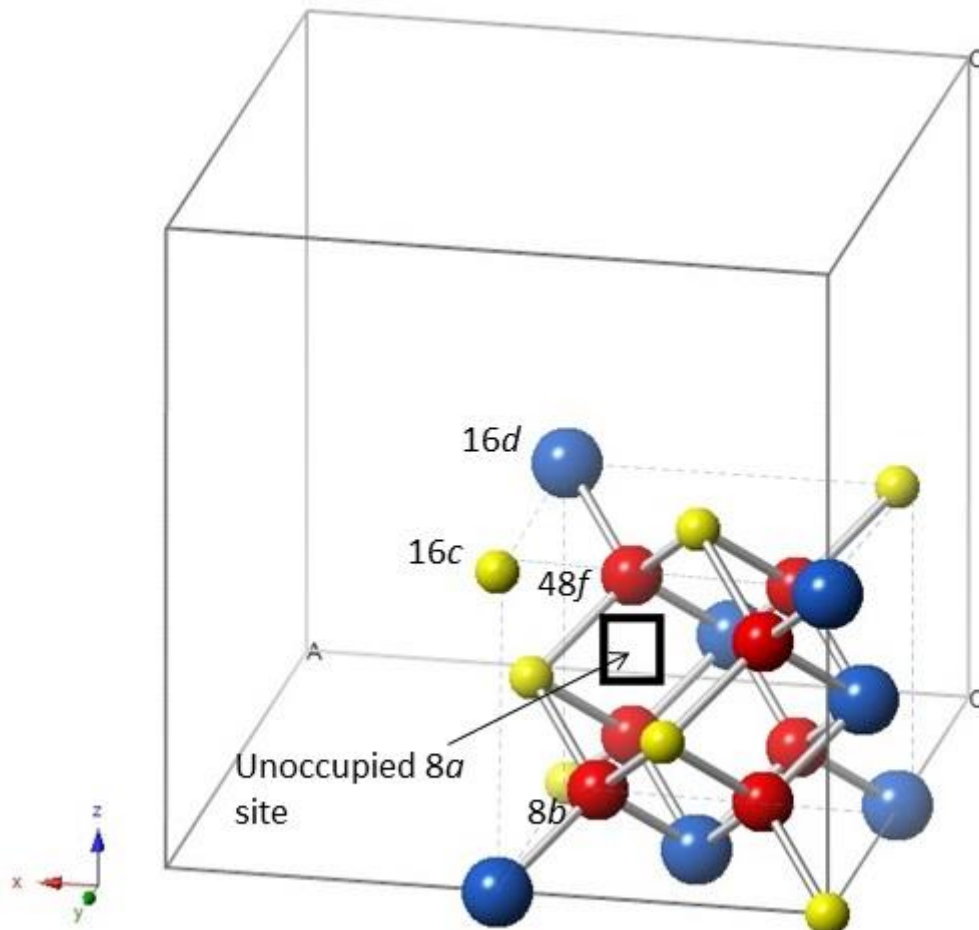


Figure 1.1: Cubic 1/8 unit cell of a pyrochlore with the Wyckoff positions of the atoms.

The unit cell of a classic fluorite structure is shown in Figure 1.2. The major difference between Figure 1.1 and 1.2 is that Figure 1.1 (pyrochlore) has four distinct crystallographic positions while Figure 1.2 (fluorite) has only two distinct positions namely 4a and 8c. The 4a site contains the cations whereas the 8c site contains the anions.

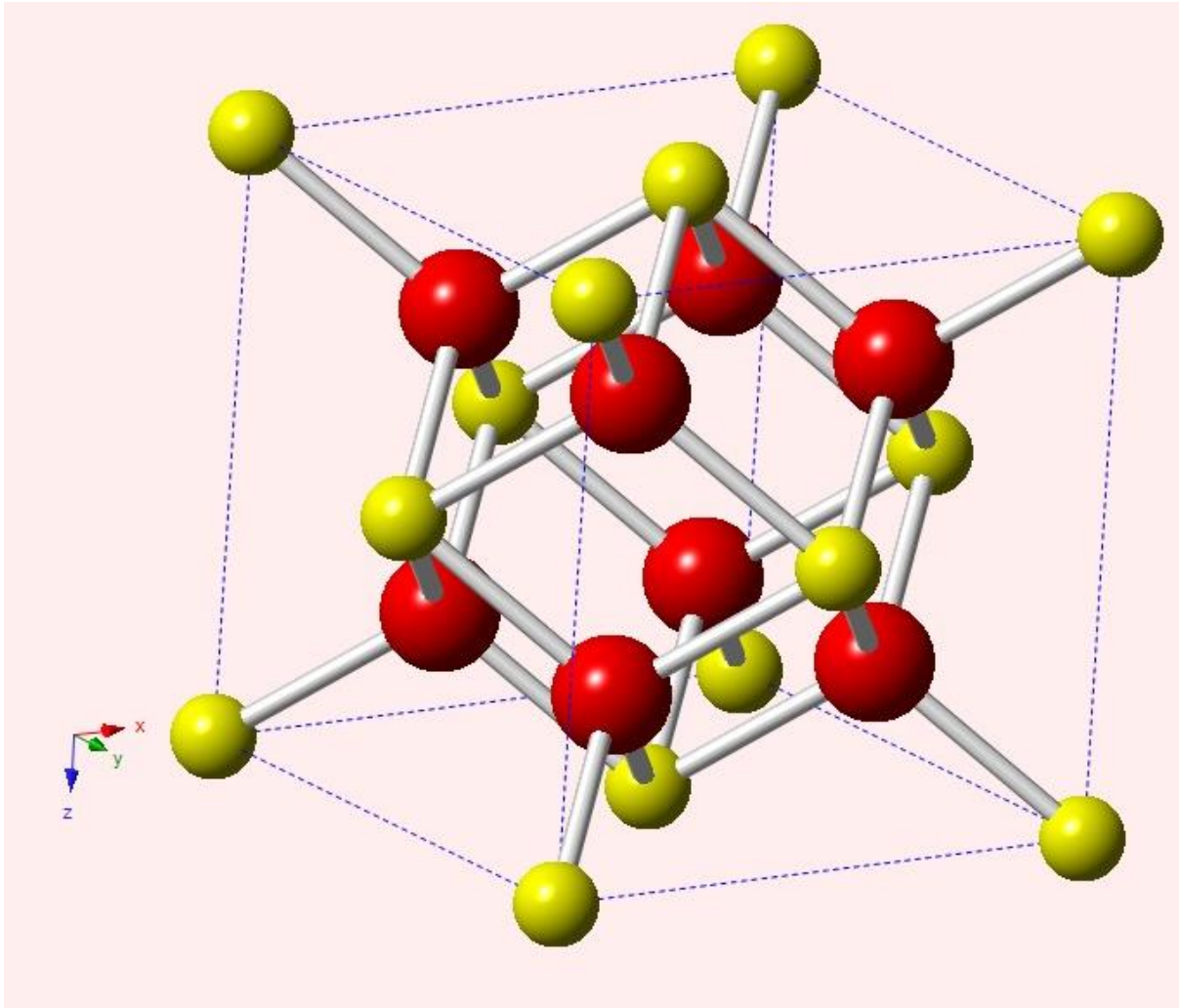


Figure 1.2: fluorite unit cell where the red spheres are anions and the yellow spheres represent a cation.

Cubic pyrochlore structures can be thought of as fluorite structures with twice the lattice parameter. The reason the lattice parameter of pyrochlore structures is twice that of cubic fluorites is mainly due to an ordering of the vacant oxygen position<sup>4</sup>. Figure 1.3 shows a complete unit cell of a pyrochlore viewed along the a-axis.

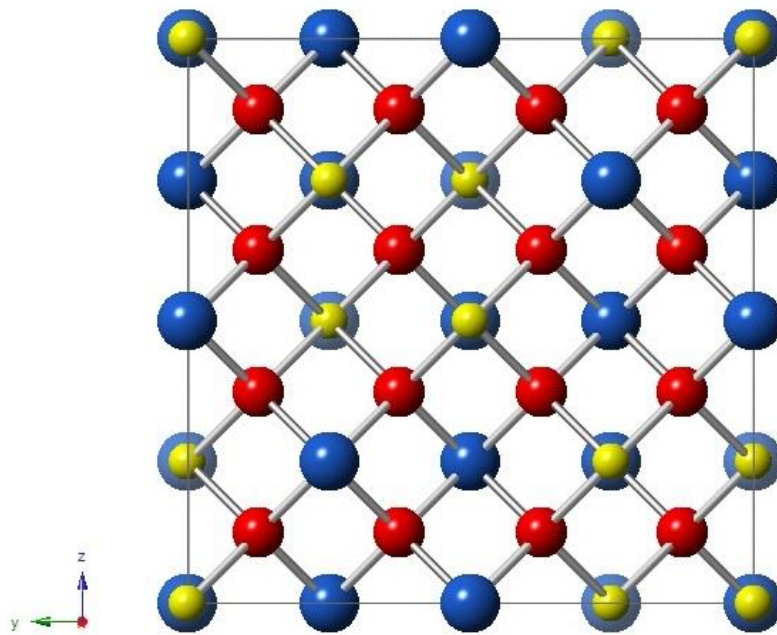


Figure 1.3: The cubic unit cell of an ordered pyrochlore viewed along the a-axis, oxygen positional parameter  $x=0.375$ . The blue spheres represent the A cation, yellow represents the smaller B cation while the red spheres represent the oxygen anions.

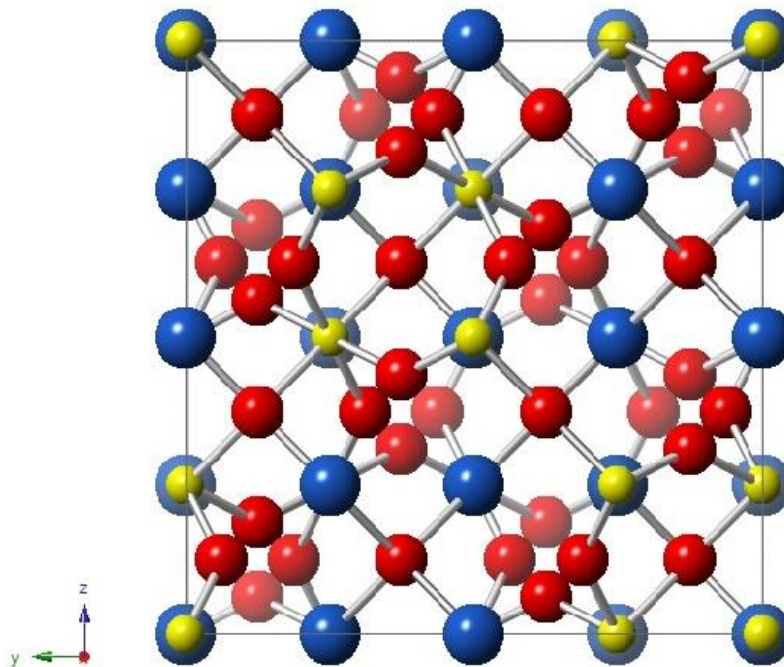


Figure 1.4: Disordered pyrochlore structure viewed along the a-axis, oxygen positional parameter  $x=0.3125$ .

The cubic fluorite structure is higher in symmetry in comparison to pyrochlore and this implies that the description of a pyrochlore structure based on a cubic fluorite structure arises due to polyhedra made by the A and B cations, these change shape based on the oxygen positional parameter ( $x$ )<sup>4</sup>. This parameter is the only value that can be refined and minute variations have notable effects on the overall pyrochlore structure. The lower limit of the positional parameter  $x=0.3125$  while the upper limit  $x=0.375$ . Figure 1.3 shows a pyrochlore with the oxygen positional parameter  $x=0.375$  which represents of a classic pyrochlore. When the positional parameter is changed slightly the overall structure of the pyrochlore is affected as seen in Figure 1.4, from this Figure it is evident that the structure moves from order to disorder. It is noteworthy however that the disorder arises from oxide anions at the 48f site while the other ions retain their positions; this thus has led to the oxygen positional parameter being associated with the oxygen ions at the 48f site. This value affects coordination and bonding of the polyhedron created by the cations and the oxide anions, as a result the structural description of pyrochlore structures varies with different positional parameters<sup>12-14</sup>. The  $BO_6$  polyhedron of pyrochlores at the upper limit and lower limit are shown in Figure 1.5.

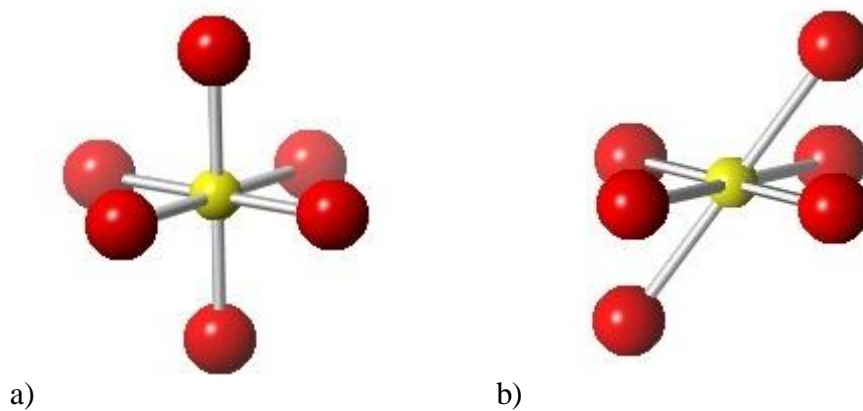


Figure 1.5: Visual aids showing the  $BO_6$  polyhedron and their differences for varying 48f  $x$  positional parameters Yellow spheres represent the B cation while the red ones represent oxide anions. Part a) shows the  $BO_6$  polyhedron for  $x=0.375$  while b) shows the polyhedron for  $x=0.3125$

Figure 1.5 shows structural differences in the octahedron created by the B cation and the oxide anions. Part a) of the illustration shows that the octahedron is perfect in the sense that

all the bond angles between the B cation and the oxide ions is  $90^\circ$  while part b) of Figure 1.5 shows a distortion of the axial oxide ions. This distortion is mainly due to the  $48f$  x positional parameter, as it decreases from 0.375 to 0.3125 the oxide anions tend to shift from their initial ordered position to disordered positions leading to distortions thus varying angles with the bond distances however remaining the same at  $2.339\text{\AA}$ . Two varying angles are created in part b) and these are  $70.53^\circ$  and  $109.47^\circ$ . These differences are the ones that lead to the differing descriptions of the pyrochlore structure <sup>4</sup>.

Distinct structural descriptions have been mentioned in literature over the years and these are:

- Structure based on the fluorite unit cell with a deficient anion <sup>15</sup>
- Corner linked  $\text{BO}_6$  polyhedron where A cations are accommodated in the interstices <sup>16</sup>
- $\text{BO}_6$  polyhedron and  $\text{A}_2\text{O}$  chains as interpenetrating networks <sup>17</sup>

Although there is no single description that best describes pyrochlore structures the most common is that based on a fluorite unit cell with a deficient anion, this description is however suitable when the  $48f$  x oxygen positional parameter is 0.375. At positional parameter 0.375 oxide anions are in an ordered form, thus satisfying requirements for the structure to be based on a fluorite unit cell. The pyrochlore unit cell as detailed here is described as an ordered  $7/8$  vacancy of the anions. The face centred cations are ordered in an ABAB order at different mirror planes, this order results in the generation of three kinds of interstices where the anions are occupied. The three interstices are; (1) 8a site which is vacant pyrochlores, (2) the 8b site which is coordinated by four A cations and (3) 48f site that is coordinated by two A cations and two B cations. The sites mentioned lead to different site symmetries within the unit cell of a pyrochlore, thus causing pyrochlores to have a different space group. This description is simple and is of a high interest for compound with a B cation that has a larger ionic radius;  $\text{Zr}^{4+}$  is one of those cations. Compounds that have  $\text{Zr}^{4+}$  as the B cation have transitions that occur normally at higher temperatures, these are order to disorder transitions. In this context the transitions are pyrochlore to defect fluorite structures <sup>4</sup>.

## 1.2 Defect fluorites

Defect fluorite structures are subcells of pyrochlore structured materials with some occurring naturally while others have to be induced from pyrochlores by high temperature order to disorder transitions. This order to disorder transformation is not only induced by temperature but there are a variety of stimulators that can induce this and these are; ion-irradiation, pressure and compositional changes<sup>18-20</sup>. Defect fluorites have a similar structure to natural fluorites (CaF<sub>2</sub> specifically). The space group of defect fluorites is Fm-3m and the unit cell length (a) is approximately 5Å and there are two Wyckoff positions, (1) 4a which occupies both the A and B cation and (2) 8c which occupies the O<sup>2-</sup> anions<sup>21</sup>. The oxygen atoms in this system are tetrahedrally coordinated by random cations and are evenly distributed, making the oxygen sites equivalent.

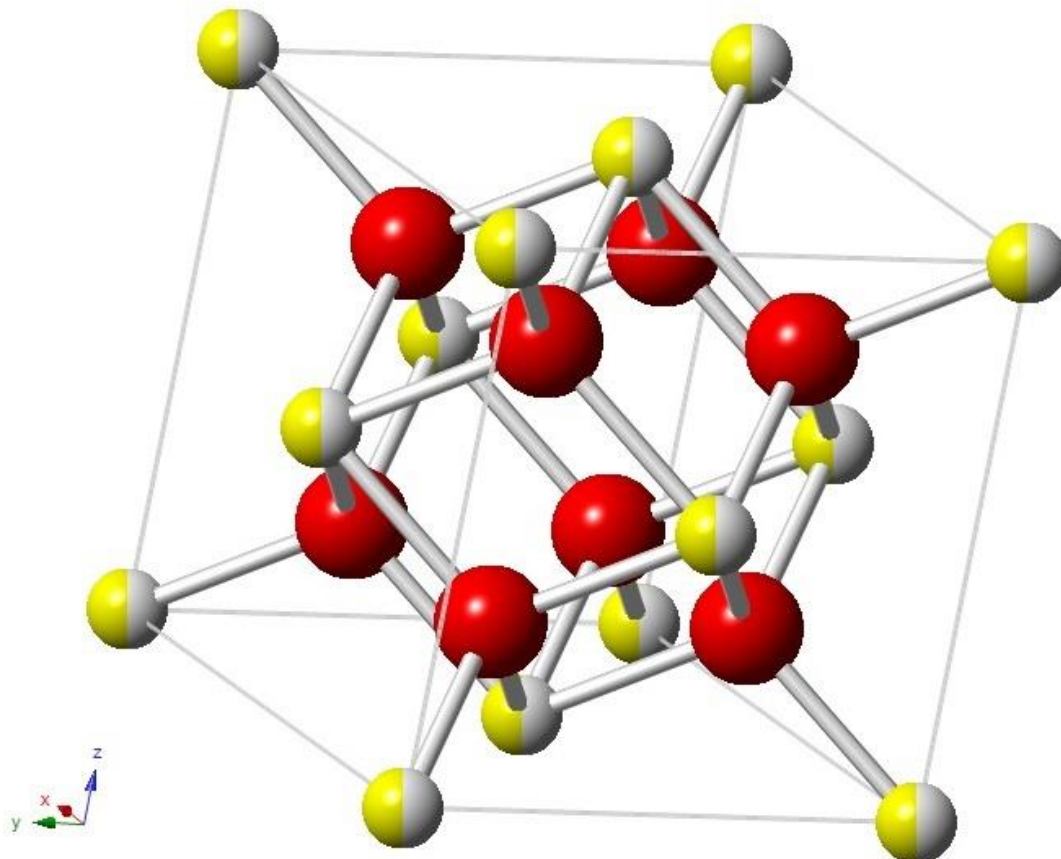


Figure 1.6: Unit cell of a defect fluorite. The red spheres represent the O<sup>2-</sup> anions occupying the 8c site and the yellow and white spheres represent the A and B cations which occupy the same position.

Figure 1.6 shows that the A and B cations share the same Wyckoff position in defect fluorites and have approximately 50/50 site occupancy. The disordering of the cations leads to the unit cell length of defect fluorites averaging a value of  $5\text{\AA}$  because the cations share a position and as a result the unit cell is half that of an ideal pyrochlore. The site occupancy of the oxide anions in this case becomes 0.875 and this satisfies the  $7/8$  oxide occupancy that is also observed in ordered pyrochlores. The general formula of defect fluorites is  $(A^{3+}, B^{4+})O_2$  which is similar to  $\text{CaF}_2$  which indicates that instead of one cation existing there are two cations. The coordination number of the A/B cations is 8 in defect fluorites this is formed the oxide ions which are nearby neighbours.

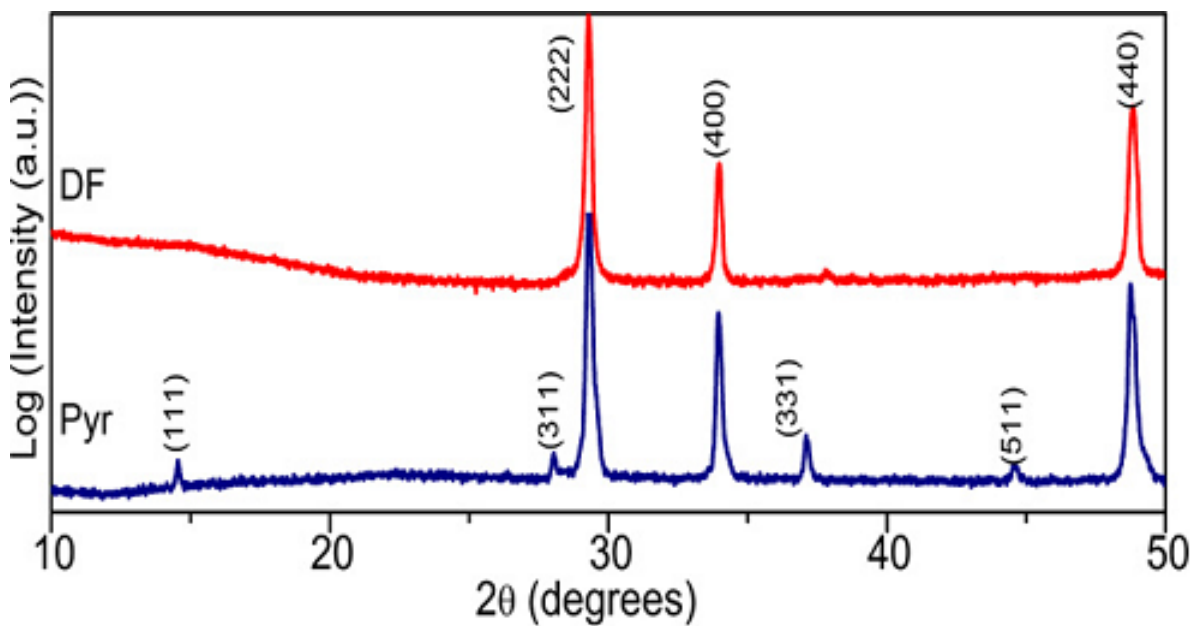


Figure 1.7: Powder X-Ray diffraction patterns of a pyrochlore (Pyr) and a defect fluorite (DF) obtained using  $\text{CuK}\alpha$  radiation<sup>21</sup>.

Figure 1.7 shows the diffraction patterns of a pyrochlore as compared to that of a defect fluorite. From Figure 1.7 it is evident that pyrochlores are different from defect fluorite structures. Pyrochlore structures have superlattice peaks which results from the larger unit cell and the different site symmetries that exist within the unit cell, these superlattice reflections are from the planes (111), (311), (331) and (511) respectively and they are not present in defect fluorites<sup>21</sup>. It can be said that the pyrochlore and defect fluorite structures are related with respect to temperature as the order to disorder transition is what leads to the superlattice reflections diminishing as the temperature increases.

Pyrochlore materials that undergo phase transitions, like zirconium ( $\text{Zr}^{4+}$ ) containing structures will have the pyrochlore structure at lower temperatures, meaning they will have

the superlattice reflections mentioned above and as the temperature rises to values above 1500 °C the superlattice peaks diminish, thus implying that they go from pyrochlore to defect fluorite structures. For some given radius ratios of the cations (A and B) there are temperatures at which the defect fluorite phase will be more stable than the pyrochlore phase and more preferable <sup>22</sup>. In a study conducted by Maran *et al* it was shown that for zirconium based pyrochlores (represented by  $\text{Eu}_2\text{Zr}_2\text{O}_7$ ) as the heat increases they transform from pyrochlore to defect fluorite and because the transformation is reversible they return to the pyrochlore phases with cooling. There are some studies that have been done to determine the transition temperature for a few chosen zirconate based pyrochlores and these data are as follows; for  $\text{Gd}_2\text{Zr}_2\text{O}_7$  it is 1530 °C, while that of  $\text{Sm}_2\text{Zr}_2\text{O}_7$  is 2200 °C and for  $\text{Nd}_2\text{Zr}_2\text{O}_7$  the transition temperature is 2300 °C. From this trend it is evident that the transition temperature of lanthanide containing zirconates increases with increasing ionic radii and decreases when the  $r_A/r_B$  ratio approaches the lower limit in the stability field of pyrochlores <sup>23-25</sup>.

### 1.3 Properties and applications

As mentioned the majority of pyrochlore structured materials that exist are of the  $(3^+, 4^+)$  type. Phase stability in ordered pyrochlores is determined by the cation ratio of A and B <sup>2</sup>. Metals with similar cationic ratios tend to form defect fluorites. This means that a structure having  $r_A/r_B$  closer to one ( $r_A/r_B < 1.46$ ) adopts a defect fluorite type structure, whereas structures with a greater  $r_A/r_B$  (between 1.46 and 1.78) crystallize as ordered pyrochlores. The pyrochlore stability range as calculated by Mervini *et al* <sup>26</sup> on the basis of the A:B radius ratio is 1.46 (represented by  $\text{Gd}_2\text{Zr}_2\text{O}_7$ ) to 1.78 (represented by  $\text{Sm}_2\text{Ti}_2\text{O}_7$ ) <sup>27</sup>. An increase or decrease of the ratio  $r_A/r_B$  mirrors the behaviour of the 48f x oxygen positional parameter, this parameter as mentioned before accounts for the amount the oxygen anion at position 48f moves from its coordinated tetrahedron to the vacant 8a position <sup>28</sup>. Classic pyrochlore structures are thought to have a positional parameter  $x=0.375$  as their upper limit <sup>12-14</sup>. The stability of pyrochlore structures have been found to increase as the radius ratio ( $r_A/r_B$ ) decreases from its upper limit <sup>5</sup>.

Figure 1.8 represents the stability map of pyrochlores and defect fluorites which is based on the A and B cationic ratios in these mixed metal oxides <sup>29</sup>. From the map it is relatively easy to predict if certain systems would be pyrochlores, defect fluorites or other structures.

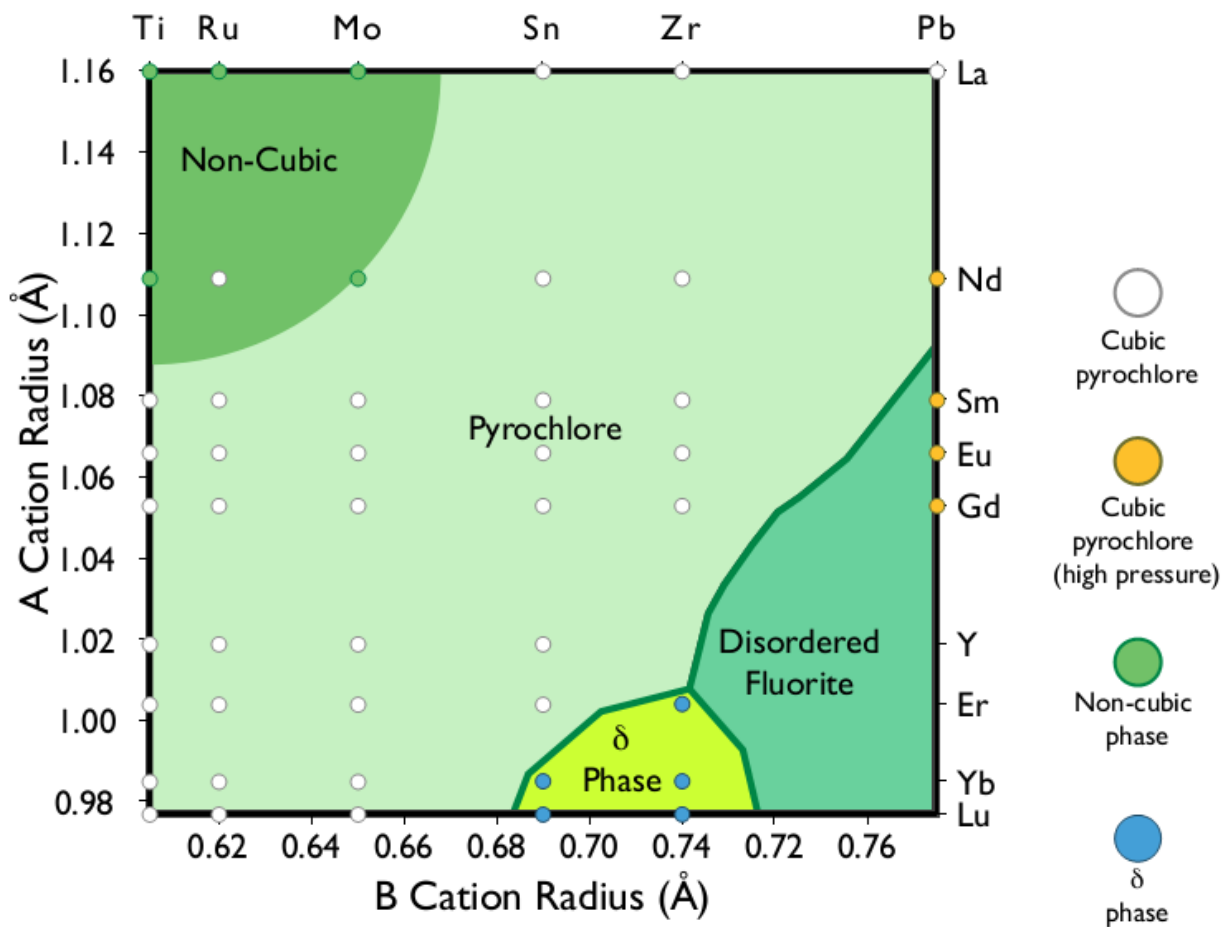


Figure 1.8: Stability map of pyrochlores and defect fluorites as predicted by Minervini *et al* 27, 29.

Pyrochlores have a wide range of applications that arise from the different physical properties they possess. Applications of pyrochlores include catalytic behaviour, magnetic, electrical, dielectric and radioactive waste disposal<sup>3, 13, 31-33</sup>. The different properties arise from the different cations used in the formation of pyrochlores (which determines the ionic size), electronic configuration and the polarizability of the ions. Pyrochlores with an electronic behaviour may have insulating, semiconducting or metallic properties. These properties allow this group of pyrochlores to have applications as high permittivity ceramics, thermistors and switching elements which have sudden changes in electrical conductivity at certain temperatures<sup>3</sup>. Some pyrochlores have applications in photocatalysis, during this process the semiconductor-type pyrochlores use solar energy to break down organic pollutants and split water to release chemical energy<sup>34-36</sup>. A study conducted by Gaur *et. al* showed that

lanthanum calcium rhodium zirconium (LCRZ) catalyst was effective for dry reforming of methane ( $\text{CH}_4$ )<sup>37</sup>. Rare-earth zirconate pyrochlores find applications as thermal barrier coatings, this feature allows them to insulate and protect hot-section metal components in turbines which are used for power generation and air compression in aircrafts<sup>38</sup>. Pyrochlores can also be used for the immobilization of radioactive waste, especially of the actinides. Zirconates and titanates are some of the best Pyrochlores used for the radioactive waste disposal due to their chemical durability and radiation resistance<sup>13</sup>. These materials are able to immobilise nuclear wastes because they can incorporate certain lanthanides, actinides and other elements that are generated as by products in nuclear reactors.

Pyrochlore materials also find application as electrolytes in solid oxide fuel cells (SOFCs) due to their ability to conduct oxygen ions<sup>39</sup>. SOFCs are fuel cells that use a mixed metal solid oxide (pyrochlore in this case) which conducts oxygen ions to convert chemical energy to electrical energy, this energy is used as an advanced power source<sup>40</sup>. SOFCs are cleaner and have lower rates of pollution and they generate electricity at higher efficiencies; other advantages include low levels on greenhouse gases, fuel adaptability and reliability<sup>41</sup>. The increasing interest in alternative energy sources is based on the global energy crisis and the need to use greener technologies in combating global warming. SOFCs fit this criterion and are thus by far the most efficient power generating technologies<sup>42</sup>. They use hydrogen, natural gas and some renewable fuels to generate electricity. SOFCs have a similar design as standard electrochemical cells; a cathode, anode and an electrolyte. The electrolyte of SOFCs however conducts oxygen ions. Figure 1.9 shows a concept diagram of a SOFC, this diagram shows  $\text{H}_2$  as the fuel and  $\text{O}_2$  is the oxidant<sup>43</sup>. The fuel enters the cell and is oxidized in the anode and releases electrons that pass through an external circuit, from the external circuit the electrons migrate to the cathode where they react with oxygen to produce oxide ions. Oxide ions create a gradient on the electrolyte and in the process they migrate to the anode. The reduced oxidant then combines with the oxidized fuel and this gives off water and heat as the by-products. The electrons released to the external circuit are then used to generate power.

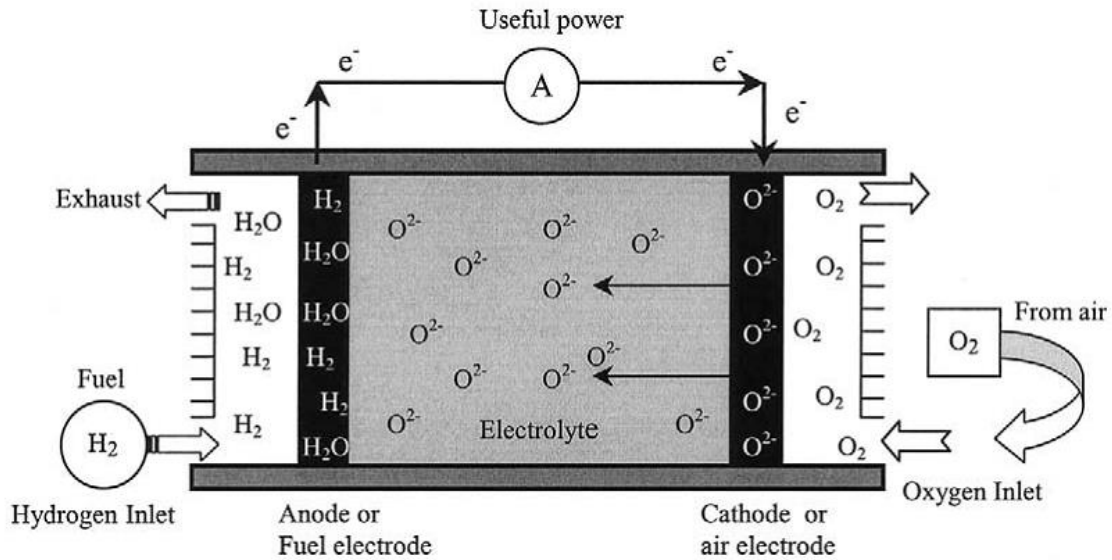


Figure 1.9: Diagram of a solid oxide fuel cell (SOFC) that conducts oxygen ions <sup>43</sup>.

There is a variety of pyrochlore and defect fluorite structured materials that exhibit oxygen-ion conductivity, the best known and widely used is yttria-stabilized zirconia (YSZ) which adopts a defect fluorite structure type. YSZ is used because it has high oxygen-ion conductivity. Adding yttria to the zirconia stabilizes the cubic fluorite phase that is conductive and generates vacancies in the lattice, this then contributes in the transportation of oxygen ions <sup>44</sup>. Pyrochlores that exhibit oxygen ion conductivity at high temperatures similar to YSZ were found in the zirconate family in the form  $\text{Ln}_2\text{Zr}_2\text{O}_7$  ( $\text{Ln}=\text{Nd}, \text{Sm-Gd}$ ) <sup>45</sup>. A disadvantage associated with YSZ and other oxygen-ion conducting Pyrochlores is that they operate at temperatures between 600-1000 °C, such temperatures limit the utility of these materials as they degrade, undergo thermal stress and require long start-up times <sup>42, 46-47</sup>. Therefore this increases the need for Pyrochlores that will conduct oxygen ions at lower temperatures.

### 1.4 Thermal Expansion in Pyrochlores

Thermomechanical properties are important in selecting materials for use in SOFC. These properties include thermal expansion coefficient (TEC), mechanical toughness, morphological and geometrical stability to name a few <sup>48</sup>.

Thermal expansion is defined as the propensity of matter to have a change in volume with response to a change in temperature (i.e upon heating); one other definition of this phenomenon is the net change in the separation between atoms of a material <sup>49</sup>. The implication of thermal expansion is higher thermal vibrations between the atoms at higher

temperatures. This physiochemical phenomenon affects the vast majority of materials seeing that their expansion may lead to changes in the structure, thus affecting its properties. The thermal expansion coefficient is sensitive to structural changes and this implies that it reflects any structural changes that occur in a material<sup>50</sup>.

The volumetric thermal expansion coefficient is determined by the following equation<sup>50</sup>:

$$\alpha_v = \frac{1}{V} \left( \frac{\partial V}{\partial T} \right)_P \quad (1.1)$$

where  $V$  represents the volume and  $T$  is the temperature at constant pressure. The linear thermal expansion coefficient is represented as:

$$\alpha_L = \frac{1}{L} \left( \frac{\partial L}{\partial T} \right)_P \quad (1.2)$$

where  $L$  represents the unit cell length in the measured direction. This is defined for cubic systems where the lengths of all the axes are equal.

Changes in thermal expansion of a material can be visualized in a powder X-ray diffraction (PXRD) pattern of a material. When expansion happens in a material the Bragg reflections shift to lower angles and this can be explained by Bragg's law which is as follows:

$$n\lambda = 2d \sin\theta \quad (1.3)$$

where  $n$  is an integer for the given order,  $\lambda$  represents the wavelength of the x-rays used,  $d$  is the interatomic spaces between the planes and  $\theta$  is the angle between the incident rays and the scattering planes<sup>51</sup>. As the interatomic space increases, the lattice parameter increases and this in turn decreases the Bragg angle.

Different materials possess different types of thermal expansion while other materials tend to contract instead of expanding. Some of the known and interesting types of thermal expansion are negative thermal expansion (NTE) and low thermal expansion (LTE), these will be discussed below

### **Negative thermal expansion**

Negative thermal expansion is described as the tendency of a material to contract upon thermal treatment. As it was discussed earlier looking at Bragg's law, with NTE the Bragg

reflections shift to higher angles implying that the interatomic spaces in a unit cell decrease. This affects the unit cell parameters, meaning that the unit cell lengths decrease and this is why it is called thermal contraction. NTE based on unit cell lengths and temperature is called intrinsic NTE and this is the one that was described above. This intrinsic NTE has two categories and these are anisotropic or isotropic. Anisotropic NTE is when one or two unit cell lengths decrease while the other one is unaffected, isotropic NTE affects all the unit cell lengths meaning that the entire unit cell contracts <sup>52</sup>.

### **Low thermal expansion**

Low thermal expansion (LTE) is when a material expands but the expansion is infinitesimal. A majority of mixed metal oxides tend to possess this type of thermal expansion and pyrochlore materials are one example, this is however isotropic in this material because pyrochlore materials have a cubic unit cell. These have been thoroughly investigated and their thermal expansion coefficients have been determined and shown in literature.

In a study conducted by Kutty *et al* various lanthanide containing zirconates ( $\text{Ln}_2\text{Zr}_2\text{O}_7$ ) were investigated and their thermal expansion coefficients were determined, these were found to be in the range of  $8\text{-}11 \times 10^{-6} \text{ K}^{-1}$  and this is considered low to intermediate thermal expansion. The trend they discovered was that as the ionic radius of  $\text{Ln}^{3+}$  decreases the thermal expansion coefficient increases, this implies that TEC increases from  $\text{La}_2\text{Zr}_2\text{O}_7$  up to  $\text{Gd}_2\text{Zr}_2\text{O}_7$  <sup>53</sup>.

In another study done by Guo *et al* it was discovered that doping rare earth zirconates with smaller amounts of  $\text{Sc}_2\text{O}_3$  increases TEC. This is attributed to the  $\text{Sc}^{3+}$  occupying interstitial sites within the crystal thus forming extra oxide ions. The formation of new oxide ions within the crystal reduces the crystal energy and increases the cohesive energy due the repulsion between the oxide anions thus increasing TEC <sup>54</sup>.

Wang *et al* did an interesting study on  $\text{Gd}_2\text{Zr}_2\text{O}_7$  doped with  $\text{Sc}_2\text{O}_3$  to investigate the effects of the dopant on the TEC this pyrochlore <sup>55</sup>. They, just like Guo *et al*, also discovered that the dopant enhances TEC and they explained this in mathematical terms using the following equation;

$$U = \frac{N_o A z^+ z^- e^2}{r_o} \left(1 - \frac{1}{n}\right) \quad (1.4)$$

and according to the equation  $U = \frac{N_0 z^2 e^2 A}{4\pi\epsilon_0 n r_0}$ ,  $U$ ,  $n$ ,  $r_0$ ,  $N_0$ ,  $z$ ,  $A$  and  $e$  are; the crystal energy, Born exponent, interionic distance, Avogadro's constant, ionic charge, Madelung constant and finally electron charge. The conclusion they came up with is that knowing very well that thermal expansion in solid materials is associated with the crystal energy, therefore doping leads to lattice expansion which reduces the degree of order within the crystal. This lattice expansion increases the interionic distance and the cationic together with the anionic disorder within the crystal decreases the Madelung constant, thus decreasing the crystal energy leading to an increased TEC. TEC is an important property in pyrochlores because of their many uses that either require minimal expansion or slightly higher expansions. This property can be influenced by the routes of synthesis.

## 1.5 Synthesis of pyrochlores

A variety of synthetic routes have been used over the years to synthesize pyrochlore materials. Mixed metal oxides, i.e pyrochlores to be specific, have physical and chemical properties that can be influenced by the synthetic route used because this determines the crystal homogeneity and microstructure, so the preparation route is of great importance and control during the synthesis is vital<sup>25</sup>. The different synthetic procedures that exist up to date have been modified such that they satisfy the properties required from a certain material, as far as the initial stages of the synthesis are concerned, the final stages also contribute to the final chemical and physical properties especially the sintering temperatures.

The routes of synthesis are dependent on the phases of the starting materials. Some starting materials could be in the solid phase and as a result the route of synthesis will be solid state synthesis, this is attributed to the fact that most of the powders and metal salts are insoluble in the solvents mostly used. A common solid state reaction used for the fabrication of pyrochlore materials is mechanochemical synthesis which uses a planetary ball mill; this will be further explored in chapter two. Solid state reactions usually require longer periods of mixing, heating and regrinding the reactants at high temperatures for better homogeneity of the final product. These types of reactions in essence are dependent upon atomic diffusion which is possible at very high temperatures for mixed metal oxides<sup>56</sup>. Although this method gives rise to highly crystalline products the disadvantage is that there is minimum or no control of the morphology and crystallite size, and because it's a thermodynamically induced process, it favours the formation of phases that are thermodynamically stable. Over time, various methods have been used to overcome problems associated with solid state reactions

and these techniques form part of solution or soft chemistry, however these methods still require annealing of the final product at high temperatures for better crystallinity. These techniques include the following; sol-gel synthesis, polymer pyrolysis and the citrate route. These are commonly used because of the added advantages they have as opposed to solid state reactions which are listed below<sup>56-57</sup>;

- Better homogeneous mixing of the reactants which leads to homogenous products
- Metastable phases that are not formed at high temperatures can be stabilized
- Higher control of the morphology, i. e the crystallite size and the shape
- Control of the desired reaction conditions

The sol-gel route, which was used for the preparation of the pyrochlore materials in this dissertation, will be further discussed.

## **1.6 Aim and objectives**

Pyrochlore materials show interesting physical properties and this has led to a range of studies on these materials, one of which is studying the thermoresponsive behaviour to investigate phase transformations and the thermal expansion coefficient. The properties that the materials exhibit has led to a range of applications that apply to the real world, these include electrolytes in fuel oxide fuel cells, immobilizing agents of actinides, thermal barrier coaters and photocatalysts among others. The aim of this study was to prepare zirconate based pyrochlore type materials, both pure and A site doped analogues, using the sol-gel method and the mechanochemical synthesis route. These were characterized using powder X-ray diffraction coupled with Rietveld analysis, variable temperature PXRD and electron probe microanalyzer (EPMA). The objectives of this study was to synthesize the following materials;  $\text{La}_2\text{Zr}_2\text{O}_7$ ,  $\text{Sm}_2\text{Zr}_2\text{O}_7$ ,  $\text{Y}_2\text{Zr}_2\text{O}_7$ ,  $\text{LaSmZr}_2\text{O}_7$ ,  $\text{LaYZr}_2\text{O}_7$ , and  $\text{SmYZr}_2\text{O}_7$  using sol-gel synthesis. This was coupled with synthesizing  $\text{La}_2\text{Zr}_2\text{O}_7$  using wet mechanochemical synthesis.

## 1.7 References

1. Wohler F., *Ann. Phys. Chem. Pogg.*, 1826, 7, 417-428.
2. Mandal B. P. and Tyagi A. K., *Barc. Newslett.*, 2010, 313, 6-13.
3. Mandal B. P. and Tyagi A. K., *J. Alloys Compd.*, 2007, 437, 260-263.
4. Subramanian M. A., Aravamuda G., and Subba Rao G. V., *Progress in solid state chemistry*, 1983, 15(2), 55-143.
5. Sickafus K. E., Minervini L., Grimes R. W., Valdez J. A., Ishimaru M., Li F., McClellan K. J., and Hartmann T., *Science*, 2000, 289, 784.
6. Shannon R. D. and Sleight A. W., *Inorg. Chem.*, 1968, 7, 1649
7. Bresse F., Stewart D. J., Seidl V., and Knop O., *Can. J. Chem.*, 1972, 50, 3648.
8. Wuensch B. J., *Solid State Ionics*, 2000, 129, 111-133.
9. Blanchard P. E. R., Clements R., Kennedy B. J., Ling C. D., and Reynolds E., *Inorg. Chem.*, 2012, 51, 13237-13244.
10. Wyckoff R. W. G., *Crystal Structures*, 1965, New York: Interscience Publishers, 2<sup>nd</sup> edition.
11. Cleave A. R., *Atomistic scale simulations for waste form applications*, Thesis, Imperial College of Science.
12. Chakoumakos, B., *J. Solid State Chem.*, 1984, 53, 120.
13. Lau G.C., McQueen T.M., Huang Q., Zandbergen H.W., and Cava R.J., *J. Solid State Chem.*, 2008, 181, 45.
14. Knop O., Brisse F., Meads R.E., and Bainbridge J., *Can. J. Chem.*, 1968, 46, 3829.
15. Aleshin E. and Roy R., *J. Am. Ceram. Soc.*, 1962, 45, 18.
16. Bystrom A., *Ark. Kem. Min. Geol.*, 1945, 18A.
17. Knop O., Brisse F., Castelliz L., and Sutarno, *Can. J. Chem.*, 1965, 43, 2812.
18. Hess N. J., Begg B. D., Conradson S. D., McCready D. E., Gassman P. L. and Weber W.J., *J. Phys. Chem. B*, 2002, 106 (18), pp 4663–4677
19. Sanjay Kumar N. R., Chandra Shekar N. V. and Sahu P. C., *Solid State Commun.*, 147, 357–359.
20. Moon P. K. and Tuller H. L., *Solid State Ionics*, 1988, 28-30, 470–474.
21. Maram P. S., Ushakov S.V., Weber R. J. K., Benmore C.J and Navrotsky A., *J. Am. Ceram. Soc.*, 2014, 1–8.
22. Heremans C., Wuensch B. J., Stalick J. K. and Prince E., *J. Solid State Chem.*, 1995, 117, 1 108-121.
23. Meilicke S. and Halle S., *Materials Research Society symposia proceedings.*, 393, 1995 55-60.
24. Michel D., Perez y Jorba M. and Collongues R., *Materials Research Bulletin*, 9, 11, 1974, 1457-1468.
25. Radhakrishnan A. N., *Studies on structure, lattice thermal expansion and oxide ion conducting properties of some rare earth based zirconate pyrochlores*, thesis, University of Kerala.
26. Rushton M. J. D., *Simulations of glass and ceramic systems for nuclear waste applications*, Thesis, University of London, 2006.
27. Ewing R. C., Weber W. J., and Lian J., *Journal of Applied Physics*, 2004, 95, 5949.
28. Cai L., Arias A. L., Nino J. C., *Journal of Materials Chemistry*, 2011, 21, 11, 3611.
29. Minervini L, and Grimes R. W., *Journal of the American Ceramic Society*, 2000, 83, 1873.
30. Zhang Y. Q., Xuan Y., Qian S. S., Li X. L., Jia Y. Q., *J. Mater. Sci.*, 1999, 34, 4475.
31. Gardner J. S., Ginras M. J. P., and Greedan J. E., *Rev. Mod. Phys.*, 2010, 82, 53.

32. Ali N., Hill M. P., Labroo S., and Greedan J. E., *J. Solid State Chem.*, 1989, 83, 178.
33. Cann D. P., Randall C. A., and ShROUT T. R., *Solid State Commun.*, 1996, 100, 529
34. Chen C., Ma W., and Zhao J., *Chem. Soc. Rev.*, 2010, 39, 4206–4219.
35. Ravelli D., Dondi D., Fagnoni M., and Albinì A., *Chem. Soc. Rev.*, 2009, 38, 1999–2011.
36. Sakata Y., Kamigouchi T., Tanaka S., Kamioka H., Matsumoto K., Fujimori H., *Catal. Sci. Technol.*, 2013, 3, 1691–1693.
37. Gaur S., Haynes D. J., and Spivey J. J., *Applied Catalysis A: General*, 2011, 403, 142–151.
38. Wu J., Wei X., Padture N. P., Klemens P. G., Gell M., Garcia E., Miranzo P., and Osendi M. I., *J. Am. Ceram. Soc.*, 2002, 85 (12), 3031-3035.
39. Shlyakhtina A. V., and Shcherbakova L. G., *Russian Journal of Electrochemistry*, 2012, 48, 1, 1-25.
40. De Jonghe L. C., Jacobson C. P., and Visco S. J., *Annu. Rev. Mater. Res.*, 2003, 33, 169-183.
41. Singhal S. C., *Prepr. Pap. –Am. Chem. Soc., Div. Fuel Chem.*, 2004, 49, 2, 478.
42. Wachsman E. D., and Taek Lee K., *Science*, 2011, 334, 935.
43. Stambouli A. B., and Traversa E., *Renewable and Sustainable Energy Reviews*, 2002, 6, 433-455.
44. Fergus J. W., *Journal of Power Sources*, 2006, 162, 30-40.
45. Van Dijk T., de Vries, K. J., and Burggraaf, A. J., *Phys. Status Solidi A*, 1980, 58, 115.
46. Bae J., Lee D., Hong S., Yang H., and, Kim YB., *Surface and Coatings Technology*, 2015, 279, 54-59.
47. Kido H., Komarneni S., and Roy R., *J. Am. Ceram. Soc.*, 1991, 74(2), 422-424.
48. Tietz F., *Solid State Ionics.*, 1999, 5, 129-138.
49. Tipler P. A., Mosca G. *Physics for scientists and engineers*, Sixth Edition, Volume 1, New York, NY: Worth Publishers, 666–670.
50. Krishnan R.S., Srinivasan R., Devanarayanan S. *Thermal expansion of crystals*, Oxford: Pergamon, 2-47.
51. Tipler P. A., Mosca G. *Physics for scientists and engineers*, Sixth Edition, Volume 1, New York, NY: Worth Publishers, 1091-1092.
52. Nyoni M. S., *Thermoresponsive Behaviour of Selected Mixed Metal Oxides*, dissertation, University of Witwatersrand, 2013.
53. Kutty K. V. G., Rajagopalan S., Mathews C. K. and Varadaraju U. V., *Materials Research Bulletin*, 1994, 29, 7, 759-766.
54. Guo L., Zhang Y., Wang C., Zhao X. and Ye F., *Materials & Design*, 2015, 82, 114–118.
55. Wang J., Nakamura A. and Takeda M., *Solid State Ionics*, 2003, 164, 3-4, 185-191.
56. Smart L. E., Moore E. A., *Solid State Chemistry*, Taylor & Francis Group, 2005.
57. Brinker C. J., Scherer G. W., *Sol-gel Science*, Academic Press, Inc., 1990.

## Chapter 2

### Experimental approach

#### 2.1 Synthesis

##### 2.1.1 Sol-gel synthesis

Homogeneity is a very important factor when synthesizing mixed metal oxides; this influences the overall morphology of the final product and leads to an evenly represented long range order of the material, which further determines the properties of the product. The sol-gel synthesis is a route that has been adopted for the synthesis of these mixed metal oxides as rapid solution diffusion leads to homogenous final products<sup>1</sup>. The greatest advantage with this route is that the homogeneous materials are achieved at low temperatures. Sol-gel synthesis can be defined as polymerization reactions that lead to oxide network formation from liquid reactants<sup>2</sup>. The word is divided into two parts; (1) sol which represents a solute or colloidal particles in a solvent, which in essence means a liquid with particles, (2) gel part which is a continuous polymer network. Sol-gel synthesis essentially produces a solid product from a dissolved compound in a liquid. Figure 2.1 shows a schematic diagram of a typical sol-gel synthesis route. Before the sol-gel forms stoichiometric amounts of the reactants are mixed in a suitable solvent (isopropanol in this case). With some gentle mixing of the precursors in a beaker using a magnetic stirrer the sol begins to form. This is followed by solvent evaporation which is normally done at room temperature for 2 days. The supercritical extraction route although not popular, is also a viable option. After the solvent has evaporated a xerogel forms which, as seen in Figure 2.1, results from the gel dried by evaporation which shrinks and collapses the gel network. Aerogel is different when compared to a xerogel due to the final product being dried under supercritical conditions, the resultant product has a retained network structure and due to this large pores form within the gel network<sup>2</sup>. The resulting product is then heated in the oven at high temperatures, typically 900 °C. The final product is a powder which can then be characterized.

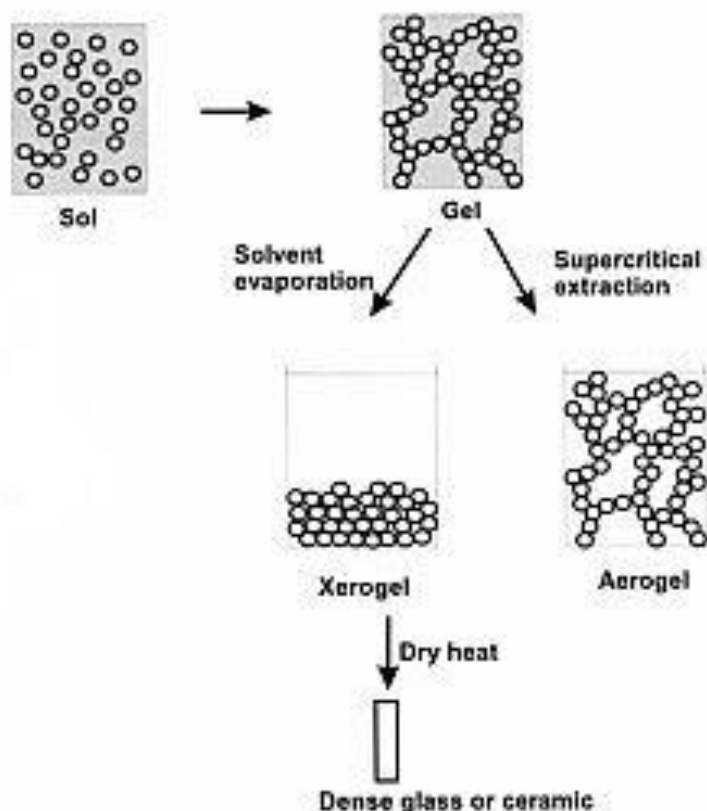


Figure 2.1 Schematic diagram showing how the sol-gel synthesis route works<sup>2</sup>.

### 2.1.2 Wet mechanochemical synthesis

Mechanochemical (MC) synthesis is a process that uses mechanical energy to produce transformations that may be chemical or physicochemical in a material<sup>3</sup>. This process uses a planetary ball mill which is shown in Figure 2.2. The milling pot is filled with balls that could either be zirconia based or stainless steel based; the powder reactants and a milling medium. In this procedure a liquid milling medium is used and this is why it is called wet mechanochemical synthesis. There is also dry mechanochemical synthesis but this is rarely used because of the disadvantage it possesses, powder tends to form agglomerations on the sides of the pot and it produces lower yields of the final product<sup>4</sup>. Figure 2.3 shows a schematic diagram of a zirconia pot and how everything is distributed inside the pot



Figure 2.2 Planetary ball mill used for mechanochemical synthesis.

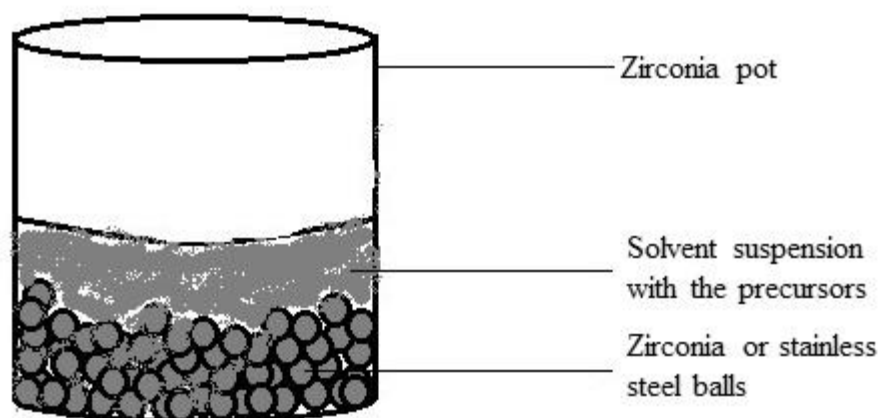


Figure 2.3: Diagram showing a zirconia pot and the constituents when stationary.

Wet mechanochemical synthesis has some added advantages as opposed to dry MC and these are listed below<sup>4</sup>:

- Decreased dust problems
- Increased homogeneity of the precursors
- Smaller particle size of the final product, which is desirable
- Higher rotational speeds for better mixing
- Lower power requirement
- Shorter times of synthesis and relatively a few variables need to be controlled

With wet MC stoichiometric amounts of the starting materials are weighed then added to a liquid milling medium for the formation of a suspension, then the balls are added. This is followed by the wet MC treatment in the planetary ball mill for 25 hours at the rotational speeds of 400 rotations per minute (rpm). The resultant product is then dried in an oven at 100°C until the product is dry; this takes up to 1 hour to produce a uniform powder. This powder is then ground using a pestle and mortar, then heated at temperature around 1200 °C for crystallization and followed by characterization.

## **2.2 Characterisation techniques**

Characterisation techniques describe the internal as well as external structure of the material. The information from these techniques also include the following; structural configuration, composition of the material and defects that exist in these materials. The defects that exist in a material play a key role in determining certain properties of a material that could be electrical, mechanical or thermal. Characterisation techniques that were used were classified into the following categories; diffraction methods, thermal analysis and microscopy methods. These methods will further be briefly discussed next.

### **2.2.1 Powder X-ray diffraction**

X-ray powder diffraction is fast, non-destructive technique that uses X-rays for the characterization of powder materials or crystalline materials<sup>5</sup>. X-ray powder diffraction is used mostly for qualitative analysis; this is due to the fact that each and every material has a unique diffraction pattern; this implies that each material tends to possess its own characteristic fingerprint. Principles of diffraction are best described by the use of Bragg's law which is shown in equation 3<sup>6</sup>.

$$n\lambda = 2d_{hkl}\sin\theta \quad (2.1)$$

where; n – diffraction order

$\theta$  – diffraction angle

$d_{hkl}$  – spacing between planes

$\lambda$  – diffraction wavelength

X-rays of a chosen wavelength ( $\lambda$ ) are directed to a crystal at a defined angle ( $\theta$ ). Atoms within the crystal are arranged in planes ( $d$ ) which are packed in a unit cell; scattered x-rays that combine constructively produce sharp constructive interference peaks that represent atomic distribution in the structure. This constructive interference leads in a pattern with varying intensities as a function of the scattered angle. This is best illustrated in Figure 2.4.

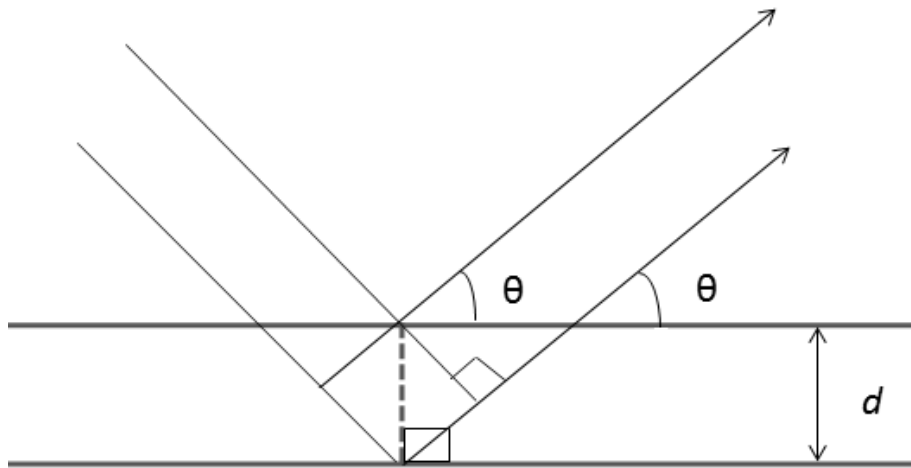


Figure 2.4: Schematic representation that is used for deriving Bragg's law from two parallel planes.

From Figure 2.4 shown above it is relatively easier to derive Bragg's law within a certain  $d$  spacing parameter. Incident waves are scattered by atoms that are arranged in a periodic form, these atoms form different planes. Scattered radiation tends to emerge in a defined direction only when the set of planes are satisfactory enough for Bragg's conditions. The set of planes within a crystal structure are described as Miller indices and these are sets of integer values that are unique to each set. Emerging diffracted X-rays (of varying intensity) do not form from all the planes within the structure; rather they emerge from the structure as a whole which accounts for systematic absences; electron density, thermal vibrations of atoms and the symmetry. The observed diffraction intensity peaks are used to determine the  $d$  spacing

which gives information of the structural make up of a material, i.e the crystal system and the unit cell.

### **2.2.2 Powder X-ray diffraction instruments**

For XRD studies two diffractometers were used and these are; Bruker D2 Phaser and Bruker D8 Advance, these will be further discussed below.

#### a) Bruker D2 Phaser

The D2 Phaser is a desktop diffractometer that uses standard X-ray tubes (in this case cobalt (Co) radiation as the primary source of x-rays). All experiments done in the D2 Phaser were at room temperature. High temperature studies are performed with the different experimental setups. The cobalt specific X-ray radiation is achieved by accelerating an electron beam directed at a cobalt plate within the x-ray tube; this process removes the core electrons from the cobalt plate which are then filled by higher energy electrons and results in the characteristic cobalt X-ray wavelength which is about 1.78897 Å. The D2 Phaser that was used for characterization in this work is shown in Figure 2.5. The samples used in this diffractometer, which are in powder form, were loaded in plastic sample holders with a defined diameter and depth. The detector used (LynxEye PSD detector), is equipped with a nickel filter as the monochromator and the x-ray generator uses a voltage of 30 kV and a current of 10 mA.



Figure 2.5: Bruker D2 phaser diffractometer equipped with cobalt radiation

b) Bruker D8 Advance

Variable temperature studies were done using the Bruker D8 diffractometer equipped with an AntonPaar XRK 900 reaction chamber (Figure 2.6). The X-ray source used was Cu K $\alpha$  with  $\lambda = 1.5406 \text{ \AA}$ . Powder samples were loaded on to a sample holder which was then mounted on the reaction chamber shown in Figure 2.6. The measurements were done from 30 °C to 850 °C (heating rate of 0.3 °C/sec) at  $2\theta = 20^\circ$  to  $110^\circ$ , heating increments were kept at 20 °C for the materials reported in this report. The X-ray generator of the Bruker D8 advance was operated at 40 kV and 40 mA equipped with a Ni monochromator. The reaction chamber was useful in studying thermal stability, thermal expansion and structural changes of the materials.

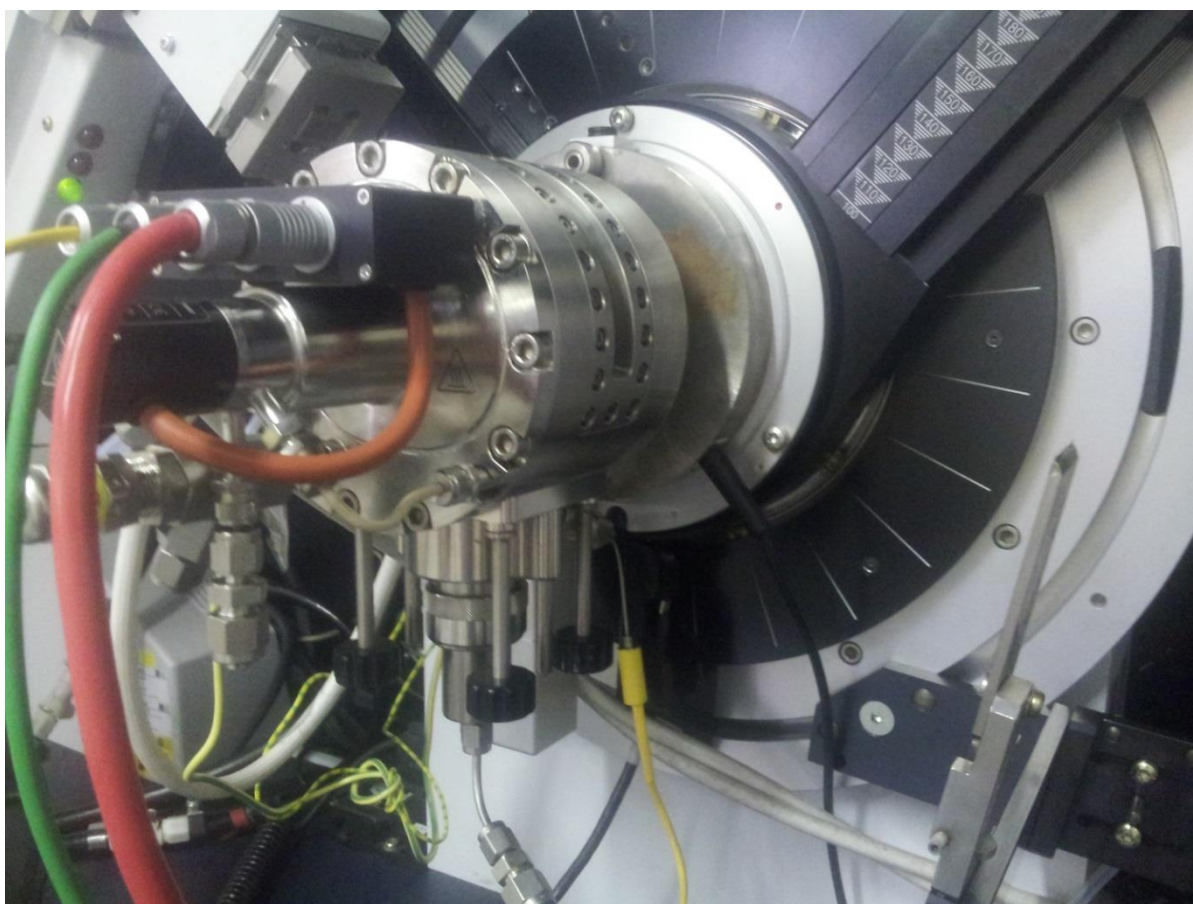


Figure 2.6: The Anton Paar XRK 900 reaction chamber used in a D8 Advance

### **2.2.3 Electron Probe Micro-Analyzer (EPMA)**

Crystal maps of the doped materials were obtained using the CAMECA SX-5-FE EPMA (Figure 2.2.4). This technique was used for quantitative analysis of the products to determine purity; this was coupled with determining if the ions of interest were evenly distributed in the final products for samples in chapter 5.



Figure 2.7: The CAMECA SX-5-FE Electron Probe Micro-Analyzer

### 2.3 Data analysis

The data that was obtained from all PXRD experiments was analyzed using a variety of softwares, the first was the Evaluation Plus software (EVA) <sup>7</sup> which was used for phase identification and the second was Total Pattern Analysis System (TOPAS) <sup>8</sup> which performs which allows for the refinements of PXRD data. For phase identifications the observed PXRD patterns were matched with experimental patterns that exist in a database called PDF-2 2004. Phase identification was followed by structure determination using Rietveld refinement.

### 2.3.1 Rietveld refinement

Rietveld refinement is a technique used in refining crystal structures<sup>9-11</sup>. A starting structural model is required during Rietveld refinement; this acts as a guide that refines parameters which include lattice parameters, atomic positions, atomic displacement parameters and the site occupancy. Sample dependant parameters which may be refined are strain, crystallite size and preferred orientation. In addition to structural parameters there are instrument parameters that are also refined and these include incident profile function, background, peak shape parameters, sample displacement zero point.

A starting model with the same crystal system as the structure is used during a structural refinement because the method is not a structure solution, it is a structure refinement. Therefore a good starting model is required during Rietveld refinement. A least squares minimisation procedure is used in Rietveld refinement, this procedure minimises the difference between the experimental or observed pattern and the pattern calculated from the structure model. Every refinement step is fed back into the program and this in turn improves the solution<sup>11</sup>. The least squares minimisation procedure works to minimise the residual,  $S_y$ :

$$S_y = \sum_i w_i (Y_{o_i} - Y_{c_i})^2 \quad (2.2)$$

where  $Y_{o_i}$  represents the intensity of the observed pattern at the  $i^{\text{th}}$  step and  $Y_{c_i}$  represents the intensity of the calculated pattern at the  $i^{\text{th}}$  step.  $w_i$  is the weight factor, this is given by  $1/Y_{o_i}$ .

The quantification of a Rietveld refinement is by certain Figures of merit namely; weighted profile residual ( $R_{wp}$ ), profile residual ( $R_p$ ), Bragg residual ( $R_B$ ), expected residual ( $R_{exp}$ ) and the goodness of fit ( $\chi^2$ )<sup>5</sup>. The most commonly reported R factor in literature is the  $R_{wp}$  factor (equation 2.3) and this is because the Figure monitors the refinement progress and the numerator is the one being minimised. The Bragg residual (equation 2.4) is the only Figure that depends on the structural parameters, this therefore gives the accuracy of the model of the crystal structure. Another Figure is the expected value,  $R_{exp}$  (equation 2.5), which is defined by the statistics of the refinement<sup>12</sup>. The last Figure that is minimised during a refinement is the chi-squared value,  $\chi^2$  (equation 2.6), and this is a measure of how well the calculated pattern fit with the experimental or observed pattern. Another important Figure of merit to consider is the Durbin-Watson  $d$ -statistic which, during a Rietveld refinement on observed or experimental data, quantifies a serial correlation between adjacent least squares residuals.

$$R_{wp} = \sqrt{\frac{\sum w_i(Y_{oi} - Y_{ci})^2}{\sum w_i(Y_{oi})^2}} \quad (2.3)$$

$$R_B = \frac{\sum |I_{oK} - I_{cK}|}{\sum I_{oK}} \quad (2.4)$$

$$R_{exp} = \sqrt{\frac{\sum(N-P)}{\sum w_i(Y_{oi})^2}} \quad (2.5)$$

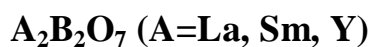
$$\chi^2 = \frac{R_{wp}}{R_{exp}} \quad (2.6)$$

## 2.4 References

1. Smart L. E., Moore E. A., *Solid State Chemistry*, Taylor & Francis Group, 2005.
2. Brinker C. J., Scherer G. W., *Sol-gel Science*, Academic Press, Inc., 1990.
3. Heinike G., *Tribochemistry*, Akademie-Verlag, Berlin, 1984.
4. Jarligo M. O. D., Kang Y-S., Kawasaki A., Watanabe R., *Materials Transactions*, 2004, 45, 8, 2634-2637.
5. Pecharsky V. K., Zavalij P. Y., *Fundamentals of powder diffraction and structural characterization of materials*. Springer, 2009.
6. Bragg W. L., *Proceedings of the Cambridge Philosophical Society*, 1913, pp. 4.
7. DIFFRAC.EVA: *The Next Era in Phase Analysis*, Bruker AXS, Karlsruhe, 2010.
8. Coelho, A. A.; *TOPAS 2007*, V 4.2, Bruker AXS.
9. Rietveld, H.M.; *J. Appl. Crystallogr.* 1969, 2, 65.
10. Nyoni M. S., M.Sc. Dissertation, University of the Witwatersrand, 2013.
11. Payne J. L., PhD Thesis, Durham University, 2011.
12. Rushton M. J. D., *Simulations of glass and ceramic systems for nuclear waste applications*, Thesis, University of London, 2006.

## Chapter 3

### Synthesis and characterization of intrinsic pyrozirconates of the form



#### 3.1 Introduction

Pyrozirconate structures of the form  $A_2Zr_2O_7$  have been extensively studied for the wide variety of properties they exhibit. Pyrozirconates have the space group Fd-3m (no. 227) with eight asymmetric units in a unit cell ( $Z=8$ ) and can be described as oxygen deficient structures with an ordered array of cations<sup>1</sup>. In this  $A_2Zr_2O_7$  structure type there are four distinct Wyckoff positions that house all the ions and one site that is vacant. The sites are; 16d for the  $A^{3+}$  ion, 16c for  $Zr^{4+}$ , 8b and 48f site for  $O^{2-}$  ions and the last site is 8a which is the vacant site<sup>2</sup>. The 48f site is the most interesting site in pyrochlore type structures because this determines the order or disorder of these structures<sup>3</sup>.

Pyrozirconate type structures have of substitutions at the A site and these substitutions lead to a wide variety of physical and chemical properties. Substitutions at the A site not only affect the properties of pyrochlore type structures but can also lead to changes in the structure<sup>3</sup>. The substitutions leading to a classical pyrochlore structure type is dependent on the ionic radius ratio,  $r_A/r_B$  where B is Zr in this case. This ionic radius ratio has led to the construction of a stability field for classic pyrochlores and this was determined by Minervini *et.al*, the stability field of classic pyrochlores lies between 1.46 and 1.72<sup>4</sup>. At values lower than 1.46 the structure tends to become a defect fluorite and at values higher 1.72 the structure changes to a delta phase which will not be discussed further as it is not repeatedly encountered. The cation radius of the A site is thus important as it determines whether a material will adopt a pyrochlore or defect fluorite structure type. A wide range of properties arise in these pyrozirconates due to the substitutions that occur. Properties arising from these materials are; superconductivity, minimal thermal conductivity, luminescence, immobilizing hosts in nuclear waste and high ionic conductivity to name a few<sup>5-7</sup>.

Most of the pyrozirconate structures exhibit the fore-mentioned properties at high temperatures and this implies that thermal expansion coefficient would be an important factor to consider in choosing a material for a certain function<sup>1</sup>. High oxide ion conductivity is a property that is used in solid oxide fuel cells and in these devices Pyrozirconate materials are

used as solid electrolytes <sup>8</sup>. As it was mentioned, TECs of the materials are important as they give an understanding of the thermoresponsive properties of the materials. In this chapter the thermal expansion coefficients of  $\text{La}_2\text{Zr}_2\text{O}_7$ ,  $\text{Sm}_2\text{Zr}_2\text{O}_7$  and  $\text{Y}_2\text{Zr}_2\text{O}_7$  are determined and their comparison gives a better understanding of the effects that the cationic radius of the  $\text{A}^{3+}$  on the TEC.

## 3.2 Experimental

### 3.2.1 Materials used

The chemicals used were all of analytical grade with high percentage purity.  $\text{La}(\text{NO}_3)_3 \cdot 6\text{H}_2\text{O}$  (99%),  $\text{Sm}(\text{NO}_3)_3 \cdot 6\text{H}_2\text{O}$  (99.9%) and  $\text{Y}(\text{NO}_3)_3 \cdot \text{H}_2\text{O}$  (99.8%) were purchased from Sigma-Aldrich; these were used as the source of the A cation in  $\text{A}_2\text{Zr}_2\text{O}_7$  pyrochlores. The source of the B cation was  $\text{Zr}(\text{OC}_3\text{H}_7)_4$  (70%) and this was purchased from Merck. Isopropyl alcohol, purchased at Merck, was used as solvent in the experimental approach. There was no pretreatment of the materials.

### 3.2.2 Sol-gel synthesis

A total of three materials were synthesized using the sol-gel method and these were; (a)  $\text{La}_2\text{Zr}_2\text{O}_7$ , (b)  $\text{Sm}_2\text{Zr}_2\text{O}_7$  and (c)  $\text{Y}_2\text{Zr}_2\text{O}_7$ . The total mass of each material synthesized was estimated to be 1g.

a)  $\text{La}_2\text{Zr}_2\text{O}_7$

$\text{La}(\text{NO}_3)_3 \cdot 6\text{H}_2\text{O}$  (1.531 g, 1.75 mmol) was dissolved separately in 10 ml isopropanol. In a different beaker  $\text{Zr}(\text{OC}_3\text{H}_7)_4$  (1.637 g, 1.75 mmol) was dissolved in 10 ml isopropanol. The salt solution containing  $\text{La}(\text{NO}_3)_3$  was then gradually added into the isopropoxide solution stirred and stirred give a homogenous mixture.

b)  $\text{Sm}_2\text{Zr}_2\text{O}_7$

$\text{Sm}(\text{NO}_3)_3 \cdot 6\text{H}_2\text{O}$  (1.493 g, 3.36 mmol) was dissolved in 10 ml isopropanol and in a different beaker  $\text{Zr}(\text{OC}_3\text{H}_7)_4$  (1.573 g, 3.36 mmol) was dissolved in 10 ml isopropanol and the steps performed for  $\text{La}_2\text{Zr}_2\text{O}_7$  were followed

c)  $\text{Y}_2\text{Zr}_2\text{O}_7$

The synthetic route used for the above materials was followed for the synthesis of this material. The amounts used were as follows;  $\text{Y}(\text{NO}_3)_3 \cdot 6\text{H}_2\text{O}$  (1.624 g, 2.12 mmol) and  $\text{Zr}(\text{OC}_3\text{H}_7)_4$  (1.984 g, 2.12mmol).

The final resulting products were then calcined at 900 °C in a muffle furnace for 8 h at a heating rate of 10 °C/min. The resulting powders were homogenized using a pestle and mortar until fine powders resulted. The phases of the materials were identified using powder X-ray diffraction; this was done using the Bruker D2 Phaser using Co K $\alpha$  radiation (1.78897 Å). The measurement range was from 2 $\theta$ = 10° to 90° at room temperature. This was followed by phase identification of the final products using Bruker-AXS Evaluation Package (EVA) equipped with ICDD PDF 2 database. Rietveld refinements of the materials were performed Topas. For lattice thermal expansion studies the Bruker D8 Discover was used, the instrument uses Cu K $\alpha$  radiation (1.5406 Å) and the temperature range was from 30 °C to 850 °C.

### 3.3 Results and Discussion

#### 3.3.1 Powder Xray diffraction

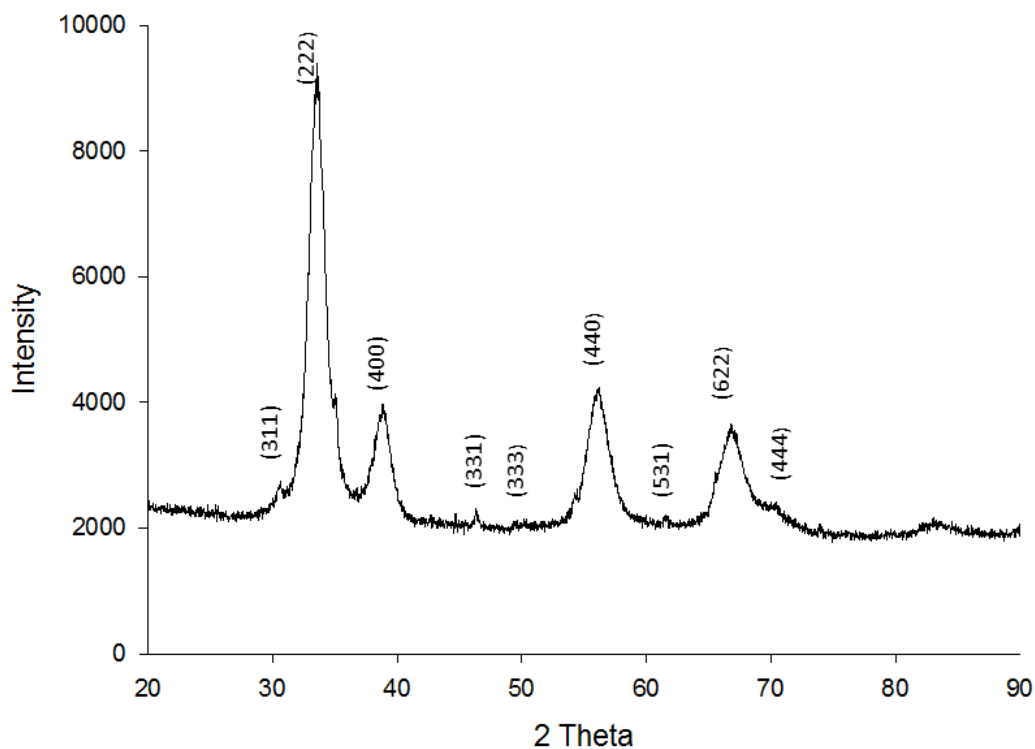
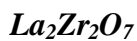


Figure 3.1 Powder X-ray diffraction pattern of La<sub>2</sub>Zr<sub>2</sub>O<sub>7</sub> at ambient temperature measured at  $\lambda = 1.78897$  Å

Figure 3.1 shows the PXRD pattern of  $\text{La}_2\text{Zr}_2\text{O}_7$  and according to the scan the material is indexed as a pyrochlore of the general formula  $\text{A}_2\text{B}_2\text{O}_7$ , this is because of the superlattice peaks that exist at  $2\theta = 30.572^\circ$  (311),  $46.424^\circ$  (331),  $50.256^\circ$  (333) and  $61.492^\circ$  (531). This therefore implies that the  $\text{La}_2\text{Zr}_2\text{O}_7$  synthesized has the space group  $\text{Fd-}3\text{m}$  which represents a cubic pyrochlore structure. The phases of the material were further confirmed by comparison to reference patterns in the ICDD using the program EVA. This indicated that the material obtained was single phase  $\text{La}_2\text{Zr}_2\text{O}_7$  with a cubic unit cell. The stability range of pyrochlores as calculated by Mervini *et. al* suggests that pyrochlores only exist when the A:B ratio of the metals lies between 1.46 and 1.78<sup>4</sup>. The ionic radius of  $\text{La}^{3+}$  that has a coordination number of 8 is 1.16,  $\text{Zr}^{4+}$  with a coordination number of 6 has an ionic radius that is 0.72 thus making the  $\text{La}^{3+}/\text{Zr}^{4+}$  ratio to be 1.61 and this falls within the stability region of pyrochlores. This further suggests that  $\text{La}_2\text{Zr}_2\text{O}_7$  is an ordered pyrochlore.

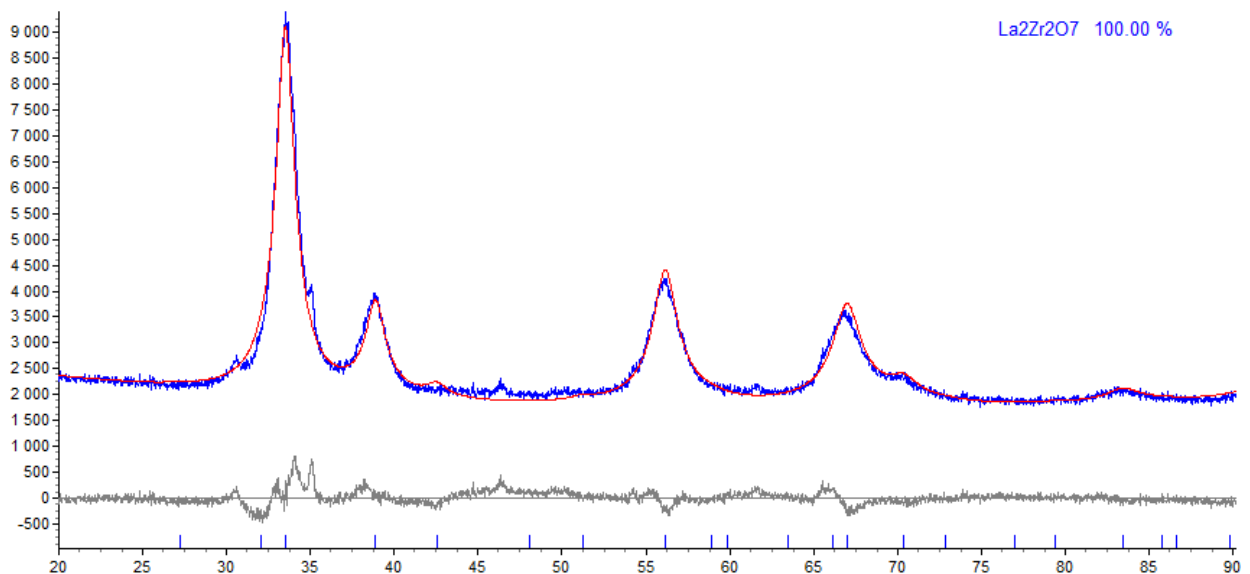


Figure 3.2 PXRD profile plots of  $\text{La}_2\text{Zr}_2\text{O}_7$  as refined by Reitveld using TOPAS; the blue plot represents the observed pattern, red shows the calculated plot and grey is the difference plot.

Figure 3.2 above represents the Rietveld refinement of  $\text{La}_2\text{Zr}_2\text{O}_7$  and this was calculated using a starting structure model of  $\text{La}_2\text{Zr}_2\text{O}_7$  as a pyrochlore. The starting structure was obtained from the Inorganic Crystal Structure Database (ICSD). The structure was fitted using Pearson-VII peak type. The lattice parameter of this phase was calculated by the program and found to be  $10.785 \text{ \AA}$ , this is a further confirmation that  $\text{La}_2\text{Zr}_2\text{O}_7$  as synthesized was a pyrochlore. This value is in good agreement with values published by Kutty *et. al*

which was  $10.7997 \text{ \AA}$ . The initial structure was refined by Rietveld method using the program Topas.

Table 3.1: Structural model of  $\text{La}_2\text{Zr}_2\text{O}_6\text{O}'$ .

Site	Wyckoff position	x	y	z
La	16d	0.500	0.500	0.500
Zr	16c	0.000	0.000	0.000
O	48f	0.344	0.125	0.125
O'	8b	0.375	0.375	0.375

Table 3.1 shows the refined crystallographic parameters of  $\text{La}_2\text{Zr}_2\text{O}_6\text{O}'$  showing the fractional coordinates of the structure. As shown the 48f positional parameter x is 0.344 and this satisfies that of a disordered pyrochlore. According to Subramanian *et.al* the 48f x positional parameter of an ideal pyrochlore lies between 0.3125 and 0.375, this determines the order of the oxide ions in the 48f position. As the value approaches 0.3125 the  $\text{BO}_6$  octahedra in pyrochlores tends to be distorted, towards 0.375 it starts being more ordered. When the structure was visualised using the program CrystalMaker it was clear that the oxide ions in position 48f were not completely ordered. This is illustrated in Figure 3.3.

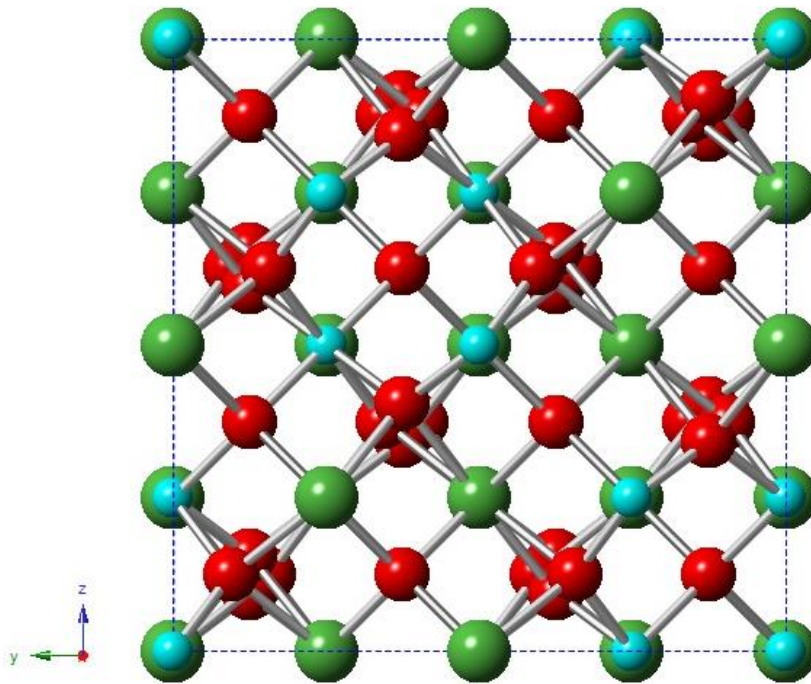


Figure 3.3 Cubic unit cell of  $\text{La}_2\text{Zr}_2\text{O}_6\text{O}'$  viewed along the a-axis, the 48f x positional parameter is 0.344. Green spheres represent  $\text{La}^{3+}$  the blue spheres are  $\text{Zr}^{4+}$  and the red spheres are  $\text{O}^{2-}$ .

Figure 3.3 above shows the pyrochlore structure of  $\text{La}_2\text{Zr}_2\text{O}_6\text{O}'$  and from the Figure it is clear that oxide ions have two distinct positions. The ordered oxide ions are on the 8b site with the same fractional coordinates, the disordered oxide ions are associated with the 48f position and this is associated with the oxide positional parameter. The value is 0.344 and this explains why the oxide ions are disordered leading to a distorted  $\text{BO}_6$  octahedron. The oxygen positional parameter determines the structural stability of pyrochlore materials,  $\text{La}_2\text{Zr}_2\text{O}_6\text{O}'$  as synthesized is a disordered pyrochlore.

## $Sm_2Zr_2O_7$

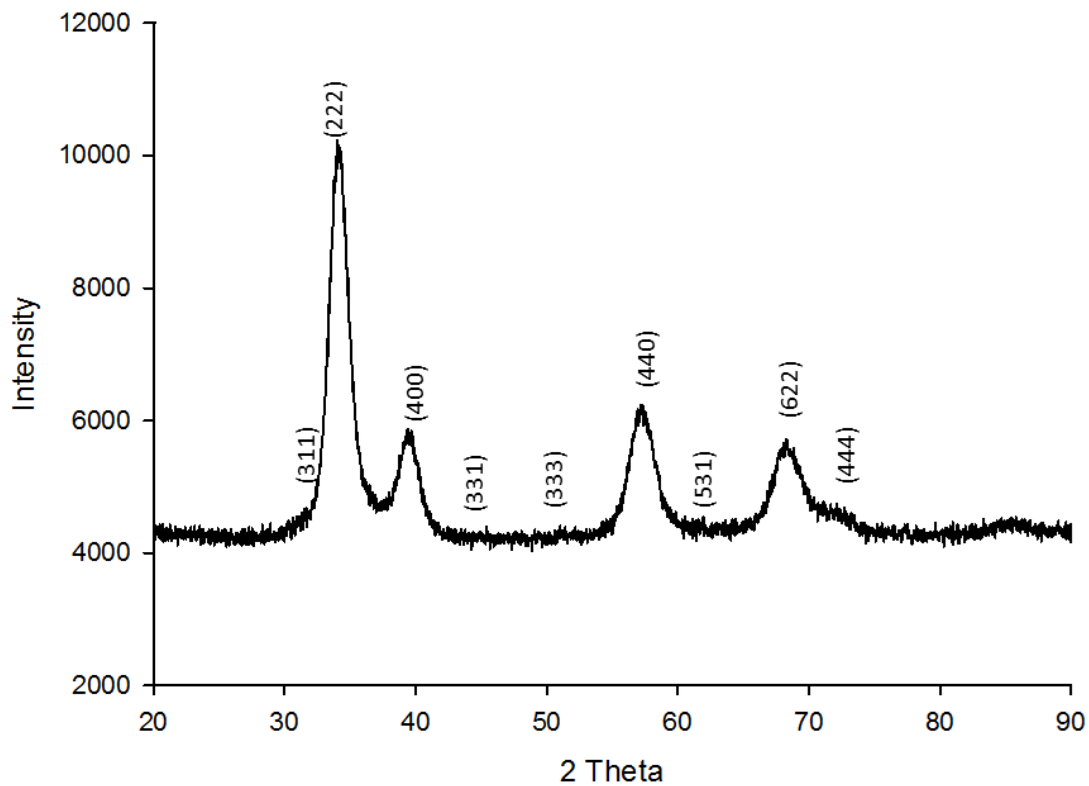


Figure 3.4: Powder X-ray diffraction pattern of  $Sm_2Zr_2O_7$  measured at room temperature,  $\lambda = 1.78897 \text{ \AA}$ .

Figure 3.4 shows the PXRD pattern of  $Sm_2Zr_2O_7$  as synthesized by the sol-gel method. The material was not fully crystalline hence superlattice peaks are faint as compared to  $La_2Zr_2O_7$ ; the presence of these faint peaks is a clear indicator that  $Sm_2Zr_2O_7$  as synthesized had a pyrochlore structure type of the form  $A_2B_2O_7$ . Phase stability diagrams and postulations derived by Mervini have suggested that pyrochlore type structures are only stable when the  $A^{3+}/B^{4+}$  ratio lies between 1.46 and 1.78. The ionic radius of  $Sm^{3+}$  in a system with a coordination number of 8 is  $1.079 \text{ \AA}$  while that of  $Zr^{4+}$  is  $0.72 \text{ \AA}$ , this makes the  $Sm^{3+}/Zr^{4+}$  ratio 1.50 and this therefore suggests  $Sm_2Zr_2O_7$  has a pyrochlore structure type.

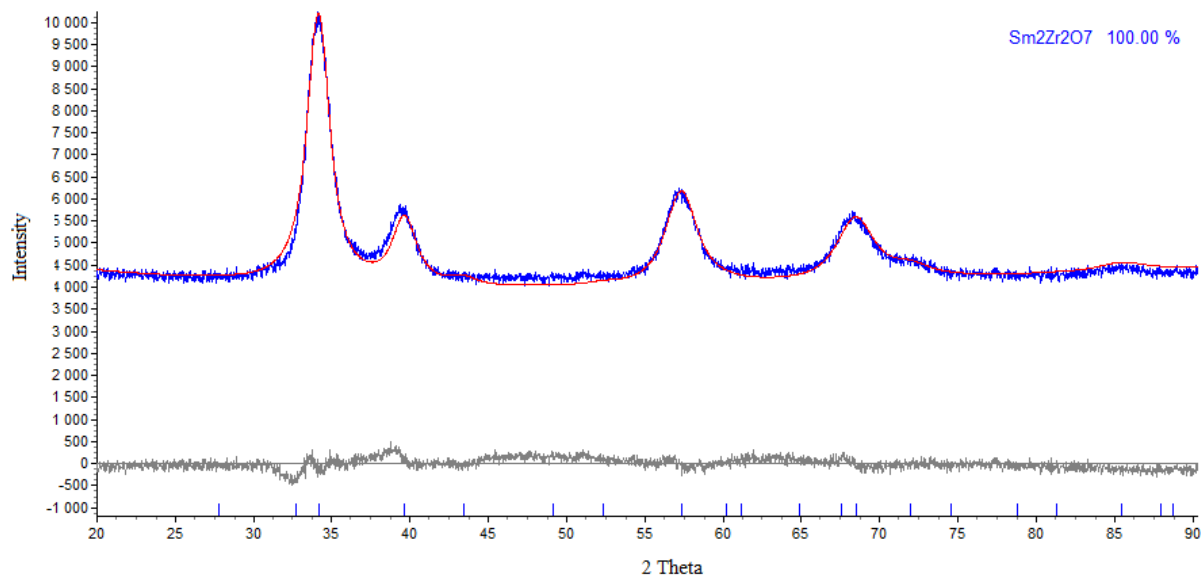


Figure 3.5: Rietveld refined profile plots of  $\text{Sm}_2\text{Zr}_2\text{O}_7$  as refined using TOPAS; the blue line is the measured pattern, red is the calculated and grey is the difference between the measured and calculated

The Rietveld refinement shown in Figure 3.5 was performed using a refined starting structure model with a pyrochlore structure type of the form  $\text{Sm}_2\text{Zr}_2\text{O}_7$  and this was in good agreement with the measured pattern. It shows that the material is phase pure and has no impurities or precursor materials. The lattice parameter as calculated was found to be 10.546 Å. The lattice parameter determined for  $\text{Sm}_2\text{Zr}_2\text{O}_7$  was similar to that determined by Kutty *et.al* which was 10.5922 Å.

Table 3.2 Wyckoff positions and fractional coordinates of  $\text{Sm}_2\text{Zr}_2\text{O}_7$

Site	Wyckoff position	x	y	z
Sm	16d	0.500	0.500	0.500
Zr	16c	0.000	0.000	0.000
O	48f	0.347	0.125	0.125
O'	8b	0.375	0.375	0.375

Table 3.2 shows that all the ions are in special positions except the 48f oxygen anion. The 48f positional parameter of  $\text{Sm}_2\text{Zr}_2\text{O}_7$  was determined to be 0.347 and this satisfies the category

of ordered pyrochlore structures. The  $\text{ZrO}_6$  octahedron that exists in this structure is distorted with some disorder associated with the oxygen at the 48f site. This is visualized in Figure 3.6.

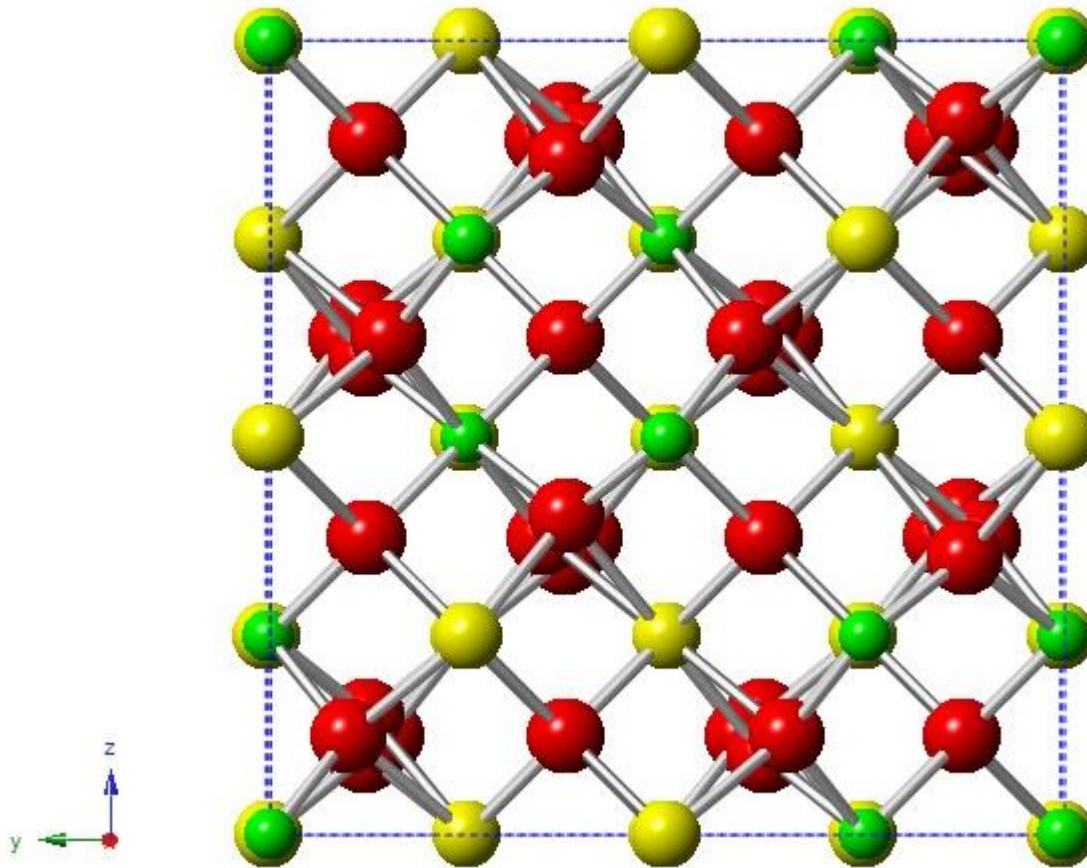


Figure 3.6: Cubic unit cell of  $\text{Sm}_2\text{Zr}_2\text{O}_7$  viewed along the  $a$ -axis. Green spheres are  $\text{Zr}^{4+}$ , yellow spheres represent  $\text{Sm}^{3+}$  and red spheres are  $\text{O}^{2-}$  ions

Figure 3.6 above clearly shows oxygen anions that are not ordered and these are at the 48f position. This is an indication that slight variations in the 48f positional parameter leads to changes in the structure and this has an effect in the physical and chemical properties of the material. Oxygen anions at position 8b are ordered and all the cations are ordered as well, so the 48f positional parameter plays a major role in determining the structure for pyrochlore materials of the chemical composition  $\text{A}_2\text{B}_2\text{O}_7$ .

## $Y_2Zr_2O_7$

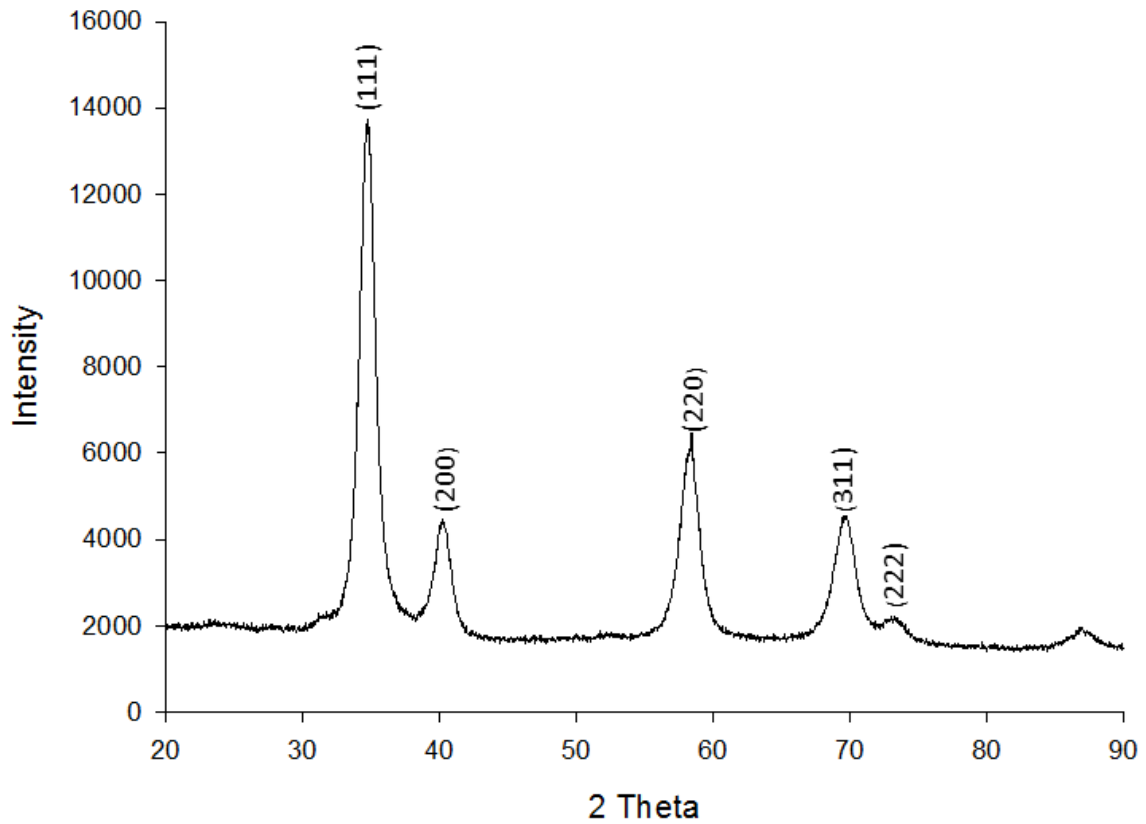


Figure 3.7: Powder X-ray diffraction pattern of  $Y_2Zr_2O_7$  at ambient temperature,  $\lambda = 1.78897$  Å.

Figure 3.7 shows the PXRD pattern of  $Y_2Zr_2O_7$  as recorded at room temperature, from the Figure it is clear that superlattice peaks are absent which indicates that the reflections present are not that of a pyrochlore but a defect fluorite structure type. Therefore they were indexed using Fm3m space group (No. 225). The defect fluorite peaks were indexed using EVA program. This pattern was in perfect agreement with a pattern that was presented by Horuichi *et.al*<sup>10</sup> even though they used Cu K $\alpha$  radiation which leads to minor changes in the 2 theta values.

The stability field of ordered pyrochlores as mentioned before is proposed to lie between a ratio of 1.46-1.78 and this is based on the cationic radius ratio of the  $A^{3+}$  and  $B^{4+}$  ions. With the  $Y_2Zr_2O_7$  structure type the  $Y^{3+}$  cation has an ionic radius of 1.019 Å and that of  $Zr^{4+}$  is 0.84 Å, both the cations have a coordination number of 8 because  $Y^{3+}$  and  $Zr^{4+}$  share a Wyckoff position in defect fluorite type structures. This then makes the  $Y^{3+}/Zr^{4+}$  cation radius

ratio to be 1.21 and this does not lie within the stability field of pyrochlores, which further confirms that  $Y_2Zr_2O_7$  has a defect fluorite structure type.

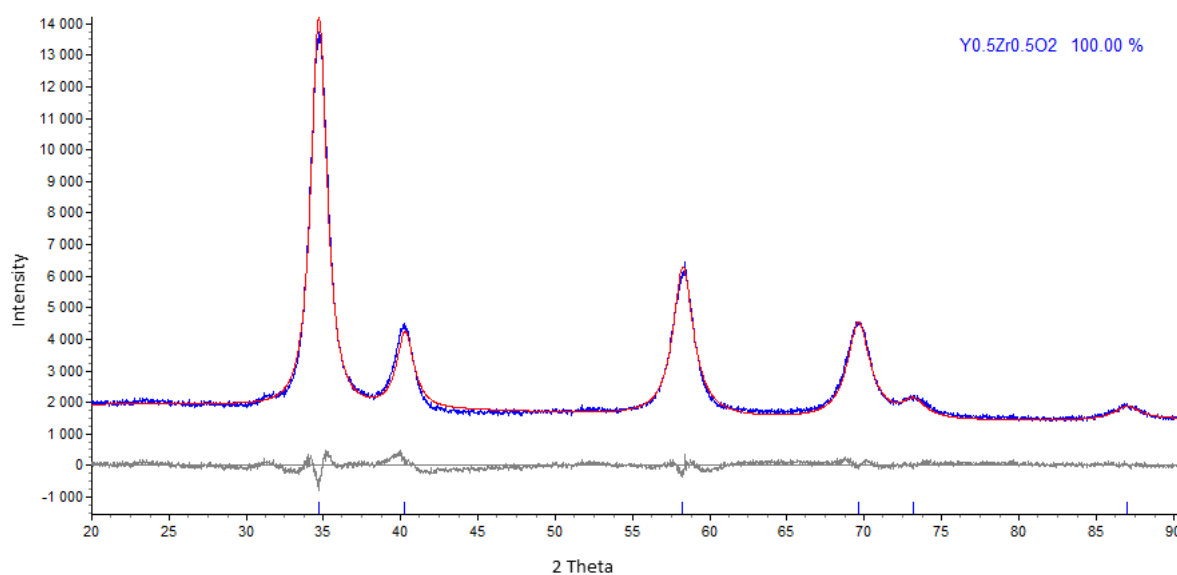


Figure 3.8 Rietveld refined profile plots of  $Y_2Zr_2O_7$  as refined using TOPAS; blue peak represents the observed pattern, red is the calculated and grey is the difference.

The Rietveld refinement of this structure type was performed using a starting structure model of a defect fluorite with the structure type  $Y_{0.5}Zr_{0.5}O_2$  with the space group  $Fm-3m$  (No. 225). As indicated in Figure 3.8 the calculated pattern was in good agreement with the observed pattern, which suggests that the synthesized material was a defect fluorite. The refined lattice parameter of this material was found to be 5.20 Å. Lattice parameters calculated by Horuichi *et.al* was found to be 5.21 Å and this value is in good agreement with the one determined in this study.

Table 3.3 Wyckoff positions and fractional coordinates of  $Y_2Zr_2O_7$

Site	Wyckoff position	x	y	z
$Y^{3+}$	4a	0	0	0
$Zr^{4+}$	4a	0	0	0
$O^{2-}$	8c	0.25	0.25	0.25

Table 3.3 shows that the A ( $Y^{3+}$ ) and the B ( $Zr^{4+}$ ) cations share a position in defect fluorites structures while the oxide has a distinct position, this implies that defect fluorite structures have only two Wyckoff positions. The only variable parameter in defect fluorite type structures is the lattice parameter as they have no oxygen positional parameter, which shows that during refinements only the lattice parameter is refined.

Pyrochlore type structures of the form  $A_2B_2O_7$  are ordered, meaning that each cation occupies a distinct position. In defect fluorite structures the  $A^{3+}$  and  $B^{4+}$  cations which are at position 16d and 16c share positions, the implication of this process is that about half of the  $A^{3+}$  cations will be at the 16c site while half of the  $B^{4+}$  cations migrate to the 16d site. This results in the 16c and 16d sites being equivalent, thus converging and forming only one Wyckoff position because both sites have the same constituents, this is the 4a site. As this happens with the cations, the oxide anions also converge and the oxide anions at the 48f site migrate to the vacancy that exists in position 8a and form one position (8c site) because all the oxygen anions are equivalent.

The Figure below shows a structure of  $Y_2Zr_2O_7$  as a defect fluorite type structure, the Figure shows it that at 4a site there's an equal sharing between the  $Y^{3+}$  and the  $Zr^{4+}$  cations. The 8c site is occupied by  $O^{2-}$  anions which are equivalent disordered on the site. The result is that the lattice parameter of this structure is half that of a pyrochlore type structure with  $A_2B_2O_7$  formula because the cations are not alternating but instead are disordered.

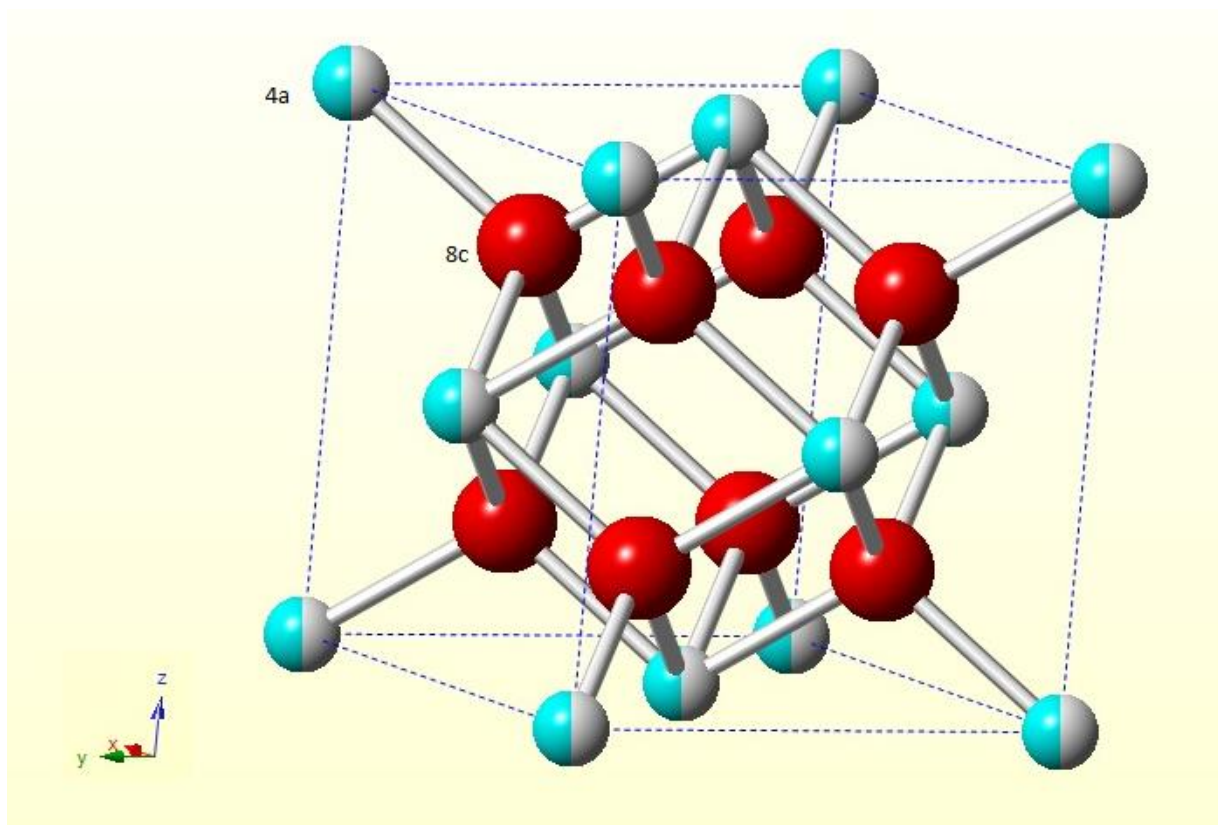


Figure 3.9 Cubic unit cell of  $\text{Y}_2\text{Zr}_2\text{O}_7$  with the defect fluorite structure type showing the Wyckoff positions of the ions. For the two toned sphere the blue color represents  $\text{Zr}^{4+}$  and the grey part is  $\text{Y}^{3+}$ , the red sphere represents  $\text{O}^{2-}$ .

### 3.3.2 High temperature Powder X-ray diffraction studies

This part of the study investigated the thermal expansion of the materials synthesized to compare what the effects of the  $\text{A}^{3+}$  cation in the  $\text{A}_2\text{Zr}_2\text{O}_7$  pyrochlore structure type. The PXRD patterns of the materials had no evidence of phase transformations in the temperature range 303 K to 1123 K. Pyrochlores of the structure type  $\text{A}_2\text{Zr}_2\text{O}_7$  repeatedly have order to disorder transformations at temperatures greater than 1773 K, at these high temperatures they transition from being ordered pyrochlore structures to defect fluorite type structures<sup>3</sup>. In a study conducted by Michel *et.al*<sup>11</sup> it was found that  $\text{La}_2\text{Zr}_2\text{O}_7$  does not undergo any high temperature phase transformation while  $\text{Sm}_2\text{Zr}_2\text{O}_7$  undergoes order to disorder transformations at 2273 K.  $\text{Y}_2\text{Zr}_2\text{O}_7$  is not expected to undergo any phase transformations because it has a defect fluorite structure as synthesized, this implies that it already possess a disordered structure<sup>11</sup>.

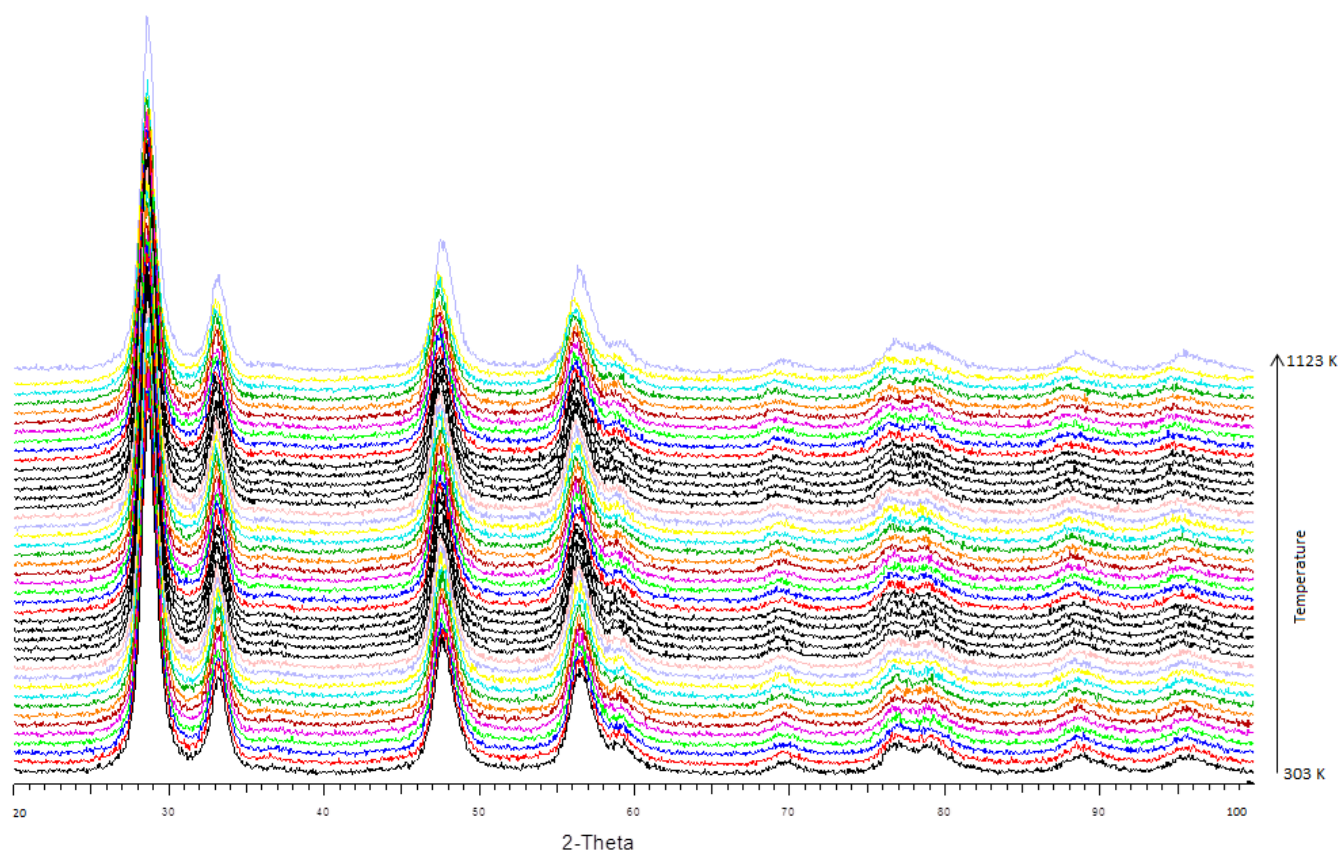


Figure 3.10 Variable-temperature patterns of  $\text{La}_2\text{Zr}_2\text{O}_7$  recorded from 303 K to 1123 K. This was recorded at 50 K increments using Cu  $K\alpha$  radiation.

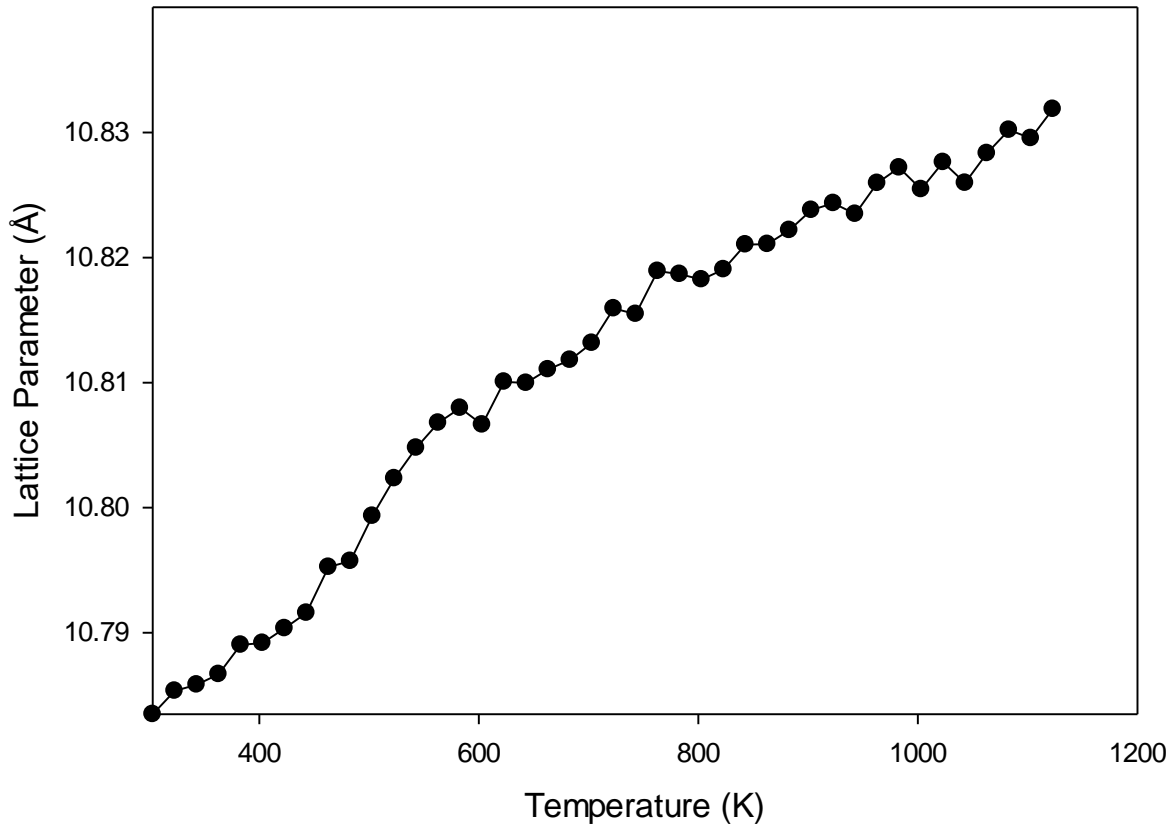


Figure 3.11 Lattice parameter obtained by Rietveld refinement against temperature plot for  $\text{La}_2\text{Zr}_2\text{O}_7$  with the line used to fit the points

Figure 3.11 is an indication that the peaks from the vt-PXRD (Figure 3.10) were shifting to lower angles and this represents thermal expansion because peaks shifting to lower angles indicate that there's an increase in the interplanar spacing ( $d$ ) which would then lead to the unit cell parameter increasing. The thermal expansion coefficient of  $\text{La}_2\text{Zr}_2\text{O}_7$  was calculated using the following equation;

$$\alpha_a = \frac{1}{a_{303}} \left( \frac{\partial a}{\partial T} \right) \quad (3.1)$$

From the equation  $\frac{\partial a}{\partial T}$  represents the slope of the graph that is calculated from a linear fit on the graph and  $a_{303}$  represents the lattice parameter at 303 K. The thermal expansion of  $\text{La}_2\text{Zr}_2\text{O}_7$  as calculated using equation 3.1 was found to be  $5.462 \times 10^{-6} \text{ K}^{-1}$

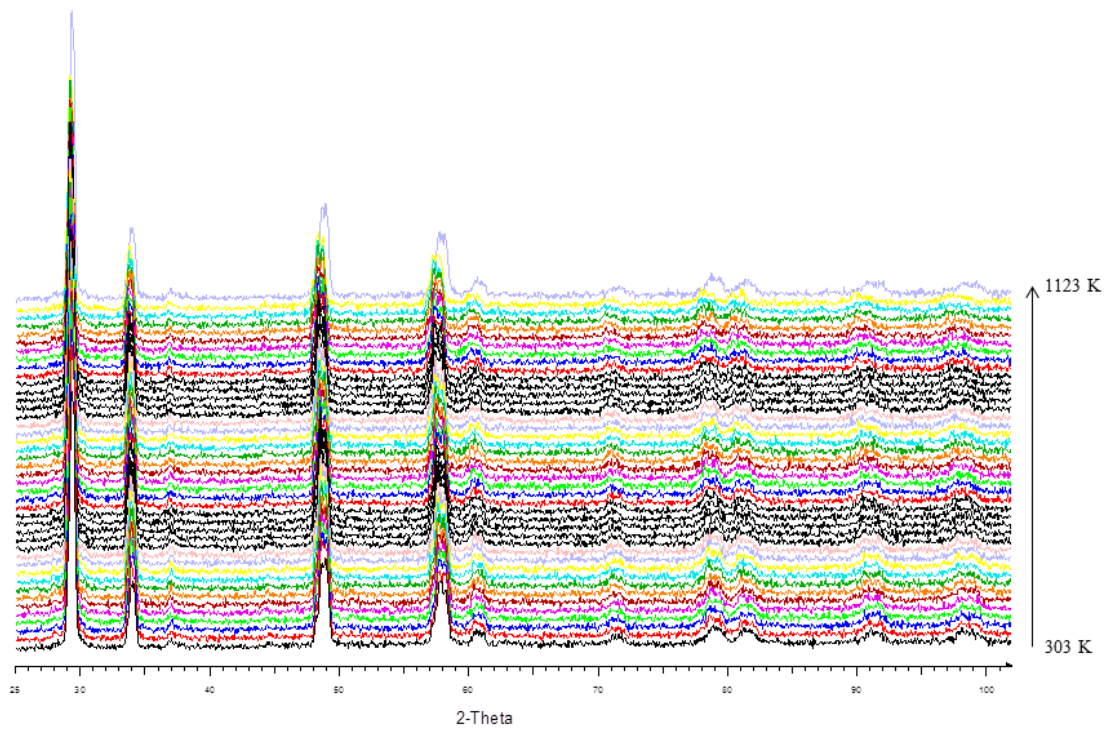


Figure 3.12 Variable temperature patterns of  $\text{Sm}_2\text{Zr}_2\text{O}_7$  measured from 303 K to 1123 K,  $\lambda=1.54 \text{ \AA}$ .

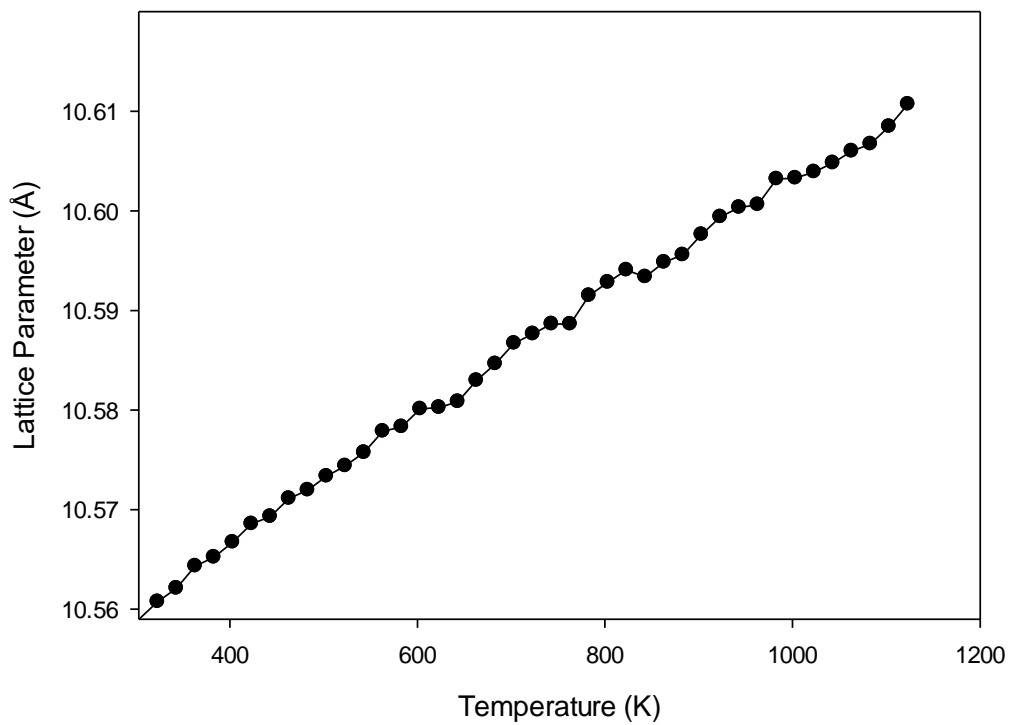


Figure 3.13 Lattice parameter against temperature plot of  $\text{Sm}_2\text{Zr}_2\text{O}_7$  with the line used to fit the points

The peaks shown in Figure 3.12 are much sharper than that of  $\text{La}_2\text{Zr}_2\text{O}_7$  which shows that the material was more crystalline when it was recorded using vt-PXRD. From the Figure there is also evidence of peaks shifting to the lower  $2\theta$  angles which shows that the material exhibits low thermal expansion. The thermal expansion coefficient of this material was calculated using the slope from the Figure 3.13.

A linear fit was incorporated and a slope of the graph was determined, this was followed by using equation 3.1 to determine the thermal expansion coefficient. The TEC of  $\text{Sm}_2\text{Zr}_2\text{O}_7$  was calculated and the value was  $5.764 \times 10^{-6} \text{ K}^{-1}$  which is classified as low thermal expansion.

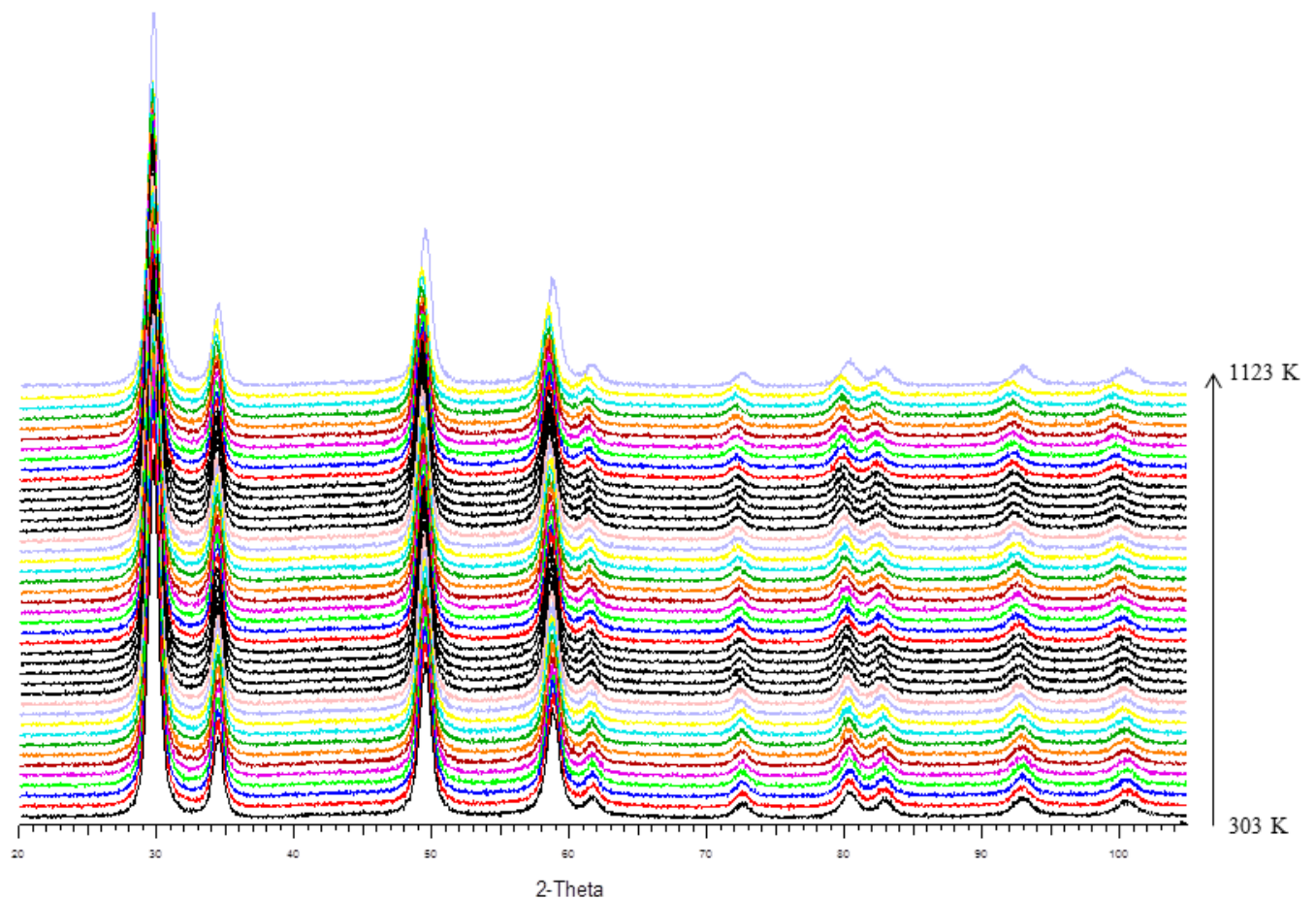


Figure 3.14 Variable temperature patterns of  $\text{Y}_2\text{Zr}_2\text{O}_7$  measured from 303 K to 1123 K

The Figure above indicates that there is low thermal expansion in  $\text{Y}_2\text{Zr}_2\text{O}_7$  and this evident because of the peak shifting that occurs with an increase in temperature. The thermal expansion in this material is shown in Figure 3.15 where the lattice parameter is plotted

against temperature. The Figure shows that the material also exhibits low thermal expansion as  $\text{La}_2\text{Zr}_2\text{O}_7$

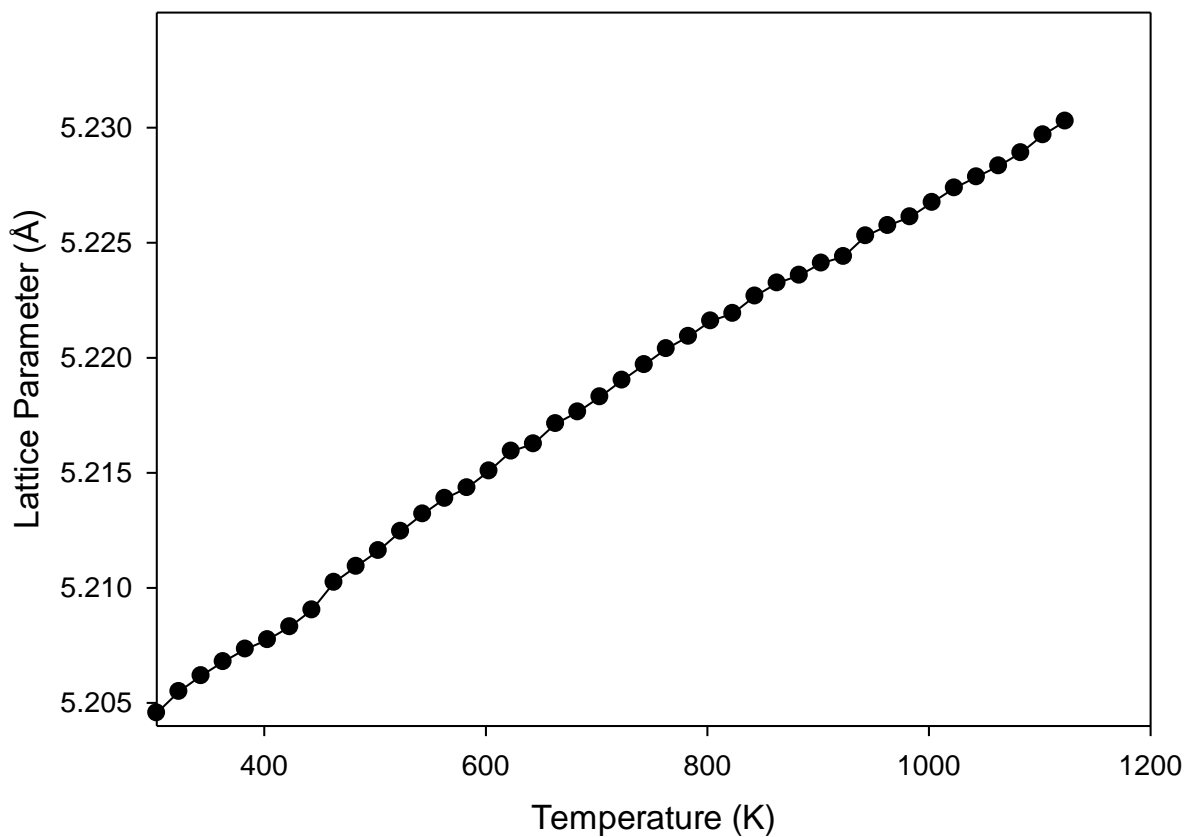


Figure 3.15 Lattice parameter vs temperature line scatter plot for  $\text{Y}_2\text{Zr}_2\text{O}_7$

The thermal expansion of this material was found to be  $5.987 \times 10^{-6} \text{ K}^{-1}$  and this is classified as low thermal expansion.

Kutty *et.al* determined the thermal expansion coefficient of Pyrozirconates of the lanthanide family. The conclusion was that as the ionic radii of lanthanides decreases due to lanthanide contraction the Madelung energy decreases and this is coupled by an increase in thermal expansion of materials. The Madelung energy represents the total lattice energy which is the sum of the attractive and repulsive forces (electrostatic energy) in a material <sup>12-14</sup>. In this case

$\text{La}^{3+}$  has a greater ionic radius than  $\text{Sm}^{3+}$  and  $\text{Y}^{3+}$ , as a result the TEC of  $\text{La}_2\text{Zr}_2\text{O}_7$  is lower than that of the other materials. So the results obtained for the TEC's of the materials investigated in this study are in good agreement with postulations made by Kutty *et.al.*

### 3.4 General conclusions

The pyrozoirconates ( $\text{La}_2\text{Zr}_2\text{O}_7$ ,  $\text{Sm}_2\text{Zr}_2\text{O}_7$  and  $\text{Y}_2\text{Zr}_2\text{O}_7$ ) were successfully synthesized and from the study it was clear that cationic radius affects the structure of a material.  $\text{La}_2\text{Zr}_2\text{O}_7$  and  $\text{Sm}_2\text{Zr}_2\text{O}_7$  possess a pyrochlore structure type with  $Fd-3m$  as the space group (No. 227).  $\text{Y}_2\text{Zr}_2\text{O}_7$  on the other hand had the similar  $\text{A}_2\text{B}_2\text{O}_7$  stoichiometry but possessed a fluorite structure type, space group  $Fm3m$  (No. 225), the PXRD pattern of this material was similar to that of yttria-stabilized zirconia and this meant that the structure had approximately half the lattice parameter of classic pyrochlore structures. The effects of the A site cationic radius on the coefficient of thermal expansion were studied and this showed that there was a significant effect on the TEC. The difference in linearity of Figure 3.11 from Figure 3.13 and 3.15 was due to some inconsistencies that came from the Rietveld refinement.  $\text{La}_2\text{Zr}_2\text{O}_7$  had the lowest TEC, followed by  $\text{Sm}_2\text{Zr}_2\text{O}_7$  and  $\text{Y}_2\text{Zr}_2\text{O}_7$  had the highest TEC. The calculated TEC of a material is affected by the ionic radius of the  $\text{A}^{3+}$  cation in the sense that as the ionic radius decreases the total lattice energy decreases. The lattice energy is the sum of the attractive and repulsive forces that exist in a structure, as these forces decrease the TEC is expected to decrease. The ionic sizes of  $\text{La}^{3+}$ ,  $\text{Sm}^{3+}$  and  $\text{Y}^{3+}$  in an environment where the coordination number is eight are; 1.16 Å, 1.079 Å and 1.019 Å.  $\text{La}^{3+}$  has the highest ionic radius and this means that it is expected to have the lowest TEC and that was shown successfully in the systematic study.  $\text{Y}^{3+}$ , which has the lowest ionic radius, had the highest TEC.

### 3.5 References

1. Feng J., Xiao B., Zhou R., and Pan W., *J. Appl. Phys.*, 2012, 111, 103535.
2. Maram P. S., Ushakov S.V., Weber R. J. K., Benmore C.J and Navrotsky A., *J. Am. Ceram. Soc.*, 2014, 1–8.
3. Subramanian M. A., Aravamuda G., and Subba Rao G. V., *Progress in solid state chemistry*, 1983, 15, 2, 55-143.
4. Minervini L, and Grimes R. W., *Journal of the American Ceramic Society*, 2000, 83, 1873.

5. Sickafus K. E., Minervini L., Grimes R. W., Valdez J. A., Ishimaru M., Li F., McClellan K. J., and Hartmann T., *Science*, 2000, 289, 784.
6. Tabira Y., Withers R. L., Minervini L., and Grimes R. W., *J. Solid State Chem.*, 2000, 153, 16.
7. Lian J., Zu X. T., Kutty K., Chen J., Wang L. M., and Ewing R. C., *Phys. Rev.*, 2002, B 66, 54108.
8. Wang J. D., Pan W., and Xu Q., *Rare Met. Mater. Eng.*, 2005, 34(Suppl 1), 581.
9. Kutty K. V. G., Rajagopalan S., Mathews C. K. and Varadaraju U. V., *Materials Research Bulletin*, 1994 29, 7, 759-766.
10. Horiuchi H., Schultz A. J., Leung P. C., and Williams J. M., *Acta Crystallographica B*, 1984, 40, 367–372.
11. Michel D., Perez y Jorba M. and Collongues R., *Materials Research Bulletin*, 1974, 9, 11, 1457-1468.
12. Zhang Y. H., Xie M., Zhou F., Cui X. Z., Lei X. G., and Song X. W., *Ceram. Int.*, 2014, 40, 9151–9157.
13. Guo L., Zhang Y., and Ye F. X., *J. Am. Ceram. Soc.*, 2015, 98, 1013–1018.
14. Wan C. L., Qu Z. X., Du A. B., and Pan W., *Acta Mater.*, 2009, 57, 4782–4789.

## Chapter 4

### Mechanochemical synthesis and characterization of $\text{La}_2\text{Zr}_2\text{O}_7$

#### 4.1 Introduction

Lanthanum zirconate,  $\text{La}_2\text{Zr}_2\text{O}_7$ , is a material with a cubic pyrochlore structure that has been studied over the years because of the properties it possesses. These properties are; high melting point, ability to accommodate dopants, low thermal conductivity, high oxide conductivity and no phase transitions at either room temperature or operating temperature<sup>1-4</sup>. These properties make  $\text{La}_2\text{Zr}_2\text{O}_7$  a functional material that finds uses in thermal barrier coatings, solid oxide fuel cells, high temperature catalysis and the immobilization of actinides<sup>5-7</sup>. For these applications the material is required to have no impurities and be homogenous.

Preparation methods of  $\text{La}_2\text{Zr}_2\text{O}_7$  that have been used are; sol-gel method, combustion method, hydrothermal synthesis and coprecipitation method<sup>8-11</sup>. Mechanochemical synthesis is a preparation method that has been adopted for the synthesis of this material; this method uses high mechanical energy to disrupt the crystal structure of the starting materials thus leading to solid state amorphization<sup>12</sup>. Mechanical synthesis of the  $\text{La}_2\text{Zr}_2\text{O}_7$  has previously been done using a dry route; this had to be modified because of the disadvantages it encountered. Powder tends to agglomerate of the milling pot used and this in turn leads to decreased yields of the final product. Wet mechanochemical synthesis has now been used to prepare  $\text{La}_2\text{Zr}_2\text{O}_7$  because of the many advantages it has over dry mechanochemical synthesis and these are; higher yields, good homogeneity of the product, lower power requirement and higher rotational speeds to name a few<sup>13</sup>.

In this chapter  $\text{La}_2\text{Zr}_2\text{O}_7$  is synthesized using the wet mechanochemical method and for the first time this material is synthesized using a stainless steel pot.

#### 4.2 Experimental approach

##### 4.2.1 Materials

Powders of  $\text{La}_2\text{O}_3$  and  $\text{ZrO}_2$  and these were of analytical grade with high percentages of purity. Absolute ethanol was also used as the solvent during the synthesis of the material.

#### **4.2.2 Wet mechanochemical synthesis**

The synthetic route of  $\text{La}_2\text{Zr}_2\text{O}_7$  by wet mechanochemical synthesis was reported from Jarligo *et.al*<sup>14</sup>. Stoichiometric amounts of  $\text{La}_2\text{O}_3$  and  $\text{ZrO}_2$  were used and the mole ratio was 1:2. The starting materials were not pre-treated; they were used as they were because of their purity.  $\text{La}_2\text{O}_3$  with a mass of 2.717 g was used together with 2.055 g of  $\text{ZrO}_2$ . These starting materials were combined with absolute ethanol to form a suspension in a 50 mL stainless steel grinding pot with stainless steel balls. The ratio of the ball to powder was 10:1 by mass and this was done to increase the grinding of the powder for enhanced homogeneity. The size of the stainless steel balls used was 5 mm. The mixture was subjected to a planetary ball mill for 24 hours at a rotation speed of 400 rotations per minute (rpm) and the resulting slurry was dried at 110 °C for a further 24 hours. It was followed by heat treatment at 1200 °C for 1 hour.

#### **4.2.3 Characterization techniques**

The as-milled product before heat treatment was analysed using the PXRD (see Figure 4.1), so was the heat treated product (see Figure 4.2). This heat treated product was further analysed with variable temperature PXRD. The final product was further analysed using Rietveld refinement.

### 4.3 Results and discussion

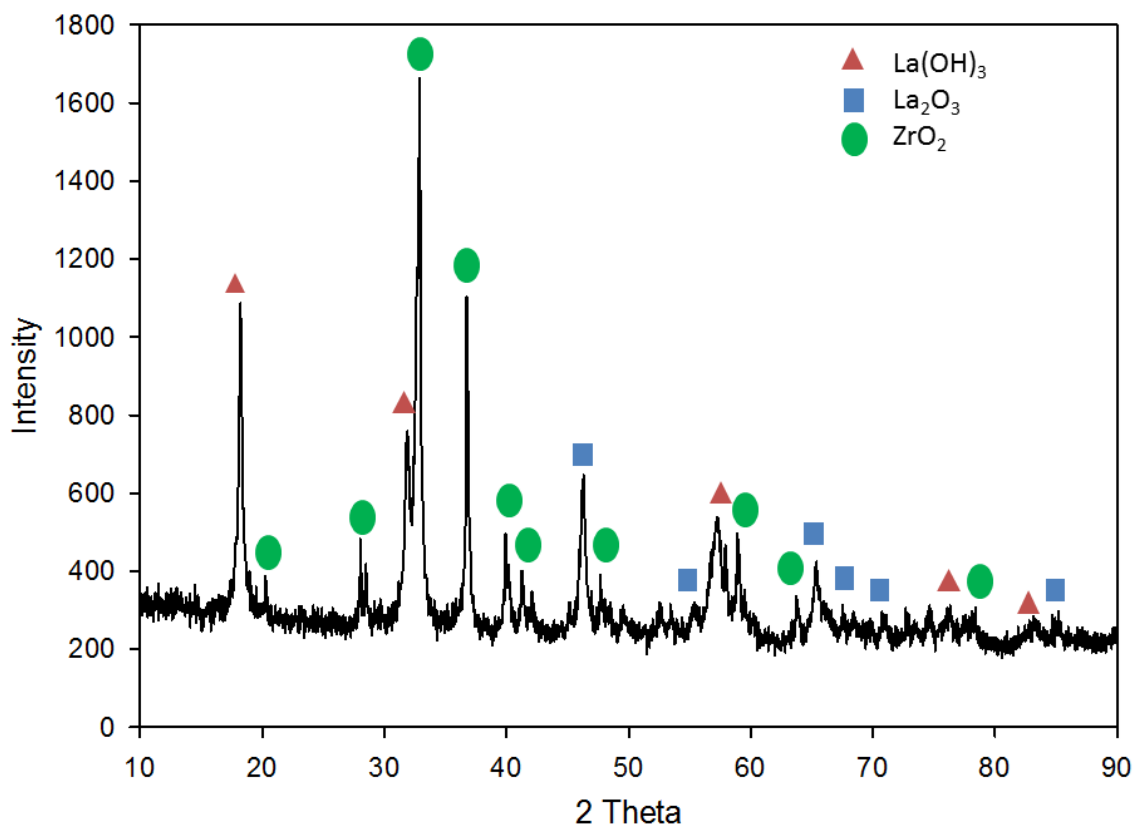


Figure 4.1 PXRD pattern of  $\text{La}_2\text{Zr}_2\text{O}_7$  as-milled before heat treatment,  $\lambda=1.78897 \text{ \AA}$ .

The PXRD pattern of the product before heat treatment is shown in Figure 4.1. The Figure shows that after the milling process a new phase,  $\text{La}(\text{OH})_3$ , formed from the starting materials and this is due to the hygroscopic behaviour of  $\text{La}_2\text{O}_3$ <sup>15</sup>. Figure 4.1 also indicates that the starting materials had amorphous structures seen at higher 2 theta values. The desired product,  $\text{La}_2\text{Zr}_2\text{O}_7$ , was not formed during the milling process hence it is not visible on the PXRD pattern. This thus shows the importance of heat treatment after a milling process.  $\text{La}_2\text{Zr}_2\text{O}_7$  was only formed after heat treatment as shown in Figure 4.2.

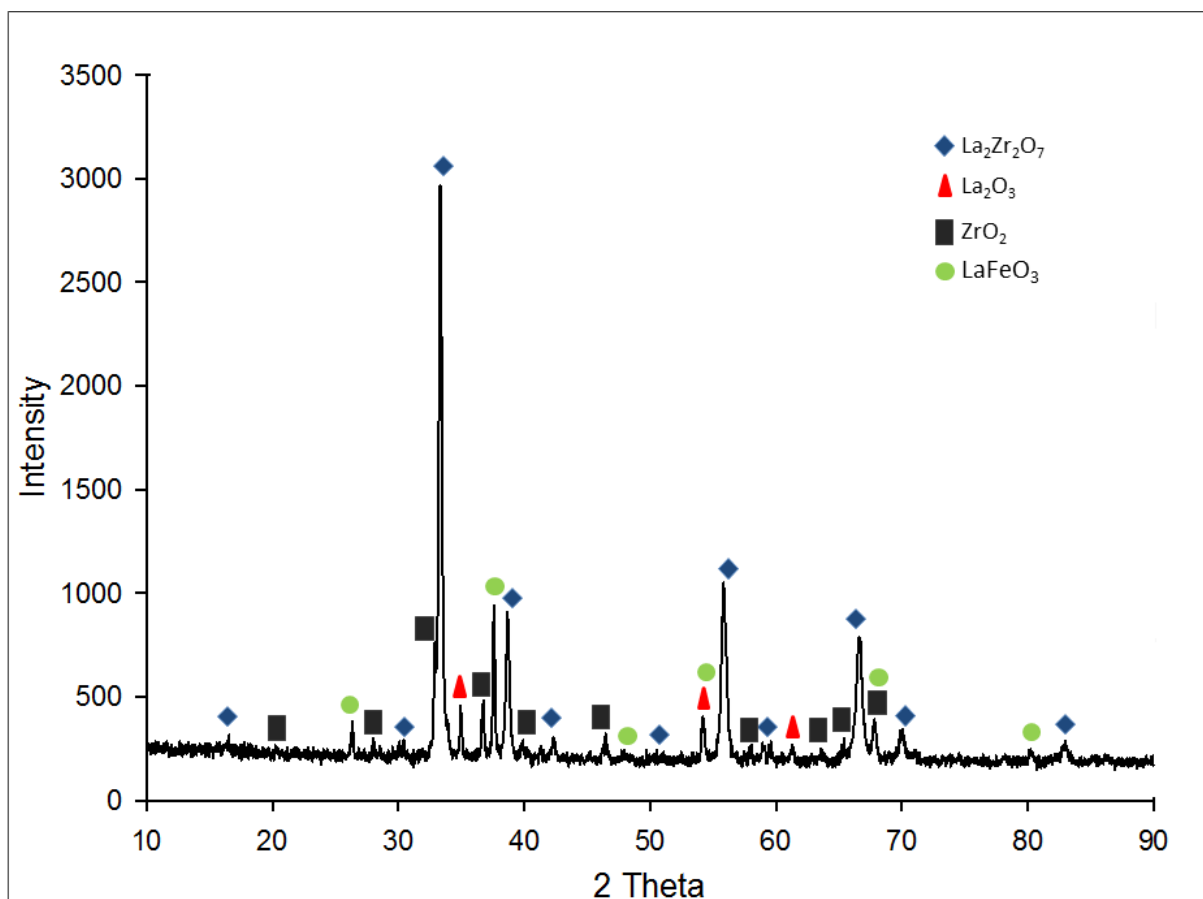


Figure 4.2: PXR D pattern of  $\text{La}_2\text{Zr}_2\text{O}_7$  after heat treatment at 1200 °C,  $\lambda=1.78897 \text{ \AA}$ .

Figure 4.2 shows the PXR D of  $\text{La}_2\text{Zr}_2\text{O}_7$  after it was heat treated, from the Figure above there are three phases of oxides that exist and these were identified using the PDF database. However, there is a phase of  $\text{La}_2\text{Zr}_2\text{O}_7$  as a pyrochlore and this is indicated by the superlattice peaks that exist and these are;  $2\theta \approx 18^\circ$  (111),  $31^\circ$  (311),  $42^\circ$  (331),  $51^\circ$  (333),  $59^\circ$  (531) and  $70^\circ$  (444). This implies that the  $\text{La}_2\text{Zr}_2\text{O}_7$  present has a pyrochlore structure type with Fd-3m as the space group. The presence of  $\text{La}_2\text{O}_3$ ,  $\text{ZrO}_2$  and  $\text{LaFeO}_3$  means that even though a phase of  $\text{La}_2\text{Zr}_2\text{O}_7$  was obtained there were still some impurities. The  $\text{La}_2\text{O}_3$  and  $\text{ZrO}_2$  are part of the reactants that didn't fully react and form the required product.  $\text{LaFeO}_3$  perovskite was formed by  $\text{La}_2\text{O}_3$  reacting with some of the iron (Fe) liberated from the stainless steel pot used in the planetary ball mill. A quantitative PXR D study of the product was done to calculate the percentage composition of the materials present and this is represented in the Figure 4.3.

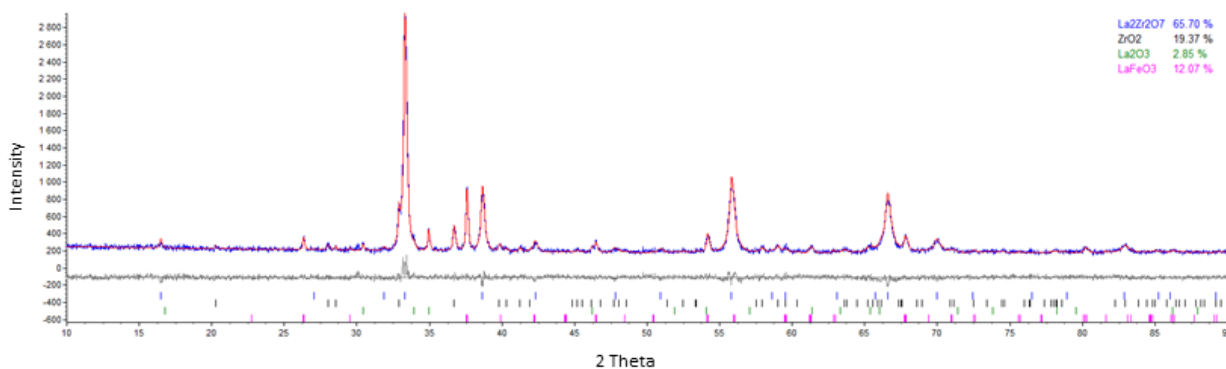


Figure 4.3 Rietveld refined profile plots of  $\text{La}_2\text{Zr}_2\text{O}_7$  with  $R_{\text{wp}} = 7.29\%$ , this was fitted with the impurities present.

Figure 4.3 shows a refinement fit for  $\text{La}_2\text{Zr}_2\text{O}_7$  and all the impurities present, this also shows the percentage compositions of all the materials present. According to the model the percentage composition of the material is as follows in a descending order;  $\text{La}_2\text{Zr}_2\text{O}_7$  65.70%,  $\text{ZrO}_2$  19.37%,  $\text{LaFeO}_3$  12.07% and  $\text{La}_2\text{O}_3$  2.85%. The phase of interest which was  $\text{La}_2\text{Zr}_2\text{O}_7$  was the most present. An interesting observation is that the amount of iron that was extracted from the stainless steel pot can be calculated using the percentage of  $\text{LaFeO}_3$  obtained from Rietveld refinement calculations. The total amount of the material synthesized was 5g and of this amount 12.07% was  $\text{LaFeO}_3$  which makes it 0.6035g. To calculate the total amount of elemental Fe present the molar mass of Fe (55.845 g/mol) was divided by the molar mass of  $\text{LaFeO}_3$  (242.751 g/mol) and multiplied by the mass of  $\text{LaFeO}_3$  (0.6035 g), which makes the mass of elemental Fe 0.1388 g. this implies that the total amount of Fe that was physically removed from the stainless steel pot was 0.1388 g. The implications of using a stainless steel pot when synthesizing pyrozoirconates using a planetary ball mill have never been reported in literature and this study shows that  $\text{ZrO}_2$  is a hard metal oxide capable of extracting softer metals from stainless steel.

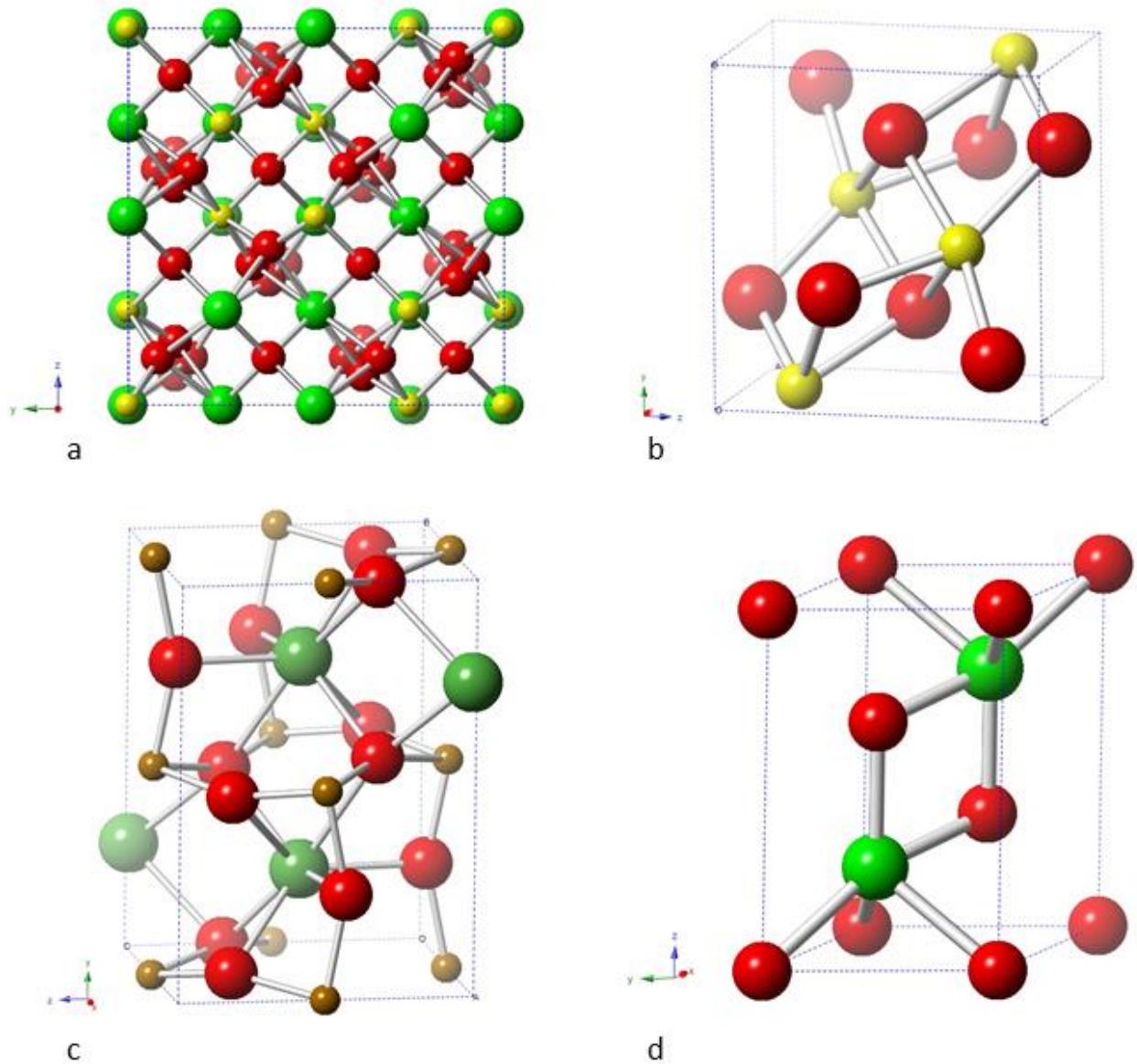
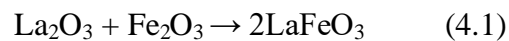


Figure 4.4: Graphic representations of the materials present in the final product. The structures in alphabetic order represent a)  $\text{La}_2\text{Zr}_2\text{O}_7$  with a pyrochlore structure type, b)  $\text{ZrO}_2$ , c)  $\text{LaFeO}_3$  and d)  $\text{La}_2\text{O}_3$ . Red spheres are O atoms, yellow represents Zr, green represents La and brown represents Fe.

From the Figure above, structure a shows a pyrochlore structure type and this satisfies the stability range of pyrochlores as determined by Minervini *et.al*<sup>16</sup>. The  $\text{La}^{3+}/\text{Zr}^{4+}$  ratio of  $\text{La}_2\text{Zr}_2\text{O}_7$  structure type is 1.61, suggesting that  $\text{La}_2\text{Zr}_2\text{O}_7$  is a pyrochlore material. Amongst the parameters used to determine whether a material is a pyrochlore there is also the 48f positional parameter, the refined value for  $\text{La}_2\text{Zr}_2\text{O}_7$  was determined and found to be 0.32364. This refined value suggests that the material synthesized was a disordered pyrochlore and this

is shown by the O atoms that form clusters at different sites as compared to the O atoms that are aligned at position 8b. This disorder implies that the  $\text{BO}_6$  octahedron that exists is distorted as compared to perfect octahedrons that exist towards the lower limit of the 48f x positional parameter ( $x=0.3125$ ). Even though there are impurities on the final product a pyrochlore structure type exists and it was the most dominant phase. The starting structure model used to refine  $\text{La}_2\text{Zr}_2\text{O}_7$  was that of pyrochlore structure type and it was in good agreement with the structure synthesized, this further confirms that the phase of  $\text{La}_2\text{Zr}_2\text{O}_7$  was a pyrochlore with a lattice parameter of  $10.810 \text{ \AA}$ .

Structure b and d are well known and these are the starting materials, whilst the most interesting phase was structure c which is  $\text{LaFeO}_3$ . The Fe present was coming from the stainless steel pot. There have been reports of synthesizing  $\text{LaFeO}_3$  by high energy ball milling starting with  $\text{La}_2\text{O}_3$  and  $\text{Fe}_2\text{O}_3$  as the reactants and this is according to the equation below <sup>15</sup>;



The structure of  $\text{LaFeO}_3$  as refined using Rietveld was found to be a perovskite type of structure. It was decided to study the thermoresponsive behaviour of the product to determine whether phase transformations would occur with increasing temperature; this is presented in Figure 4.5.

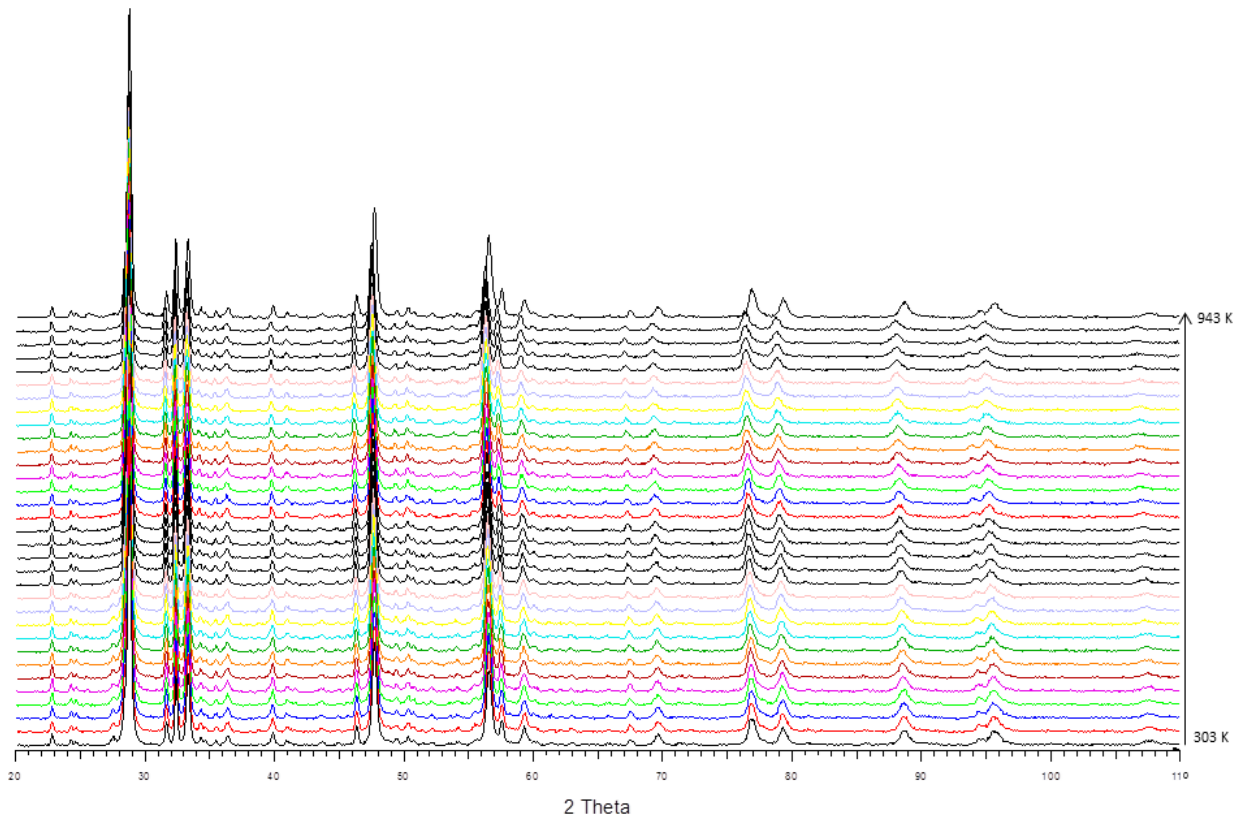


Figure 4.5 Variable temperature plots of  $\text{La}_2\text{Zr}_2\text{O}_7$  with traces of  $\text{ZrO}_2$ ,  $\text{LaFeO}_3$  and  $\text{La}_2\text{O}_3$  measured from 303 K to 943 K,  $\lambda=1.5406 \text{ \AA}$

The Figure above shows PXRD plots of the product from 303 K to 943 K, this was done to study the thermo-responsive behaviour of  $\text{La}_2\text{Zr}_2\text{O}_7$  in order to determine the thermal expansion coefficient. Figure 4.2 has shown that the material present was impure; as a result the thermal expansion coefficient is expected to be affected by the other phases present in the material. Peaks that represent  $\text{La}_2\text{O}_3$ ,  $\text{LaFeO}_3$ ,  $\text{La}_2\text{Zr}_2\text{O}_7$  and  $\text{ZrO}_2$  were zoomed in to indicate that there was peak shifting that occurred during the thermal treatment of the material and this is shown in Figure 4.6.

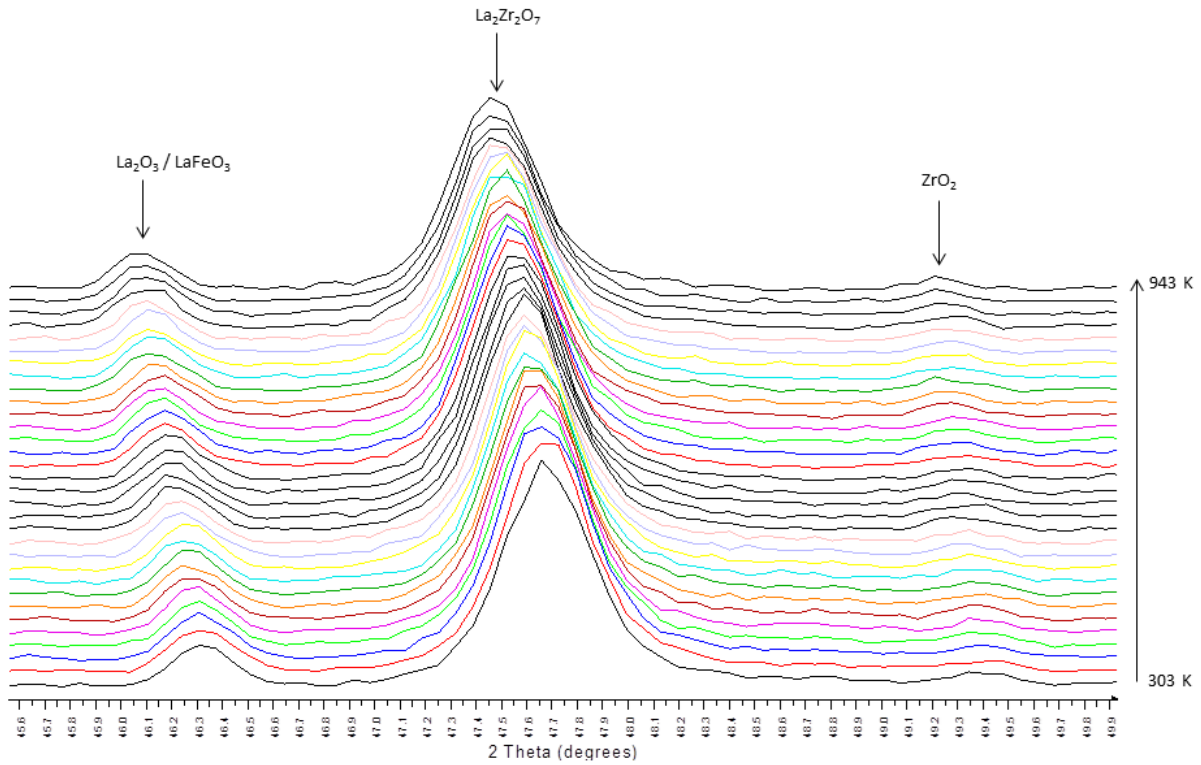


Figure 4.6 Zoomed in peaks of all the phases to show peak shifting during the heat treatment.

From Figure 4.6 the first peak shows  $\text{La}_2\text{O}_3$  and  $\text{LaFeO}_3$  in one position and this is due to the peaks overlapping, the  $\text{ZrO}_2$  peaks is not as intense as compared to the other peaks but was shown to indicate that all the phases had some form of peak shifting. All the peaks shifted towards the left and this implies that there was thermal expansion, this come from Bragg's law which is shown below;

$$n\lambda = 2d\sin\theta \quad (4.2)$$

According to Bragg's law the d spacing within a unit cell is inversely proportional to the position of the peak ( $2\theta$ ) which means that as the angle decreases the d spacing which represents the planes increases, thus expanding the unit cell. This suggests that all the phases present expanded with increasing temperature. The phase of interest however, which was  $\text{La}_2\text{Zr}_2\text{O}_7$ , was further studied to calculate the thermal expansion. A plot of lattice parameter against temperature was used to determine the thermal expansion of  $\text{La}_2\text{Zr}_2\text{O}_7$  and this is shown in Figure 4.7.

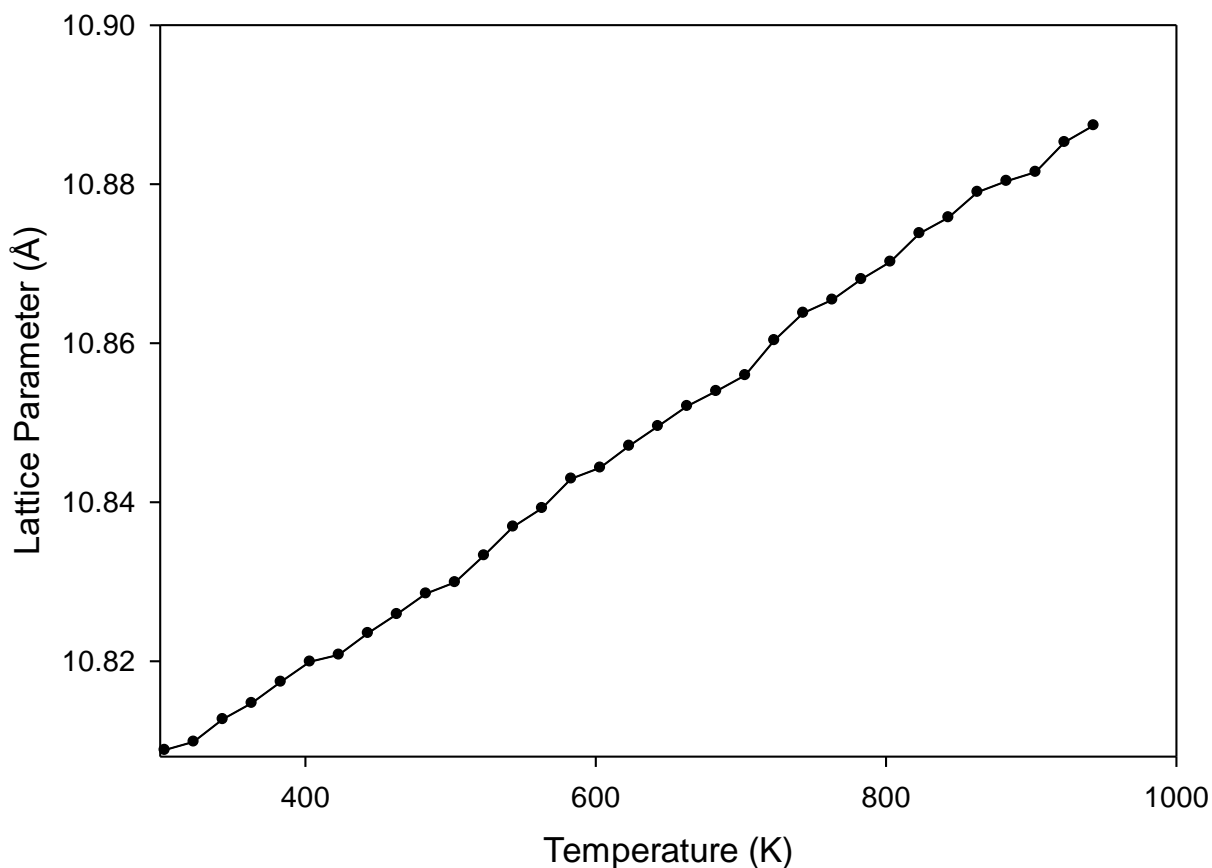


Figure 4.7 Lattice parameter obtained by Rietveld refinement against temperature plot for  $\text{La}_2\text{Zr}_2\text{O}_7$ .

The Figure above shows how the lattice parameter of  $\text{La}_2\text{Zr}_2\text{O}_7$  is affected by an increase in temperature; from the Figure it is evident that the lattice parameter has a linear relationship with temperature. The  $\text{La}_2\text{Zr}_2\text{O}_7$  pyrochlore structure has a cubic unit cell, thus implying that the expansion of the unit cell in this case is isotropic hence the thermal expansion coefficient was calculated as the linear thermal expansion. Equation 4.3 below was used to calculate the thermal expansion.

$$\alpha_a = \frac{1}{a_{303}} \left( \frac{\partial a}{\partial T} \right) \quad (4.3)$$

The lattice thermal expansion coefficient of  $\text{La}_2\text{Zr}_2\text{O}_7$  from 303 K to 943 K was found to be  $11.14 \times 10^{-6} \text{ K}^{-1}$ , which is an acceptable value when compared to literature values which range from  $7.5\text{-}10 \times 10^{-6} \text{ K}^{-1}$  <sup>17-19</sup>. The  $\text{La}_2\text{Zr}_2\text{O}_7$  synthesized had a pyrochlore type structure and in pyrochlore structure the thermal expansion coefficient increases with increasing

disorder. This high thermal expansion was therefore expected because of the increase in disorder which was observed in the material with an overall increase in the 48f positional parameter.

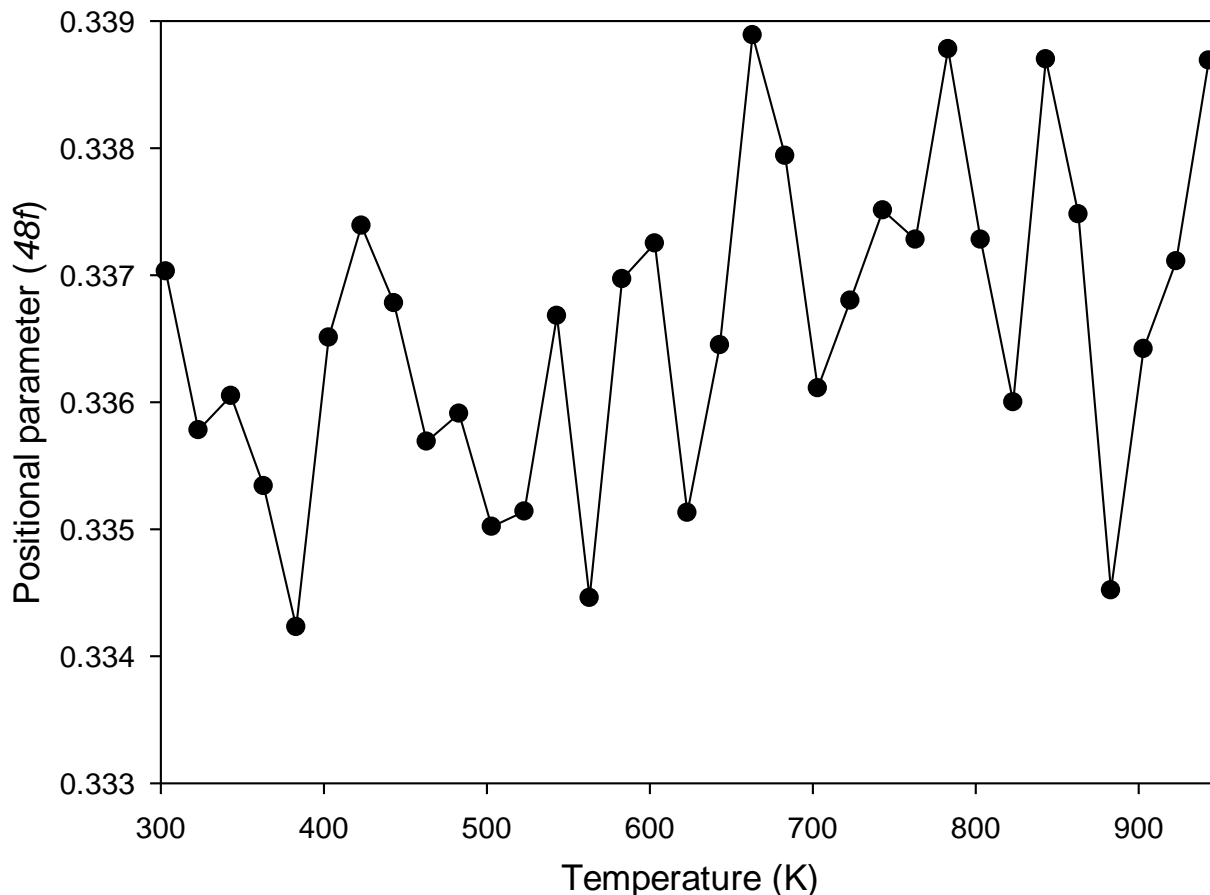


Figure 4.8 Variation of the 48f x positional parameter as a function of temperature for  $\text{La}_2\text{Zr}_2\text{O}_7$  determined by Rietveld refinement.

The Figure above shows differences in the positional parameter with an increase in temperature, from there is a progressive increase in the positional parameter with increasing temperature on average. The 48f x positional parameter of oxygen affects the stability of a pyrochlore material; this has effects on the B ( $\text{Zr}^{4+}$ ) site octahedron. When the positional parameter has a value of 0.3125 the  $\text{BO}_6$  octahedron is regular which means that there is order in a pyrochlore type structure, at 0.375 however the  $\text{BO}_6$  octahedron becomes distorted. The distortions arise due to the axial oxygen atoms shifting from their original positions, thus introducing disorder in a pyrochlore type structure. Bond distances between Zr and O atoms at the  $\text{ZrO}_6$  octahedron were calculated as a function 48f x positional parameter by computer

simulation; the trend observed was that as the positional parameter increases so does the bond distance between Zr and O. An observation made was that the bond distances for either the Zr-O on the equatorial position or the axial position were equal; this was an indication that even though there was axial distortions on the  $ZrO_6$  octahedron the length of the bonds elongated simultaneously. The bond distance as a function of the 48f x positional parameter is shown in the Figure below to clarify the trend observed.

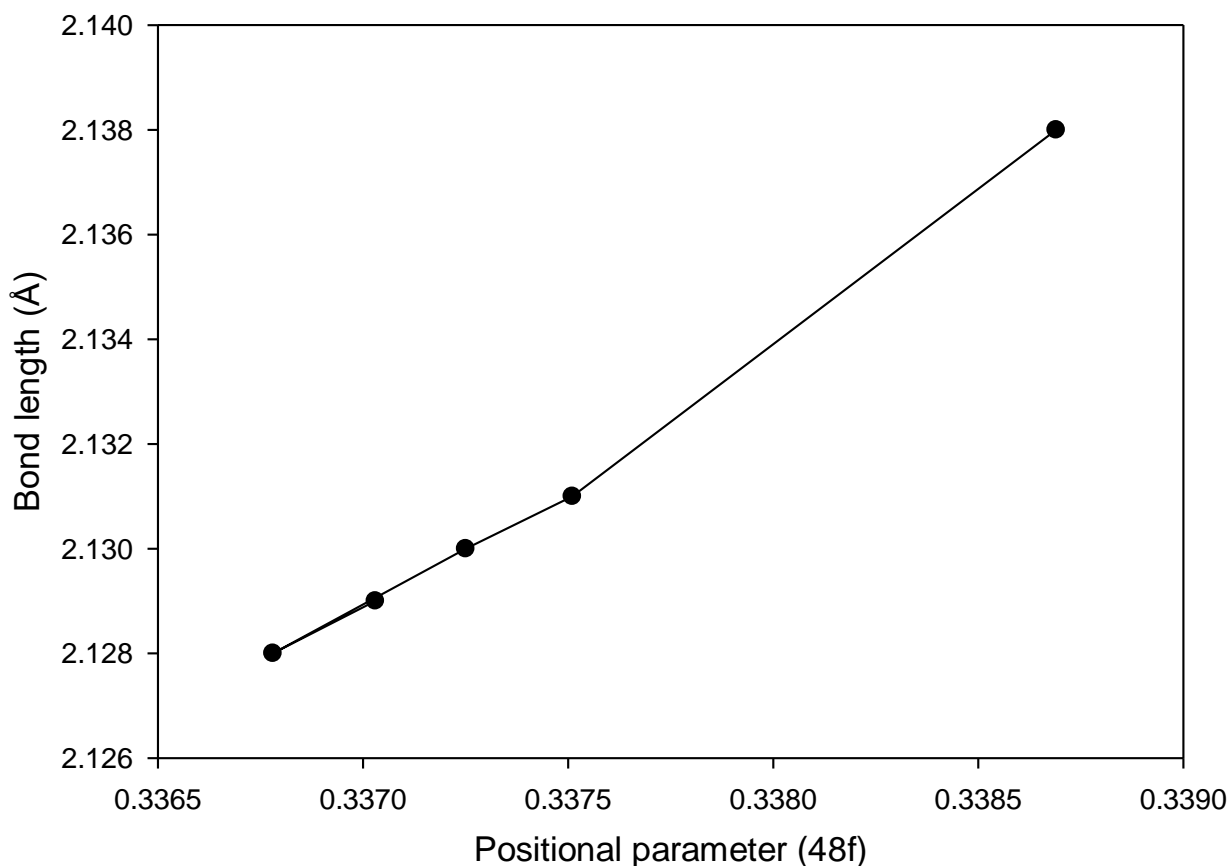


Figure 4.9 Bond lengths between Zr and O atoms as a function of the 48f x positional parameter determined by Rietveld refinement.

The lower limit of the positional parameter ( $x=0.3125$ ) gave a calculated value of  $2.026 \text{ \AA}$  as the bond distance between Zr and O while the upper limit ( $x=0.375$ ) gave a bond distance of  $2.339 \text{ \AA}$ . This clearly indicates that the bond distance is affected by changes in the positional parameter. The values used to plot Figure 4.9 are some of the values used to plot Figure 4.8. From Figure 4.9 there is evidence that the bond distance increases with increasing positional parameter, this increase in bond distance affects the lattice parameter of the material. An increase in bond distance indicates that the d spacing within a unit cell of a

material increases, thus increasing the lattice parameter which in turn increases the linear thermal expansion of a material.

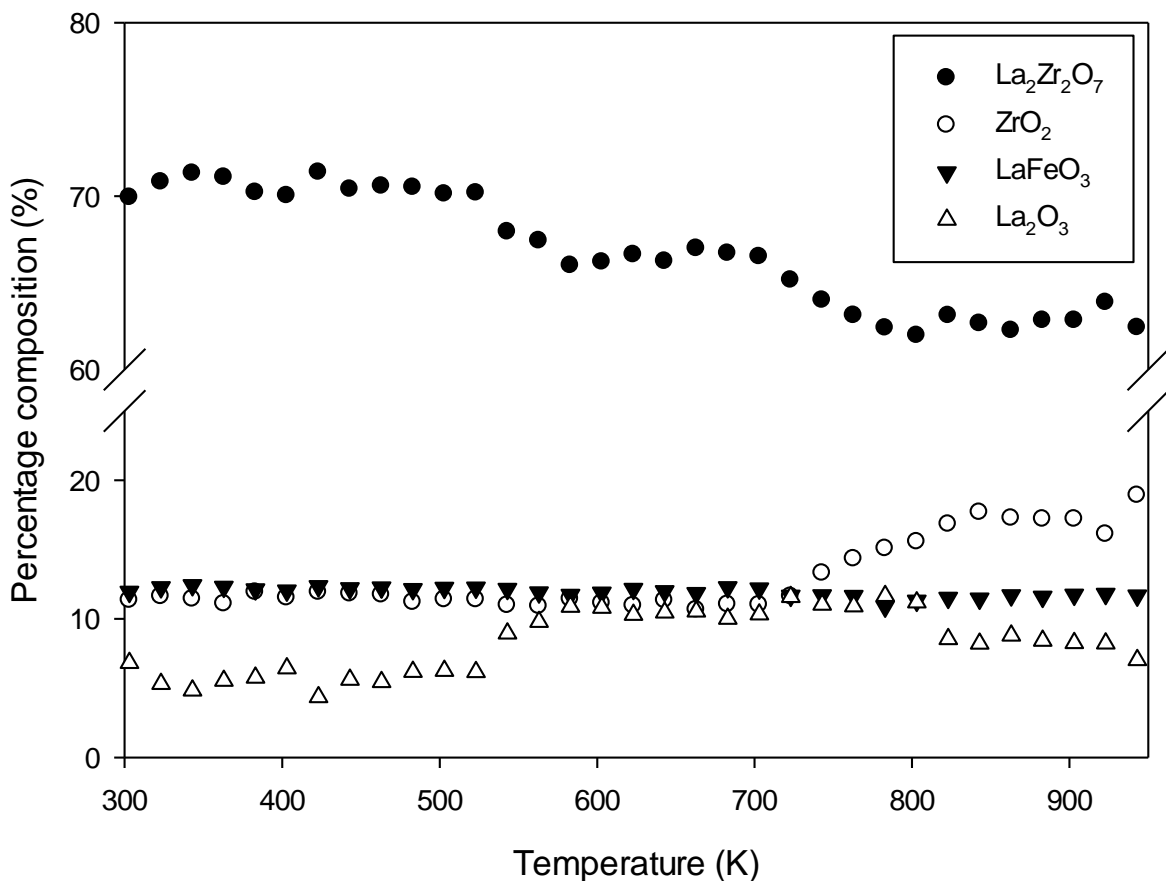


Figure 4.10 Percentage composition of each phase as a function of temperature

Figure 4.10 shows the percentage composition of each phase. This Figure was generated to study the effects of temperature to the percentage composition of each phase, according to this Figure La<sub>2</sub>Zr<sub>2</sub>O<sub>7</sub> was the most dominant phase while La<sub>2</sub>O<sub>3</sub> was the least present phase. It is worth noticing that the overall percentage composition of La<sub>2</sub>Zr<sub>2</sub>O<sub>7</sub> decreased as the temperature increased, this decreasing phase was however correlated with the increase in the overall percentages of La<sub>2</sub>O<sub>3</sub> and ZrO<sub>2</sub>. Decreasing amounts of La<sub>2</sub>Zr<sub>2</sub>O<sub>7</sub> is a clear indication that the phase is slowly separating into the precursors used to synthesize it. This result indicates that the La<sub>2</sub>Zr<sub>2</sub>O<sub>7</sub> phase is thermally unstable above approximately 500 K. The other observation from Figure 4.10 was the percentage of LaFeO<sub>3</sub>, this percentage was almost constant as the temperature increased.

## 4.4 Conclusions

A mechanochemical synthetic route was followed for synthesizing  $\text{La}_2\text{Zr}_2\text{O}_7$  using a stainless steel jar. A product was obtained and from PXRD analysis it was found that the product was impure. It is worth noting however that there were peaks that represented  $\text{La}_2\text{Zr}_2\text{O}_7$ . Amongst the impurities present in the final product were  $\text{La}_2\text{O}_3$  and  $\text{ZrO}_2$  as unreacted starting materials. The other interesting impurity present was  $\text{LaFeO}_3$ , a perovskite type structure. The reason this material formed part of the product was due to the Fe that was part of the stainless steel jar. This material reacted with  $\text{La}_2\text{O}_3$  to form the perovskite. From the results obtained a quantitative study was conducted to determine how much of the elemental Fe was extracted from the jar and this was found to be 0.1388 g. High temperature PXRD formed part of the study to determine the TEC of  $\text{La}_2\text{Zr}_2\text{O}_7$  and investigate how the impurities affect this coefficient, the TEC was found to be  $11.14 \times 10^{-6} \text{ K}^{-1}$ , this value was higher than that of a pure phase of  $\text{La}_2\text{Zr}_2\text{O}_7$  and this is expected due to the disorder that is introduced by the impurities.

## 4.5 References

1. Ohara M., Takahashi K., Torigoe T. and Yamaguchi K., *Proceedings of the International Gas Turbine Congress*, (Kobe, Japan, November 1999) pp. 821–824.
2. Vassen R., Cao X., Tietz F., Basu D., Stover D., *J. Am. Ceram. Soc.*, 83 (2000) 2023.
3. Cao X. Q., Vassen R. and Stoeber D.: *J. European Ceram. Soc.* 24 (2004) 1–10.
4. Zhang A., Lu M., Yang Z., Zhou G. and Zhou Y., *Solid State Science*, 10 (2008) 74–81.
5. Modeshia D. R. and Walton R. I., *Chem. Soc. Rev.*, 2010, 39, 11, 4303–25 .
6. Subramanian M. A., Aravamuda G., and Subba Rao G. V., *Progress in solid state chemistry*, 1983, 15(2), 55-143.
7. Ewing R. C., Weber W. J., and Lian J., *Journal of Applied Physics*, 2004, 95, 5949 .
8. Cloet V., Lommens P., Huhne R., De Buysser K., Hoste S., and Van Driessche I., *J. Cryst. Growth*, 2011, 325, 1, 68–75.
9. Orlovskaya N., Chen Y., Miller N., Abernathy H., Haynes D., Tucker D., and Gemmen R., *Adv. Appl. Ceram.*, 2011, 110, 1, 54–7.
10. Chen D., and Xu R., *Mater. Res. Bull.*, 1998, 33, 3, 409–17.
11. Chen H., Gao Y., Liu Y., and Luo H., *J. Alloys Compd.*, 2009, 480, 2, 843–8.

12. Kong L. B., Zhang T. S., Ma J., and Boey F., *Progress in Materials Science*, 2008, 53, 207-322.
13. Richerson D. W., *Modern Ceramic Engineering: Properties, Processing and Use in Design*, (M. Dekker, New York, 1992) pp. 386–391.
14. Jarligo M. O. D., Kang Y-S., Kawasaki A., Watanabe R., *Materials Transactions*, 2004, 45, 8, 2634-2637.
15. Sorescu M., Xu T., and Hannan A., *American Journal of Materials Science*, 2011, 1, 1, 57-66.
16. Minervini L, and Grimes R. W., *Journal of the American Ceramic Society*, 2000, 83, 1873.
17. Kutty K. V. G., Rajagopalan S., Mathews C. K. and Varadaraju U. V., *Materials Research Bulletin*, 1994, 29, 7, 759-766.
18. Ushakov S. V., Navrotsky A., Weber R. J. K., and Neuefeind J. C., *J. Am. Ceram. Soc.*, 2015, 98 , 10, 3381–3388.
19. Lehmann H., Pitzer D., Pracht G., Vassen R., and Stover D., *J. Am. Ceram. Soc.*, 2003, 86, 8, 1338–44.

## Chapter 5

### Effects of annealing temperature in LaSmZr<sub>2</sub>O<sub>7</sub>, LaYZr<sub>2</sub>O<sub>7</sub> and SmYZr<sub>2</sub>O<sub>7</sub> doped pyrochlores

#### 5.1 Introduction

Pyrochlores of the structure type A<sub>2</sub>Zr<sub>2</sub>O<sub>7</sub> have been extensively studied over the years as they show potential in various applications, one of which is electrolytes in solid oxide fuel cells<sup>1</sup>. These materials possess a cubic pyrochlore structure and have a lattice parameter that is about 10 Å, some of the materials would have the pyrochlore stoichiometry (A<sub>2</sub>Zr<sub>2</sub>O<sub>7</sub>) but possess a defect fluorite structure type which has a lattice parameter of about 5 Å<sup>2</sup>. The structure preference of these materials depends on the cationic radius ratio between the A<sup>3+</sup> and the Zr<sup>4+</sup> ions respectively as determined by Minervini *et.al*<sup>3</sup>.

Pyrochlore type materials are interesting in that substitutions are possible in the A and the B site; the substitutions however are allowed only when the charge neutrality and the ionic radius ratios are suitable<sup>1</sup>. When these conditions are met the materials will have either stable cubic pyrochlore structures or defect fluorite type structures. Substitution at the A site could be done by alkali metals, alkali earth metals, transition metals and rare earth metals<sup>1</sup>.

In this chapter A<sub>2</sub>Zr<sub>2</sub>O<sub>7</sub> pyrochlore materials substituted on the A (where A=La, Sm, Y) site are synthesized and characterized using PXRD, Rietveld refinement and EPMA. The substituted materials are in the form (A, A')Zr<sub>2</sub>O<sub>7</sub>.

#### 5.2 Experimental approach

##### 5.2.1 Materials used

The precursors used were of analytical grade and were purchased at Sigma-Aldrich. These were La(NO<sub>3</sub>)<sub>3</sub>.6H<sub>2</sub>O (99%), Sm(NO<sub>3</sub>)<sub>3</sub>.6H<sub>2</sub>O (99.9%) and Y(NO<sub>3</sub>)<sub>3</sub>.6H<sub>2</sub>O (99.8%). The metals in the nitrate salts were used as the source of the A<sup>3+</sup> cation in the A<sub>2</sub>B<sub>2</sub>O<sub>7</sub> pyrochlore type structures. The source of the B<sup>4+</sup> cation was Zr in the form of a propoxide which was Zr(OC<sub>3</sub>H<sub>7</sub>)<sub>4</sub> (70%). There was no pretreatment of the precursors before synthesis.

### 5.2.2 Sol-gel synthesis of the doped analogues

A total of three materials were synthesized using the same method which was sol-gel synthesis and these were; (a)  $\text{LaSmZr}_2\text{O}_7$ , (b)  $\text{LaYZr}_2\text{O}_7$  and (c)  $\text{SmYZr}_2\text{O}_7$ . The total mass of each material synthesized was 1g.

d)  $\text{LaSmZr}_2\text{O}_7$

Equimolar amounts of  $\text{La}(\text{NO}_3)_3 \cdot 6\text{H}_2\text{O}$  (0.749 g, 1.713 mmol) and  $\text{Sm}(\text{NO}_3)_3 \cdot 6\text{H}_2\text{O}$  (0.762 g, 1.713 mmol) were dissolved separately in 10 ml isopropanol followed by mixing the solutions in a beaker. In a different beaker  $\text{Zr}(\text{OC}_3\text{H}_7)_4$  (1.603 g, 3.426 mmol) was dissolved in 10 ml isopropanol. The solution of the salts was then gradually poured in the isopropoxide solution stirred to give a homogenous mixture.

e)  $\text{LaYZr}_2\text{O}_7$

For this solid solution equimolar amounts of  $\text{La}(\text{NO}_3)_3 \cdot 6\text{H}_2\text{O}$  (0.837 g, 1.915 mmol) and  $\text{Y}(\text{NO}_3)_3 \cdot 6\text{H}_2\text{O}$  (0.735 g, 1.915 mmol) were dissolved separately in 10 ml isopropanol as solution a). This followed by dissolving  $\text{Zr}(\text{OC}_3\text{H}_7)_4$  (1.792 g, 3.83 mmol) in 10 ml isopropanol and the steps performed for  $\text{LaSmZr}_2\text{O}_7$  were followed

f)  $\text{SmYZr}_2\text{O}_7$

The synthetic route used for the above materials was followed for the synthesis of this material. The amounts used were as follows;  $\text{Sm}(\text{NO}_3)_3 \cdot 6\text{H}_2\text{O}$  (0.834 g, 1.874 mmol),  $\text{Y}(\text{NO}_3)_3 \cdot 6\text{H}_2\text{O}$  (0.719 g, 1.874 mmol) and  $\text{Zr}(\text{OC}_3\text{H}_7)_4$  (1.754 g, 3.748 mmol).

The resulting product from the materials was a gelatinous substance that was allowed to dry at room temperature for 24 hours. This was then ground and fired at 900 °C for 8 hours.

### 5.2.3 Characterization techniques

The Bruker D2 phaser was used for PXRD analysis at room temperature for all the products, this was to identify the phases present and was performed from  $2\theta = 10^\circ$  to  $90^\circ$ . Subsequent to PXRD, the electron probe micro analyzer (EPMA) was used to map different ions within the crystals and this was done to identify whether there was an even mixture of the ions within the crystals or if the ions present were localized at specific sites. EPMA was also a useful tool in determining whether the products had impurities. The products were annealed at 1200 °C for better crystallinity and further analyzed using PXRD. Subsequently, the

thermoreponsive behavior of the products was analyzed using variable temperature PXRD from 303 K to 1053 K.

## 5.3 Results and discussion

### 5.3.1 Powder X-ray diffraction studies

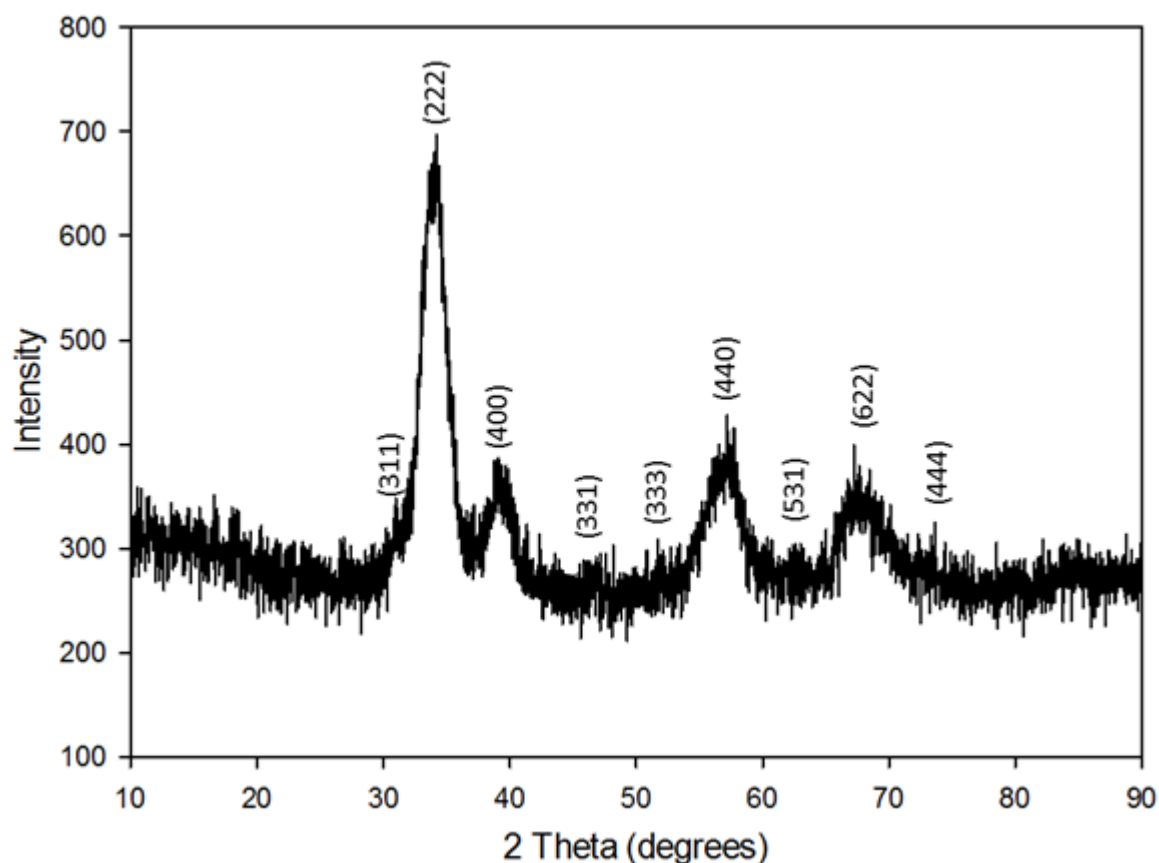


Figure 5.1 PXRD pattern of LaSmZr<sub>2</sub>O<sub>7</sub> after calcining at 900 °C.

The PXRD analysis of LaSmZr<sub>2</sub>O<sub>7</sub> (Figure 5.1) suggests that the material synthesized was a classical pyrochlore; this is indicated by the superlattice peaks exist with the following planes; (331), (311), (511) and (531) respectively. The only superlattice peak that was not clear was the one at (111). This is in good agreement with a study done by Lui *et.al* where they investigated Sm<sub>2-x</sub>La<sub>x</sub>Zr<sub>2</sub>O<sub>7</sub> with different compositions of x ranging from 0 to 1.0<sup>4</sup>. The different compositions lead to the same pyrochlore type structure. Further calculations were performed to confirm if the material was indeed a pyrochlore or a defect fluorite using Minervini's cationic ratio approximations which suggest that classical pyrochlores have a cation ration (A<sup>3+</sup>/B<sup>4+</sup>) that ranges from 1.46 to 1.78<sup>3</sup>. The calculated ratio of (La<sup>3+</sup>,

$\text{Sm}^{3+}/\text{Zr}^{4+}$  was found to be 1.56 which lies within the stability field of classical pyrochlores. This was followed by Rietveld refinement to determine the lattice parameter and 48fx positional parameter of the oxide ions. The Table that follows shows the Wyckoff positions of the ions with their respective fractional coordinates, the values obtained are from Rietveld refinement. The structural model in Table 5.1 was subsequently used to draw a structure of  $\text{LaSmZr}_2\text{O}_7$  and this is shown in Figure 5.2.

Table 5.1 Structural model of  $\text{LaSmZr}_2\text{O}_7$  pyrochlore type

Site	Wyckoff position	x	y	z
La	16d	0.500	0.500	0.500
Sm	16d	0.500	0.500	0.500
Zr	16c	0.000	0.000	0.000
O	48f	0.342	0.125	0.125
O'	8b	0.375	0.375	0.375

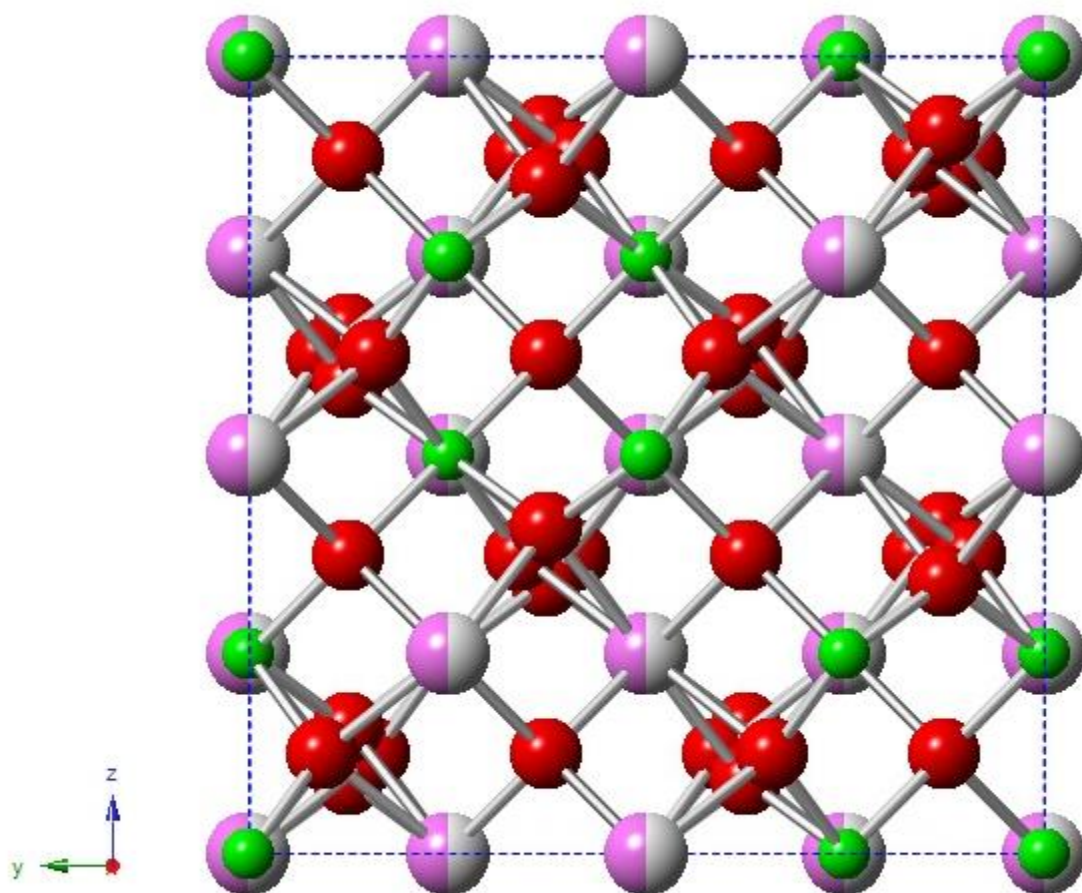


Figure 5.2 Structure of  $\text{LaSmZr}_2\text{O}_7$  viewed along the a-axis. Sm (pink), La (white), Zr (green) and O (red)

The material was synthesized such that the ratio of La:Sm was 1:1, and this in Figure 5.2 is shown by the two toned sphere with a pink and a white color suggesting that La and Sm share a position, this model was confirmed by Rietveld refinement. The parameters of interest in this structure were the lattice parameter and the 48f x positional parameter, the lattice parameter was  $10.67 \text{ \AA}$  and the positional parameter for the oxide ion at position 48f was 0.342 as shown in Table 5.1. A lattice parameter that is approximately  $10 \text{ \AA}$  is a distinct feature for classical pyrochlores, further confirming that the material had a pyrochlore type structure. The positional parameter of the oxide anion which was found to be 0.342 implies that the  $\text{ZrO}_6$  octahedron was distorted; this results from the oxide anions at position 48f exhibiting disorder.

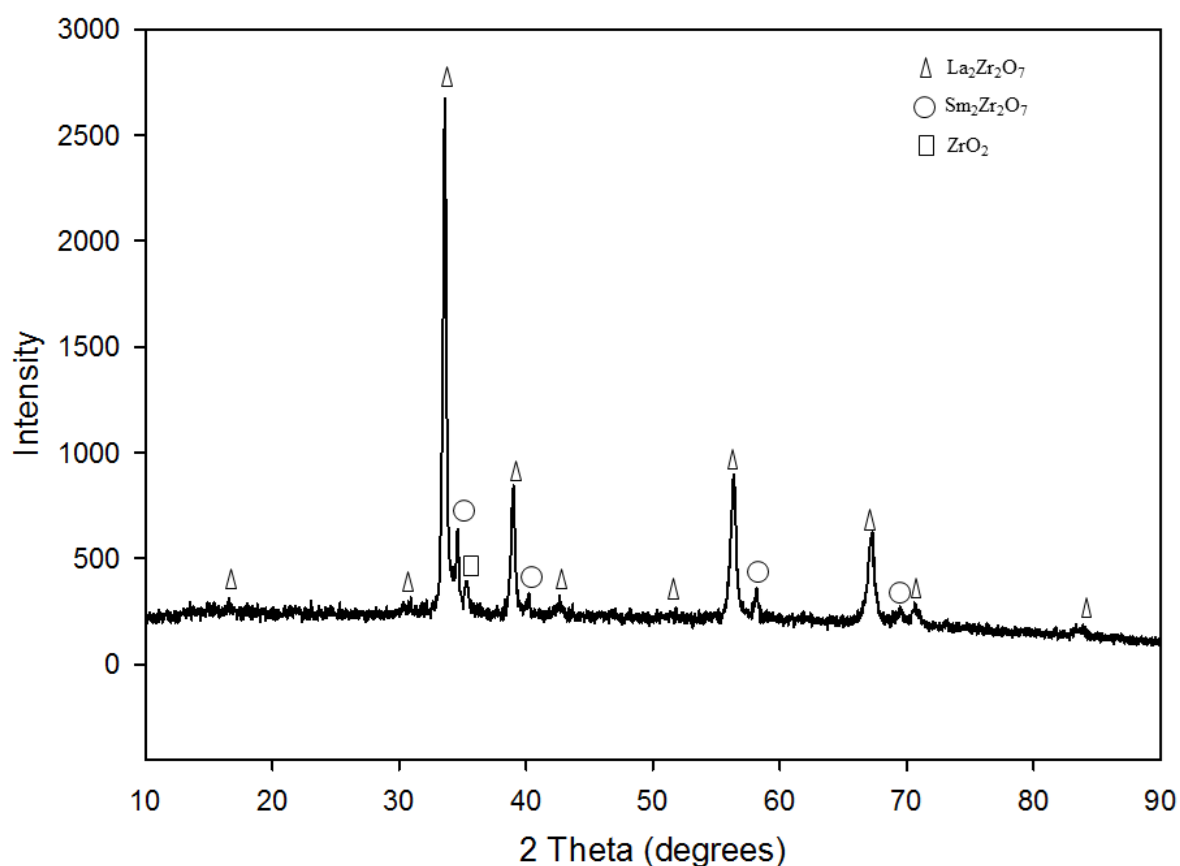


Figure 5.3 PXRD pattern of  $\text{LaSmZr}_2\text{O}_7$  after annealing at  $1200\text{ }^\circ\text{C}$

PXRD analysis of  $\text{LaSmZr}_2\text{O}_7$  after annealing at  $1200\text{ }^\circ\text{C}$  (Figure 5.3) shows that as the temperature increased there was significant crystallinity of the material, however, the material was not a single pure phase of  $\text{LaSmZr}_2\text{O}_7$  but a mixture of the primary pyrochlores ( $\text{La}_2\text{Zr}_2\text{O}_7$  and  $\text{Sm}_2\text{Zr}_2\text{O}_7$ ) and  $\text{ZrO}_2$ . This was confirmed using Rietveld refinement which resulted in a quantitative study showing the percentage contribution of each phase to the final product. From Figure 5.3 it was evident that  $\text{La}_2\text{Zr}_2\text{O}_7$  was the most dominant phase while

$\text{Sm}_2\text{Zr}_2\text{O}_7$  and  $\text{ZrO}_2$  were the least dominant of the three phases.

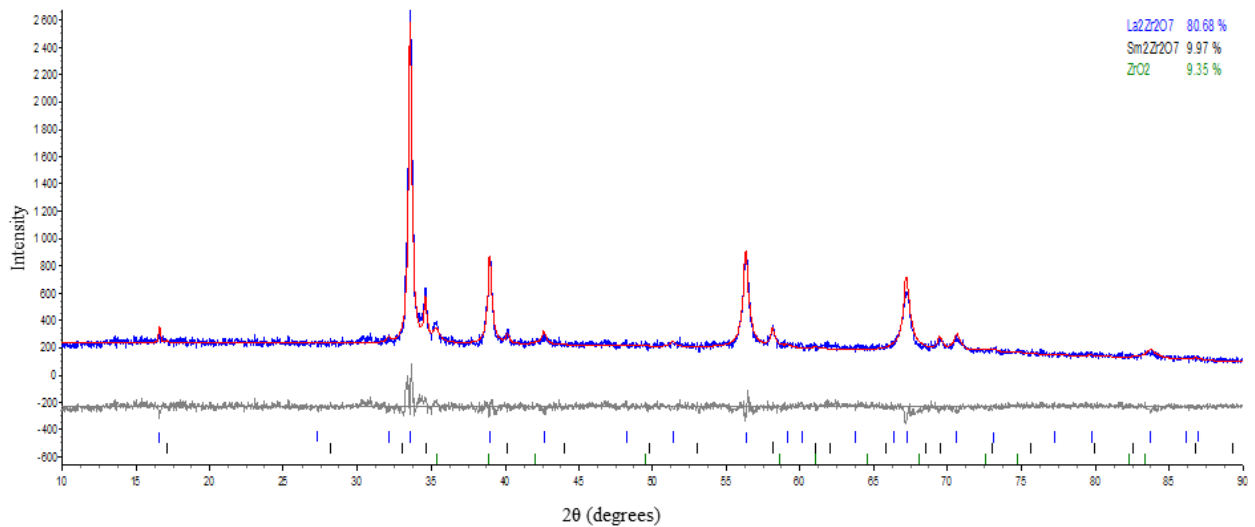


Figure 5.4 Rietveld refinement profile of  $\text{LaSmZr}_2\text{O}_7$  annealed at  $1200\text{ }^\circ\text{C}$ ,  $R_{wp}=8.156\%$

$\text{La}_2\text{Zr}_2\text{O}_7$  as the most dominant phase contributed 80.68% to the final product; the second was  $\text{Sm}_2\text{Zr}_2\text{O}_7$  which contributed 9.97% while  $\text{ZrO}_2$  was 9.35%. This was an indication that  $\text{LaSmZr}_2\text{O}_7$  is thermally unstable at  $1200\text{ }^\circ\text{C}$ , which indicates that this material is not viable for high temperature applications. A literature survey was done to find out if  $\text{LaSmZr}_2\text{O}_7$  has been extensively studied for high temperature applications and in the studies found it was indicated that the material has never been annealed at such a high temperature. A more comprehensive study has to be done to investigate the temperature at which this material disintegrates into the phases that were found. Although PXRD is a useful study in identifying different phases that exist in a material it is difficult to distinguish if the patterns that emerge are a result of a single phase or multiple phases overlapping in a peak, such a milestone requires advanced instrumentation such as synchrotron measurements.

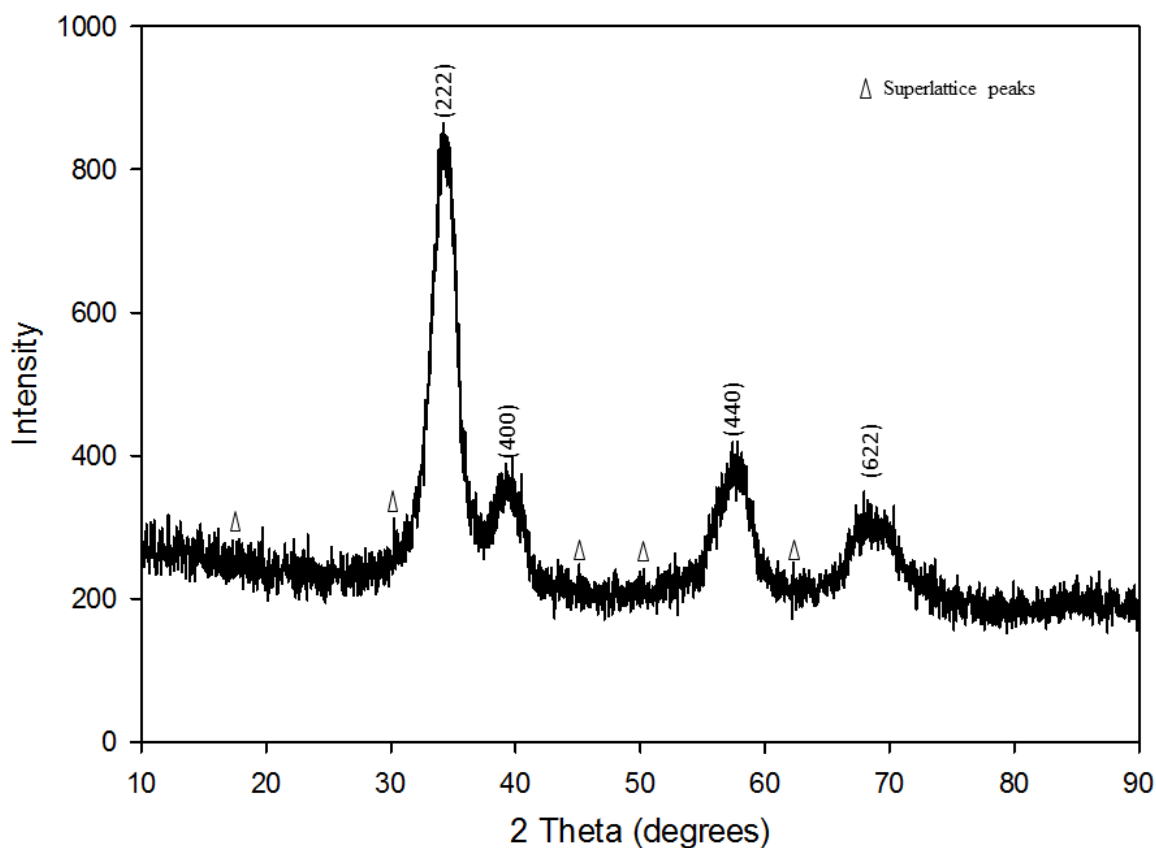


Figure 5.5 PXR D pattern of  $\text{LaYZr}_2\text{O}_7$  calcined at  $900\text{ }^\circ\text{C}$ .

The PXR D pattern of  $\text{LaYZr}_2\text{O}_7$  (Figure 5.5) which was calcined at  $900\text{ }^\circ\text{C}$  for 8 hours shows minor superlattice peaks, highlighted by triangles, which suggests that the material was a classic pyrochlore structure. This is in good agreement with a study conducted by Whittle *et.al* which was investigating various compositions of  $\text{La}_x\text{Y}_{2-x}\text{Zr}_2\text{O}_7$  ( $x = 0.0, 0.4, 0.8, 1.2, 1.6$  and  $2.0$ )<sup>5</sup>. From the variations the discovery was that a defect fluorite structure exists only when  $x \geq 1.2$ , below that value the material was predominantly a single pyrochlore phase with a minor defect fluorite phase. The material synthesized in this study had a 1:1 ratio of La to Y, suggesting that it has a predominant pyrochlore phase and Figure 5.5 shows this clearly. The A:B ratio which determines the stability field of pyrochlores done by Minervini *et.al* was found to be 1.51 and this falls within the stability field of pyrochlores, thus further confirming that the material was a pyrochlore type structure. Rietveld refinement was done for this material and the calculations were done using a pyrochlore phase, this resulted in a good match. The parameters from Rietveld refinement were used to model the structure of  $\text{LaYZr}_2\text{O}_7$ ; the structural model is shown in Table 5.2.

Table 5.2 Structural model for  $\text{LaYZr}_2\text{O}_7$  as a pyrochlore structure type

Site	Wyckoff position	x	y	z
La	16d	0.500	0.500	0.500
Y	16d	0.500	0.500	0.500
Zr	16c	0.000	0.000	0.000
O	48f	0.341	0.125	0.125
O'	8b	0.375	0.375	0.375

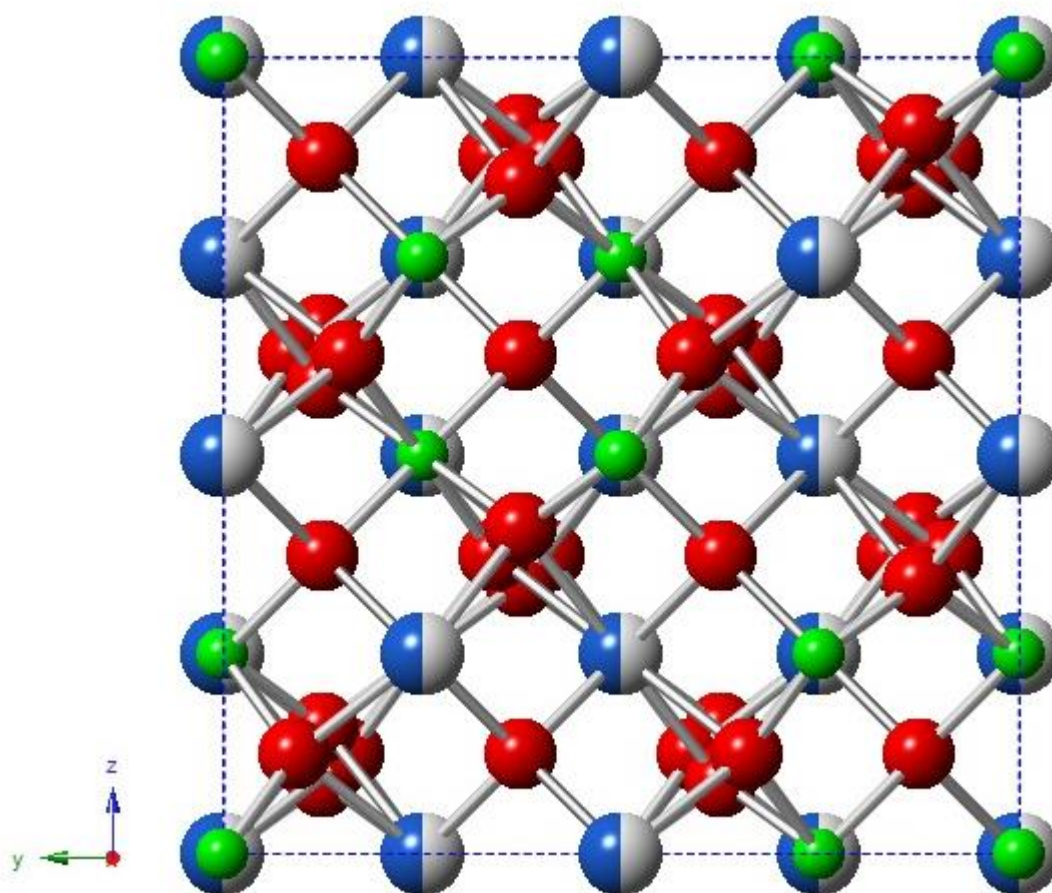


Figure 5.6 Structural model of  $\text{LaYZr}_2\text{O}_7$  as viewed from the (100) face. La (white), Y (blue), Zr (green) and O (red)

Table 5.2 shows the structural model used to draw the structure of  $\text{LaYZr}_2\text{O}_7$ . La and Y share a Wyckoff position (16d); this is indicated by the matching fractional coordinates. The percentage sharing of the position 50% for each of the  $\text{A}^{3+}$  cations ( $\text{La}^{3+}$  and  $\text{Y}^{3+}$ ), this is

shown in the graphic picture in Figure 5.5 where there is a spheres that are two toned. From the Figure it is evident that the cations are ordered while there is a noticeable disorder with some of the oxide anions. The disorder seen from the Figure results from the 48f positional parameter of the oxide anions, the value is shown in Table 5.2 as 0.341. As it was mentioned earlier, there are only two parameters in pyrochlore type structures that are refined and that is; the lattice parameter and the 48f positional parameter. As the positional parameter of pyrochlore structures approaches  $x = 0.3125$  the oxide anions at 48f become disordered, suggesting that the  $ZrO_6$  octahedron that exists within the structure is distorted. As the value approaches  $x = 0.375$  however, the octahedron becomes perfect due to the oxide anions exhibiting a higher degree of order. Therefore the 48f positional parameter that was obtained from Rietveld refinement ( $x = 0.341$ ) is between the limit for pyrochlore type structures, thus showing the disorder observed in Figure 5.6. The lattice parameter that was refined was found to be  $10.565 \text{ \AA}$ , which is an acceptable value for classic pyrochlores seeing that the value is twice that of defect fluorites ( $a \approx 5 \text{ \AA}$ ).

$LaYZr_2O_7$  was further annealed at  $1200 \text{ }^\circ\text{C}$  to increase the crystallinity and give sharp peaks, the PXRD pattern is shown in Figure 5.7. With increased temperatures used for annealing the material disintegrated from being a solid solution of  $LaYZr_2O_7$  to a mixture of two mixed metal oxides. The most dominant of the two present phases was  $La_2Zr_2O_7$  which was a pyrochlore type material; this is indicated by the superlattice peaks shown by the blue triangles while the least dominant was  $Y_2Zr_2O_7$  which was a defect fluorite. The results are sensible when compared to Figure 5.5 which shows a single phase of  $LaYZr_2O_7$  as a pyrochlore type structure, this indicates that the initial product which was which was only calcined at  $900 \text{ }^\circ\text{C}$  had more of  $La_2Zr_2O_7$  than  $Y_2Zr_2O_7$  which resulted in the presence of superlattice peaks. The pattern shown in Figure 5.7 was refined using Rietveld and matching using  $La_2Zr_2O_7$  as a pyrochlore and  $Y_2Zr_2O_7$  as a defect fluorite resulted in a good match. The Rietveld refinement profile of  $LaYZr_2O_7$ , as shown in Figure 5.8, also shows the percentage composition of each phase. From Figure 5.8 the percentage composition of  $La_2Zr_2O_7$  was calculated as 62.67 % and that of  $Y_2Zr_2O_7$  was 37.33 %.

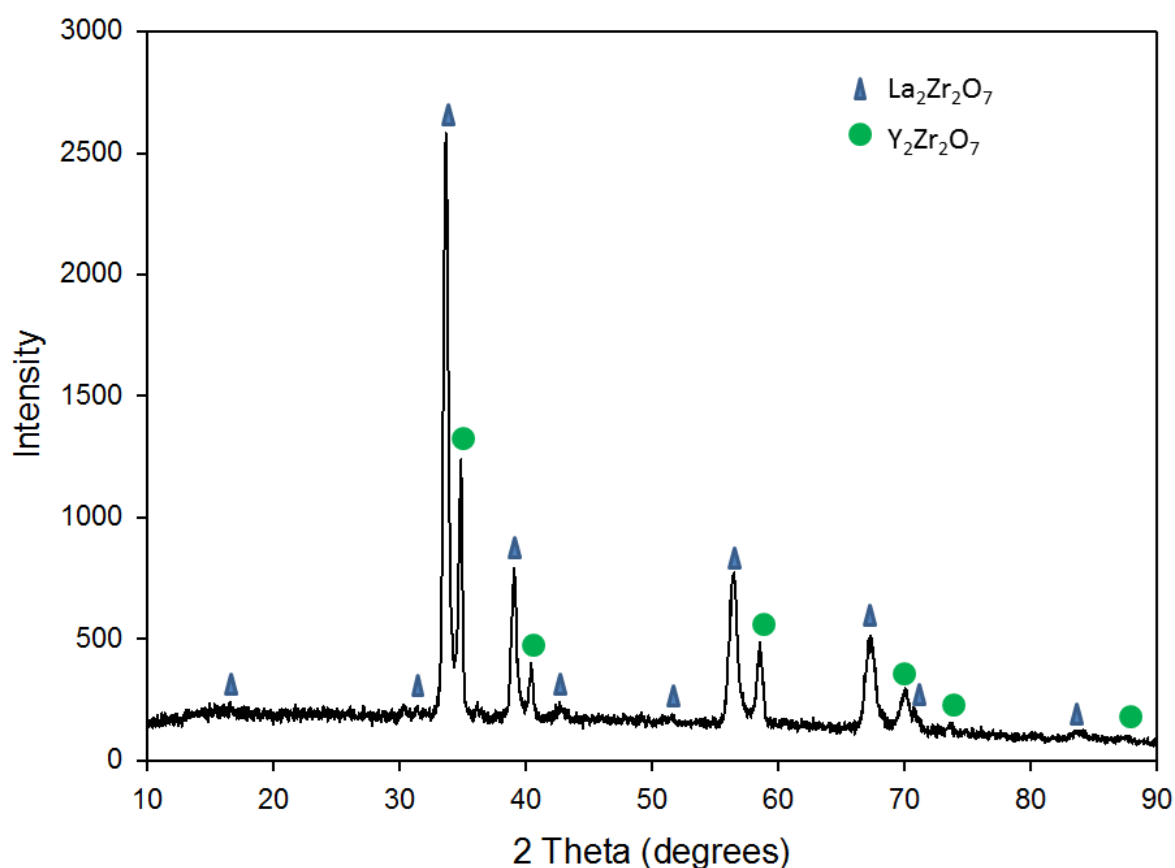


Figure 5.7: PXRD pattern of  $\text{LaYZr}_2\text{O}_7$  after annealing at 1200 °C.

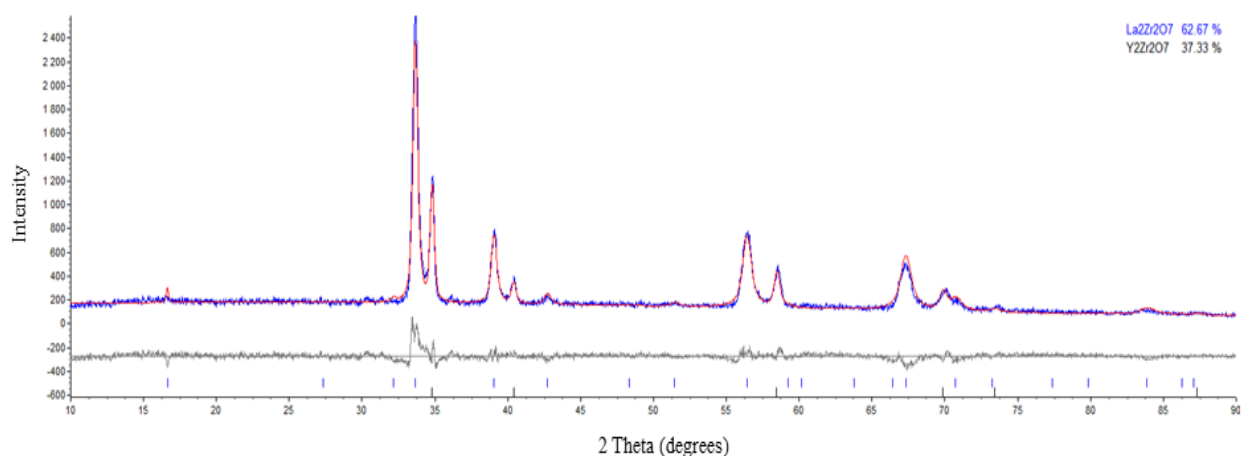


Figure 5.8: Rietveld refinement profile of  $\text{LaYZr}_2\text{O}_7$  annealed at 1200 °C,  $R_{wp} = 10.99\%$ .

The last material that was synthesized for the doped analogues was  $\text{SmYZr}_2\text{O}_7$ , a composition that has not been extensively studied. This composition was the most interesting of all the products because of the A:B ratio it possess. The average A:B ratio of this composition was

found to 1.46, which according to Minervini *et.al* is the lower limit in the stability phase of pyrochlores, any value below 1.46 suggests the mixed metal oxide has a defect fluorite phase. This therefore meant that the material would have a defect fluorite phase as the most dominant phase; this is shown in Figure 5.10. The absence of superlattice peaks is an indication that there was no doubling of the lattice parameter, therefore this was expected to be approximately 5 Å thus further implying that the A and B cations ( $\text{Sm}^{3+}$ ,  $\text{Y}^{3+}$  and  $\text{Zr}^{4+}$ ) were disordered. The structure was refined using Rietveld and from this the lattice parameter was calculated as 5.233 Å which is an acceptable value for defect fluorite type structures.

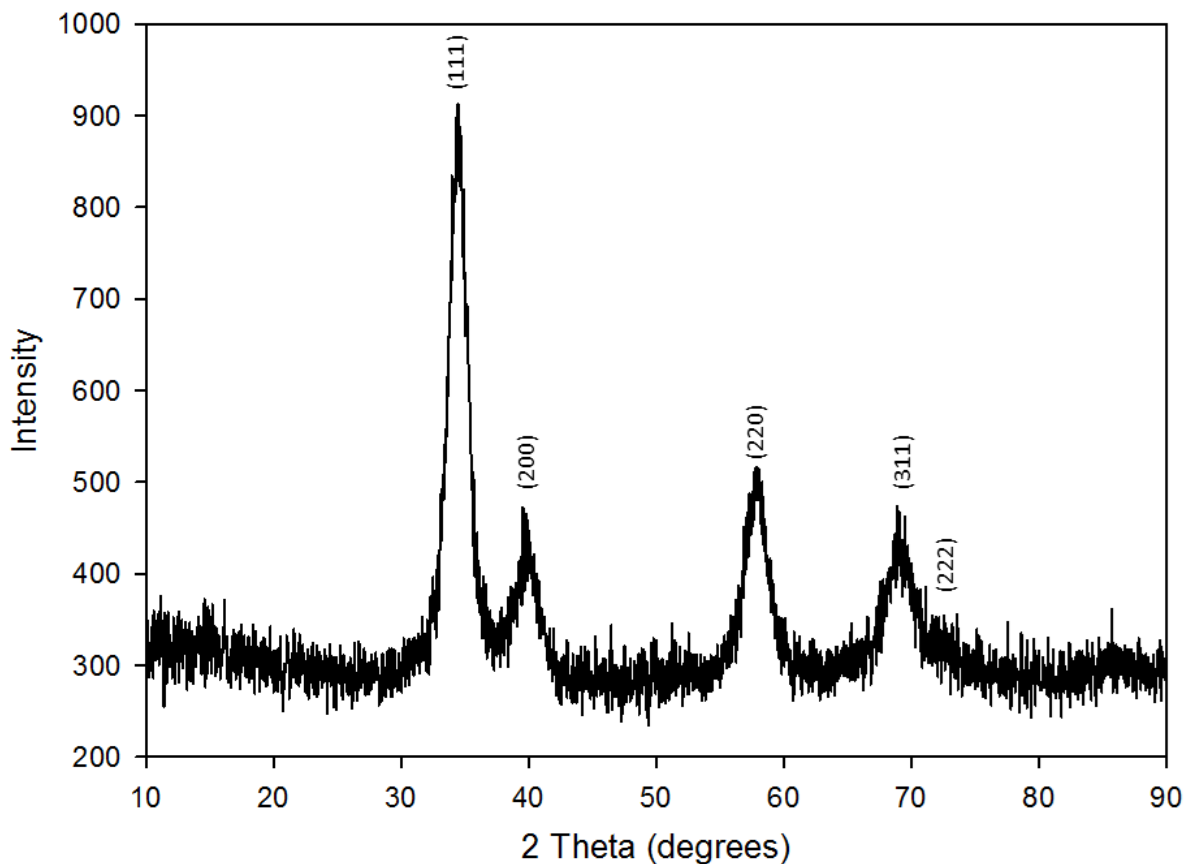


Figure 5.9: PXRD pattern of  $\text{SmYZr}_2\text{O}_7$  calcined at 900 °C.

Table 5.3: Structural model of  $\text{SmYZr}_2\text{O}_7$  as a defect fluorite.

Site	Wyckoff position	x	y	z
Sm	4a	0.000	0.000	0.000
Y	4a	0.000	0.000	0.000
Zr	4a	0.000	0.000	0.000
O	8c	0.250	0.250	0.250

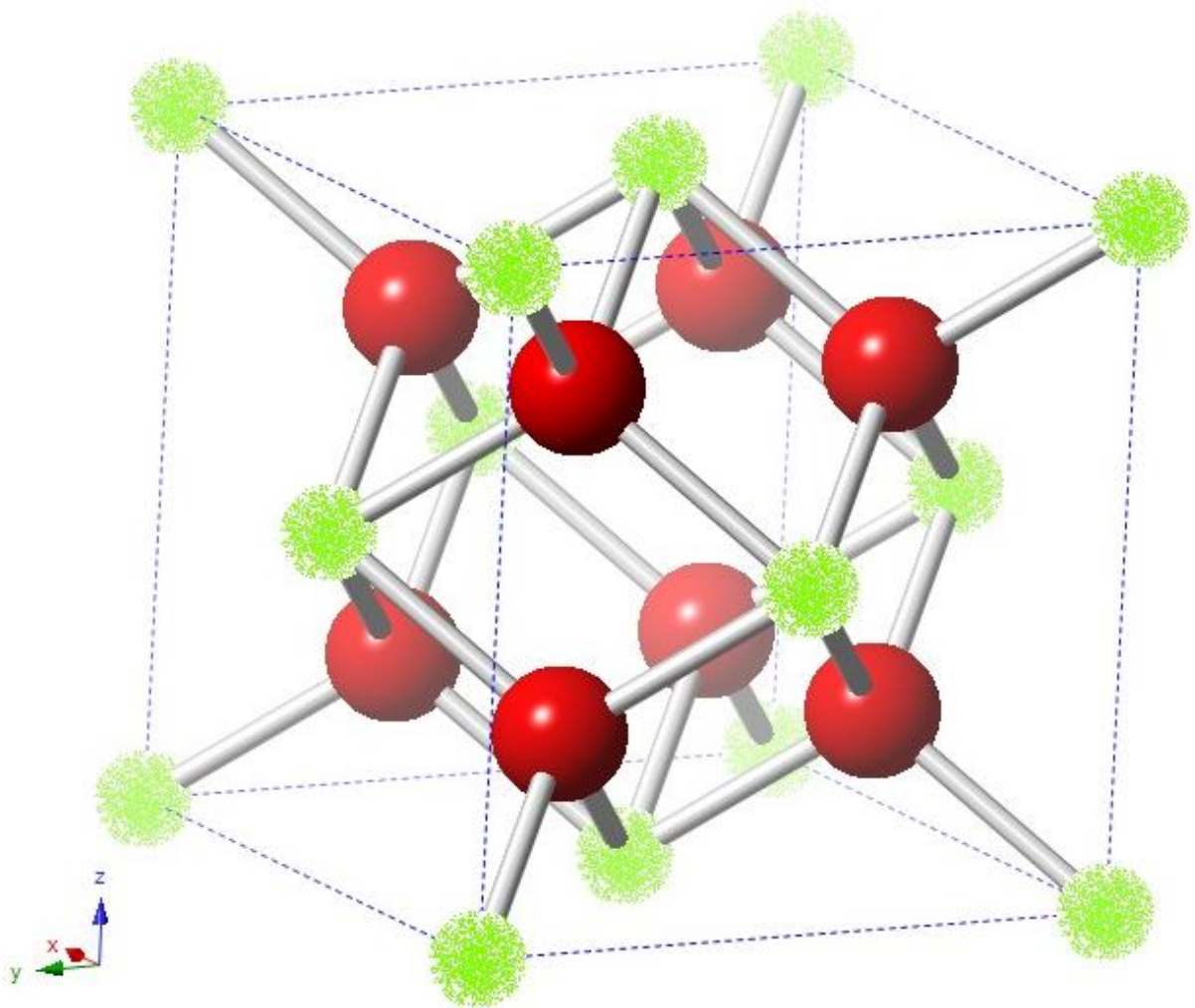


Figure 5.10: Structural model of  $\text{SmYZr}_2\text{O}_7$  showing the unit cell and bonding of the atoms. Oxygen (red) and Sm, Y and Zr (green randomly filled sphere).

The structural model used for defect fluorites suggests that all the cations ( $\text{Sm}^{3+}$ ,  $\text{Y}^{3+}$  and  $\text{Zr}^{4+}$ ) share a special Wyckoff positions with the x, y and z fractional coordinates being 0.000 as shown in Table 5.3. This means that the structure only has two Wyckoff positions namely 4a (accommodates the cations) and 8c (accommodates the oxide ions). This is further shown in Figure 5.11 which shows the structure of  $\text{SmYZr}_2\text{O}_7$ ; the green randomly filled spheres on the Figure represent the 4a position which is the position for  $\text{Sm}^{3+}$ ,  $\text{Y}^{3+}$  and  $\text{Zr}^{4+}$ . Defect fluorite type structures only have one parameter that can be refined and that is the lattice parameter, unlike pyrochlore type structures which have the 48f positional parameter of the oxygen anion which is another parameter that can be refined. Defect fluorite type structures are disordered because of the randomly distributed cations, therefore at high temperatures there are no further transitions that occur in these materials.

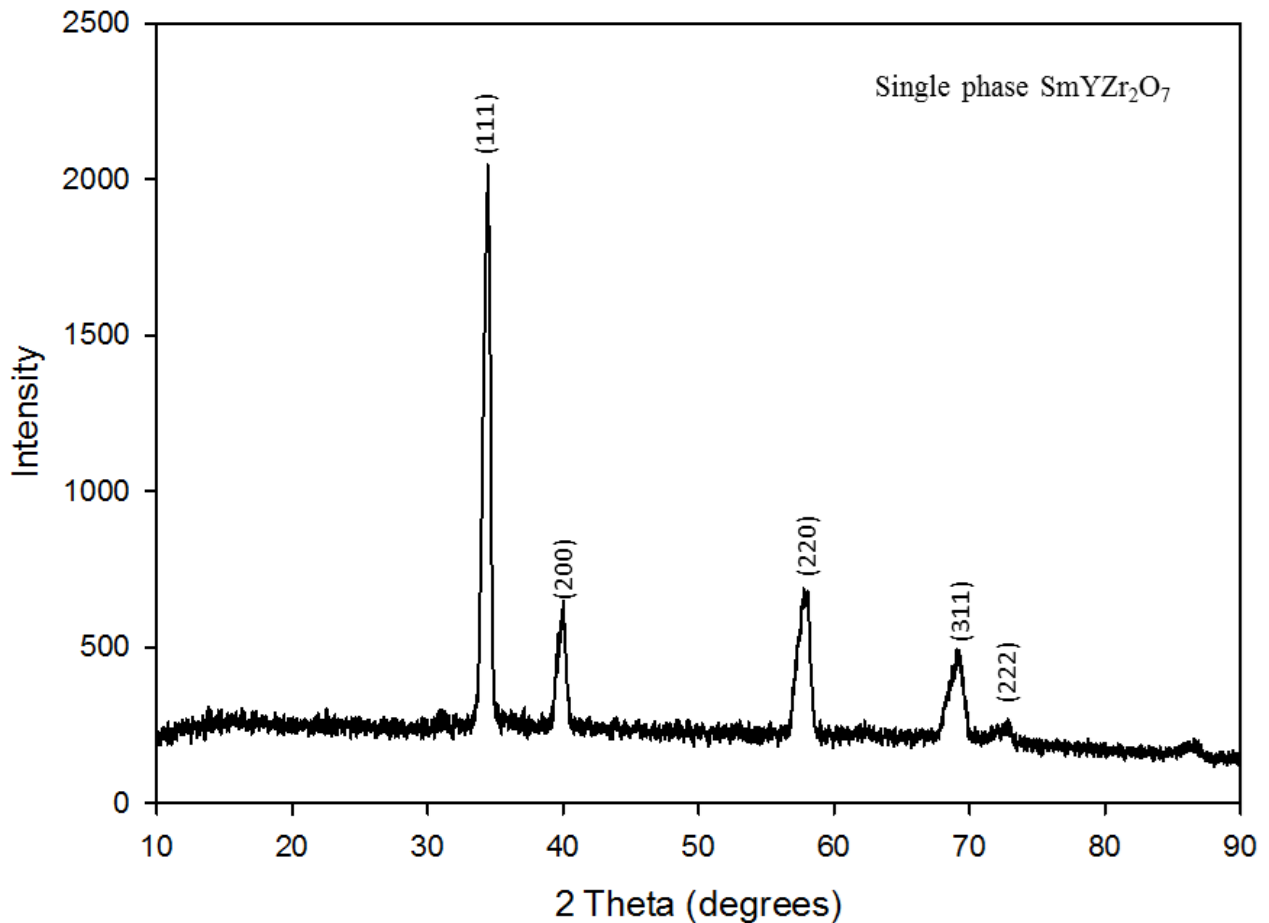


Figure 5.11: PXRD pattern of single phase  $\text{SmYZr}_2\text{O}_7$  after annealing at 1200 °C.

SmYZr<sub>2</sub>O<sub>7</sub> proved to be the most thermally stable analogue and this is shown in Figure 5.11, after the material was annealed at 1200 °C it resulted in a single phase. This is different as compared to LaYZr<sub>2</sub>O<sub>7</sub> and SmLaZr<sub>2</sub>O<sub>7</sub>. The material was still a defect fluorite and this is shown by the five peaks that represent defect fluorites and these are; (111), (200), (220), (311) and (222). The peaks as shown were indexed using a cubic defect fluorite structure with the space group Fm-3m (No. 225) and this was a good match, further verifications were done using Rietveld refinement and this also resulted in a good match. The Rietveld refinement profile is shown in Figure 5.12.

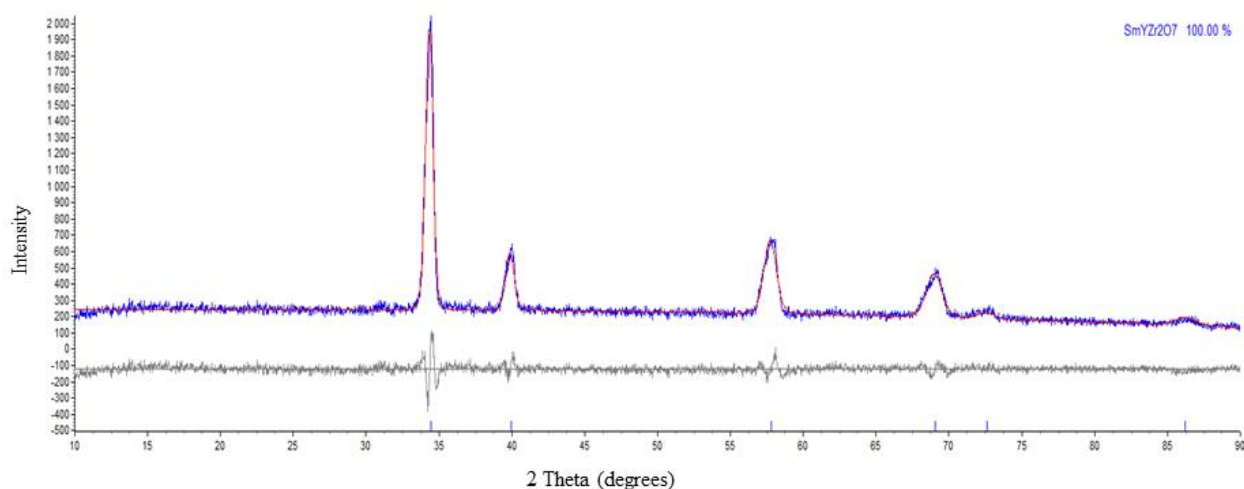


Figure 5.12: Rietveld refinement profile of SmYZr<sub>2</sub>O<sub>7</sub> annealed at 1200 °C, Rwp = 8.016% and a = 5.234 Å.

The SmYZr<sub>2</sub>O<sub>7</sub> phase after annealing at 1200 °C was pure, as mentioned earlier. Rietveld refinement showed that the material was 100% SmYZr<sub>2</sub>O<sub>7</sub>. There are no reports of SmYZr<sub>2</sub>O<sub>7</sub> as a defect fluorite in literature and therefore this was the first study conducted that shows that SmYZr<sub>2</sub>O<sub>7</sub> is indeed a defect fluorite where Sm, Y, and Zr share a Wyckoff position. The Rwp value was acceptable as shown on the legend of Figure 5.12 as 8.016%.

Due to the fact that the material was novel a further investigation was done to determine that lattice thermal expansion coefficient, this was done using the Bruker D8 recorded from 303 K to 1053 K. The angle ranged from  $2\theta = 20^\circ$  to  $110^\circ$  using cobalt (Co) radiation. The variable temperature PXRD pattern of SmYZr<sub>2</sub>O<sub>7</sub> is shown in Figure 5.14. The Figure shows that the peaks shift to lower angles as the temperature increases which are indicative of thermal expansion due to the interplanar spacing increasing.

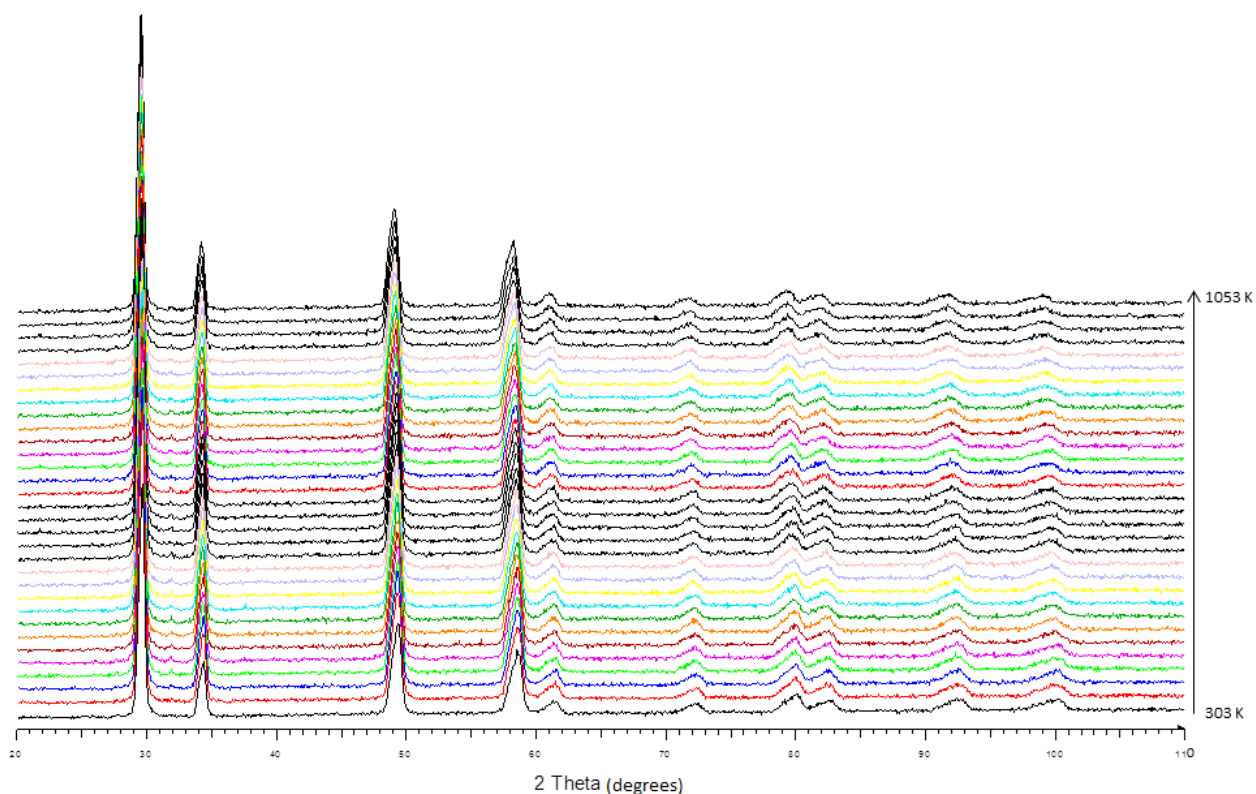


Figure 5.14: Variable temperatures PXRD pattern of  $\text{SmYZr}_2\text{O}_7$  from 303 K to 1053 K.

For further clarification the peaks that represent (311) and (222) were zoomed in to show that there was an expansion of the lattice parameter, this is shown in Figure 5.14. From the Figure it is evident that as the temperature increases the peaks shift to the left, thus indicating that there is lattice thermal expansion. Two peaks; one at  $2\theta \approx 58.5^\circ$  (311) and the other at  $2\theta \approx 61.5^\circ$  (222) were zoomed in for a better clarity that peaks were indeed shifting to the left as the temperature increases, this is shown in Figure 5.15.

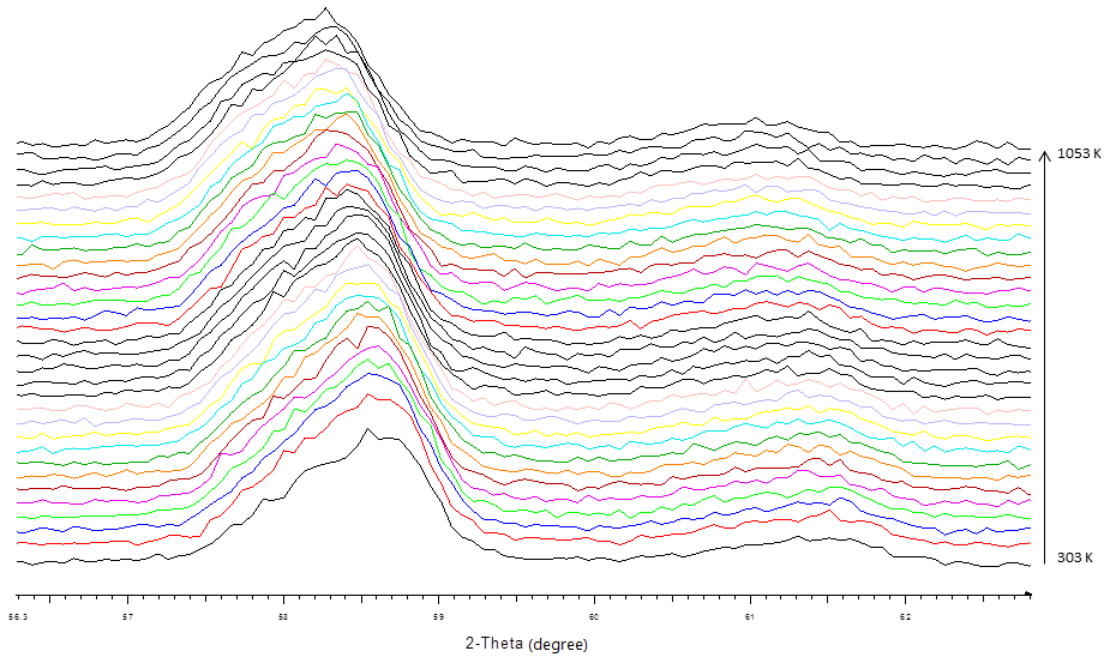


Figure 5.14: Variable temperature PXRD pattern showing (311) and (222) peaks.

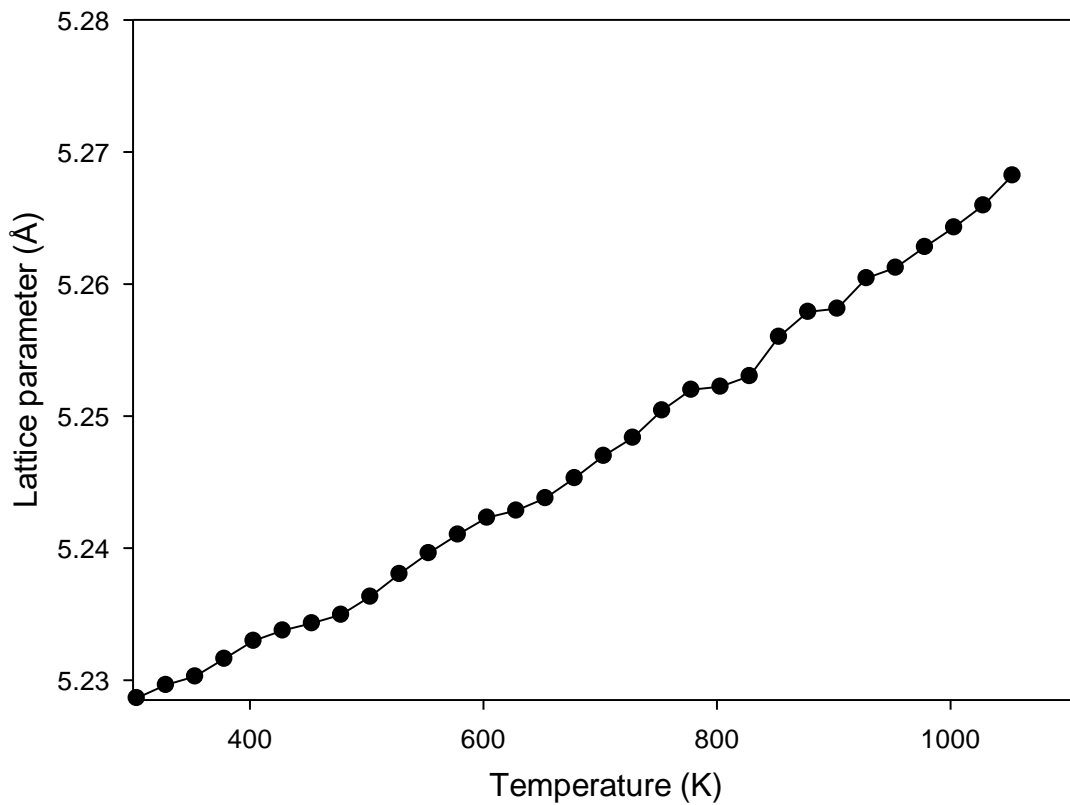


Figure 5.15: Lattice parameter obtained by Rietveld refinement as a function of temperature plot for  $\text{SmYZr}_2\text{O}_7$ .

To calculate lattice thermal expansion coefficient the equation below was used;

$$\alpha = \frac{1}{a_{303}} \left( \frac{\partial a}{\partial T} \right) \quad (5.1)$$

A graph of lattice parameter as a function of temperature is plotted (Figure 5.16); from this the slope is calculated and then used in equation 5.1. The calculated thermal expansion for SmYZr<sub>2</sub>O<sub>7</sub> was found to be 10.08 x 10<sup>-6</sup> K<sup>-1</sup>. The value calculated was in good agreement with the values of Sm<sub>2</sub>Zr<sub>2</sub>O<sub>7</sub> and Y<sub>2</sub>Zr<sub>2</sub>O<sub>7</sub> as seen in literature. Sm<sub>2</sub>Zr<sub>2</sub>O<sub>7</sub> exists as a pyrochlore type structure and the coefficient of thermal expansion for this material lies between 10-11 x 10<sup>-6</sup> K<sup>-1</sup> as calculated by Kutty *et.al*<sup>6</sup>. Y<sub>2</sub>Zr<sub>2</sub>O<sub>7</sub> on the other side exists as a defect fluorite and this implies that the thermal expansion of this material should be similar to that of yttria stabilized zirconia (YSZ). The coefficient of thermal expansion for YSZ as calculated by Yamashita *et.al* ranges between 7.37-11.75 x 10<sup>-6</sup> K<sup>-1</sup> respectively<sup>7</sup>. Therefore the calculated thermal expansion coefficient from this study lies in the range of the values found in literature and this is the first report of TEC for SmYZr<sub>2</sub>O<sub>7</sub>.

### 5.3.2 Mapping studies

The electron probe micro-analyzer (EPMA) was used for mapping studies. This was done to determine how each of the cations is distributed on a chosen crystal. This is a useful tool in determining whether the material synthesized was a solid solution or a mixture of two phases. The first material that was analyzed was LaSmZr<sub>2</sub>O<sub>7</sub> (Figure 5.16), from the Figure there are different elements that were mapped in one crystal. The first image shows the crystal of LaSmZr<sub>2</sub>O<sub>7</sub> that was to be mapped. Lanthanum (La) atoms were mapped first and from the second crystal it is evident that La was not evenly distributed on the crystal of interest, the La map is seen as the green part of the crystal. La was concentrated on certain regions of the crystal and this is indicative of non-homogeneity, the same thing applies for samarium (Sm) which is also concentrated at specific regions. Zirconium (Zr) was the only atom that was evenly distributed throughout the chosen crystal shown in blue on the last image. As the material was fired at 1200 °C it was evident that there were two phases present in the material (Figure 5.3), this then confirms that the material was indeed a mixture of La<sub>2</sub>Zr<sub>2</sub>O<sub>7</sub> and Sm<sub>2</sub>Zr<sub>2</sub>O<sub>7</sub>. Ambient temperature PXRD techniques however are not good in distinguishing between two phases especially when they share 2θ angles. La<sub>2</sub>Zr<sub>2</sub>O<sub>7</sub> and Sm<sub>2</sub>Zr<sub>2</sub>O<sub>7</sub> both have a pyrochlore superstructure, therefore they share similar superlattice peaks and this inhibits any differences that can be seen when using room temperature PXRD techniques.

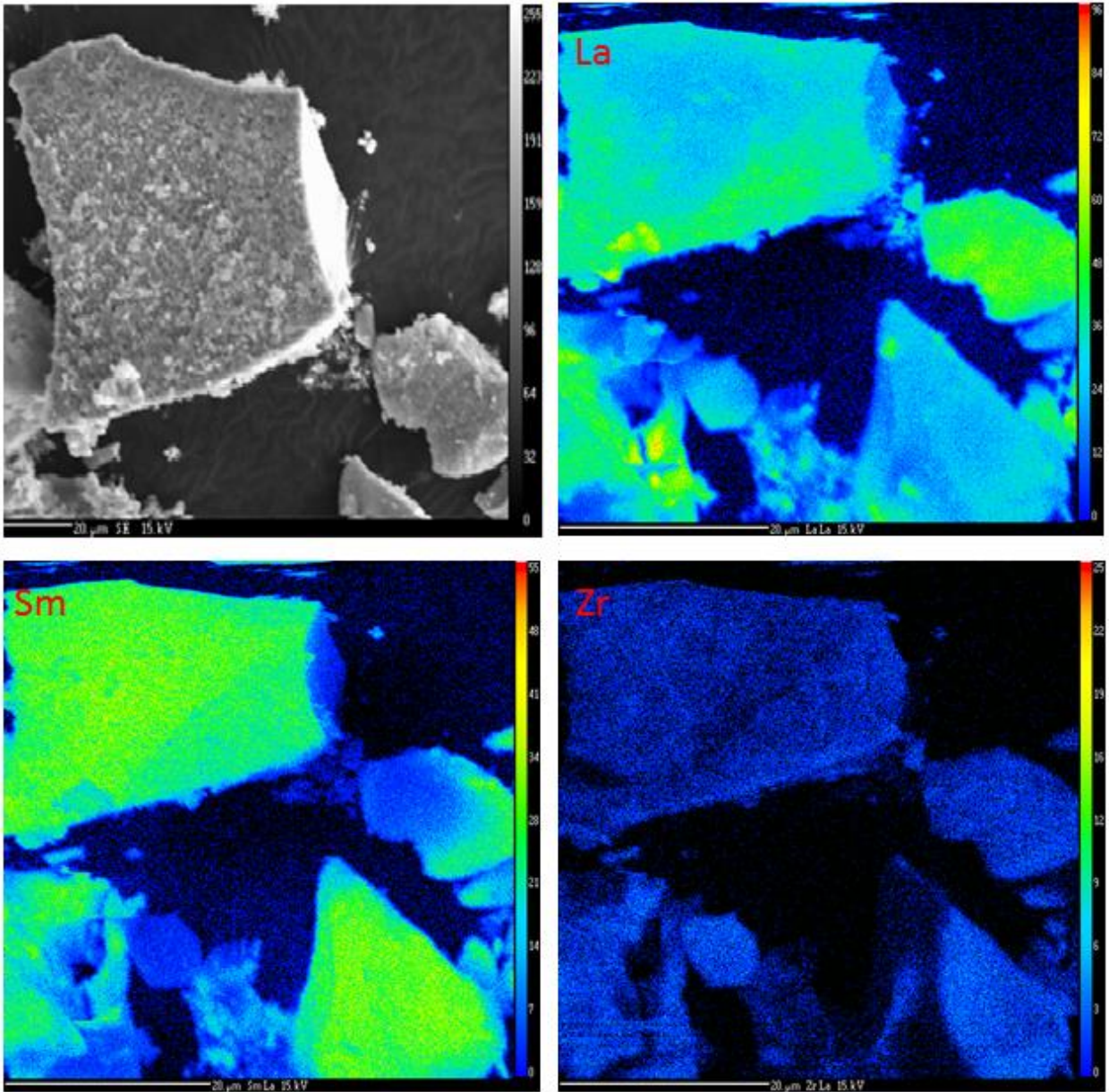


Figure 5.16: Elemental maps for a chosen crystal of  $\text{LaSmZr}_2\text{O}_7$  structure.

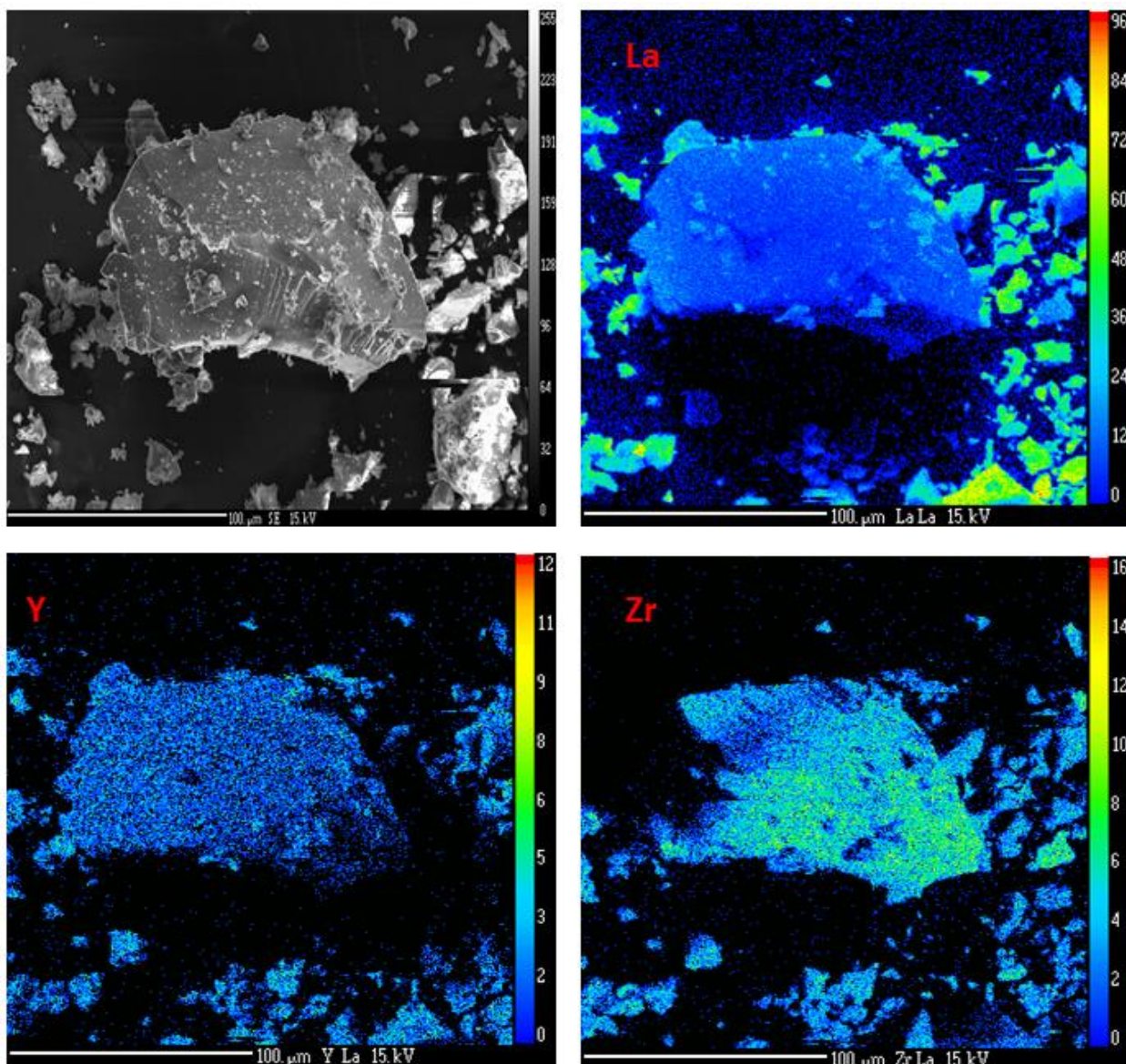


Figure 5.17: Elemental maps for a chosen crystal of  $\text{LaYZr}_2\text{O}_7$  pyrochlore.

$\text{LaYZr}_2\text{O}_7$  was considered a solution after an ambient temperature PXRD analysis as there were only single and distinct peaks on the measured pattern (Figure 5.5). When the elemental maps were measured (Figure 5.17) it was discovered that some of the elements were not evenly distributed throughout the chosen crystal. When examining Figure 5.18 it is evident that the lanthanum (La) map indicated that La atoms were in specific regions, this is visualized by the lime green colour on the smaller crystals around the major one. Yttrium (Y) was more evenly distributed as compared to La; however, there were still regions where Y is absent thus suggesting that there were La rich sites and Y rich sites. This is indicative of uneven distribution of the atoms of interest which means that there were two phases present and these were  $\text{La}_2\text{Zr}_2\text{O}_7$  and  $\text{Y}_2\text{Zr}_2\text{O}_7$  respectively. This supports Figure 5.7 which shows

that as the material was fired at 1200 °C it separated into the primary pyrochlore structures.

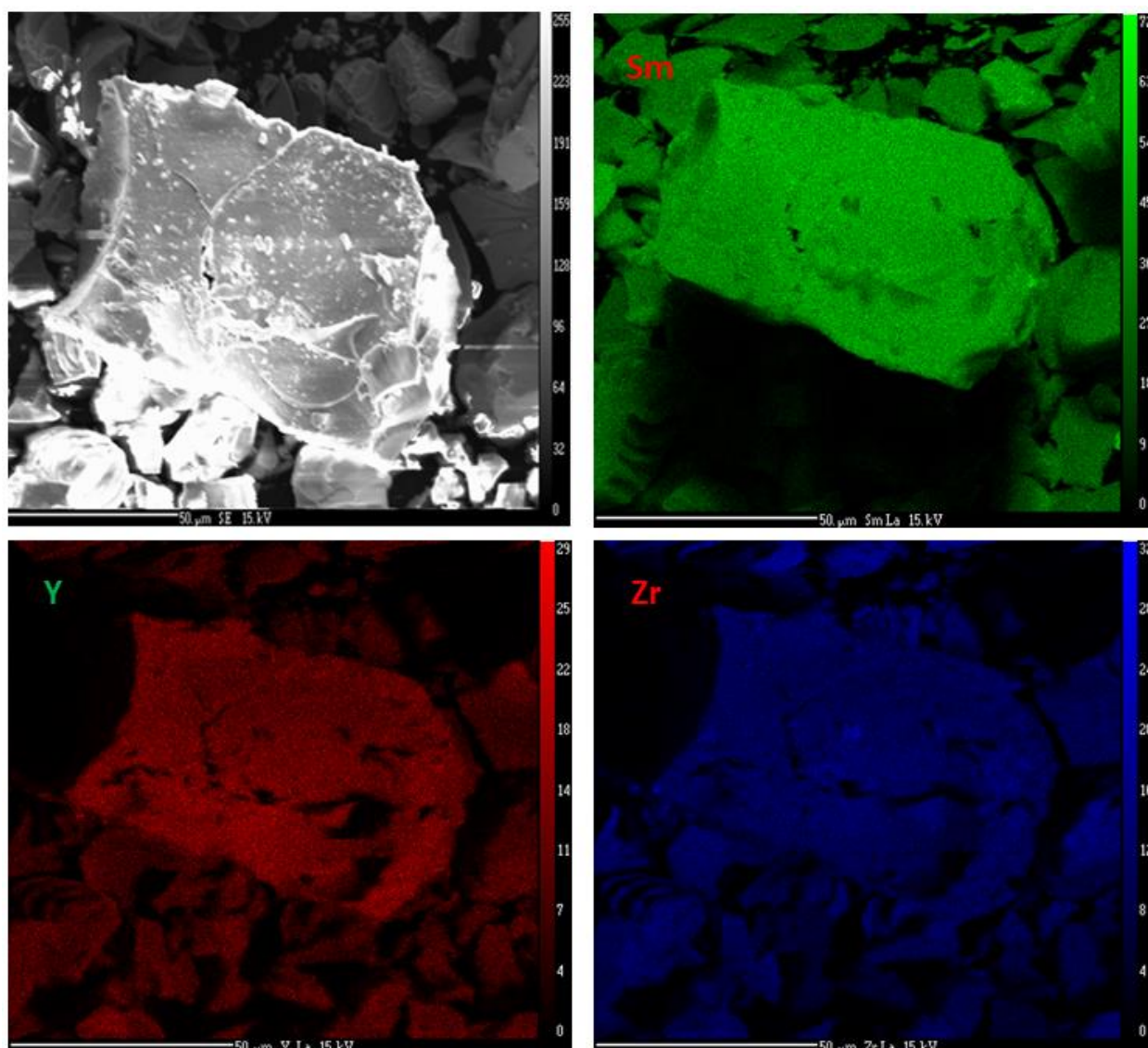


Figure 5.18: Elemental maps for a chosen crystal of  $\text{SmYZr}_2\text{O}_7$ .

$\text{SmYZr}_2\text{O}_7$  was found to be the only material that has a single phase even when fired at 1200 °C. The elemental map of this material supported data analysed from PXRD which suggested that the material was a single phase of  $\text{SmYZr}_2\text{O}_7$ . From Figure 5.18 it is shown that a Sm map (in green) had an even distribution of the atom, instead of having the atom agglomerate at specific sites. The same thing applies for Y atoms (in red) which are also evenly distributed on the chosen crystal and therefore this proves beyond reasonable doubt that  $\text{SmYZr}_2\text{O}_7$  was indeed a single phase and was the most stable of all the doped analogues that were synthesized. This then makes  $\text{SmYZr}_2\text{O}_7$  a novel material as it has not been synthesized before and such data does not exist in literature. Besides the map of the trivalent cations

(Sm<sup>3+</sup> and Y<sup>3+</sup>), a map for the tetravalent cation (Zr<sup>4+</sup>) was also obtained and this shows that Zr atoms are also evenly distributed in the chosen crystal.

## 5.4 General conclusions

Doped analogues of the pyrozoirconate class were synthesized using the sol-gel method. These were all characterized with PXRD before and after annealing. LaSmZr<sub>2</sub>O<sub>7</sub> and LaYZr<sub>2</sub>O<sub>7</sub> were the least stable materials, this was seen by annealing them at 1200 °C and they disintegrated into the primary pyrozoirconates implying that they were a mixture instead of being a solid solution. The two materials that were unstable also proved to be a mixture by looking at the mapping studies which showed that the cations were not evenly distributed. Amongst the three products SmYZr<sub>2</sub>O<sub>7</sub> showed the most thermal stability as it had peaks that showed a single phase even after annealing at 1200 °C. For the first time since the synthesis of doped analogues of pyrozoirconates we see a stable phase of SmYZr<sub>2</sub>O<sub>7</sub> with a defect fluorite structure type, this material was mapped for the first time and this is shown by the EPMA study and from this it was seen that the cations were all evenly distributed. This implies that this material can be useful in solid oxide fuel cells and the fact that it possesses a defect fluorite structure type would make it an ideal electrolyte. The thermal expansion coefficient was calculated and this value was good in the sense that it lies between the TEC's of both Sm<sub>2</sub>Zr<sub>2</sub>O<sub>7</sub> and Y<sub>2</sub>Zr<sub>2</sub>O<sub>7</sub>.

## 5.5 References

1. Subramanian M. A., Aravamuda G., and Subba Rao G. V., *Progress in solid state chemistry*, 1983, 15, 2, 55-143.
2. Payne J. L., PhD Thesis, Durham University, 2011.
3. Minervini L, and Grimes R. W., *Journal of the American Ceramic Society*, 2000, 83, 1873.
4. Lui Z-G., Ouyang J-H., Zhou Y., Xiang J., and Liu X-M., *Materials and Design*, 2011, 32, 4201–4206,
5. Whittle K. R., Cranswick L. M. D., Redfern S. A. T., Swainson I. P., and Lumpkin G. R., *Journal of Solid State Chemistry*, 2009, 182, pp. 442-450.
6. Kutty K. V. G., Rajagopalan S., Mathews C. K. and Varadaraju U. V., *Materials Research Bulletin*, 1994, 29, 7, 759-766.

## Chapter 6

### Conclusions and future work

#### 6.1 Conclusions

The main aims and objectives of the project were to:

- Synthesize  $\text{La}_2\text{Zr}_2\text{O}_7$ ,  $\text{Sm}_2\text{Zr}_2\text{O}_7$  and  $\text{Y}_2\text{Zr}_2\text{O}_7$  using sol-gel synthesis, followed by a thoroughly Reitveld refinement of the materials and study their thermoresponsive behaviour which helps determine the thermal expansion coefficient.
- Synthesize  $\text{La}_2\text{Zr}_2\text{O}_7$  using the wet mechanochemical route in a planetary ball mill equipped with a stainless steel pot.
- Synthesize doped analogues of the zirconates ( $\text{LaSmZr}_2\text{O}_7$ ,  $\text{LaYZr}_2\text{O}_7$  and  $\text{SmYZr}_2\text{O}_7$ ) using the sol-gel method, refine the structures using Rietveld refinement and get elemental maps of the final products to determine whether single solutions or a mixture of materials formed part of the product.

All the products were characterised using powder X-ray diffraction (PXRD), Rietveld refinement and high temperature PXRD. Elemental maps were only done with the doped analogues.

Chapter 3 investigated the thermoresponsive behaviour of  $\text{La}_2\text{Zr}_2\text{O}_7$ ,  $\text{Sm}_2\text{Zr}_2\text{O}_7$  and  $\text{Y}_2\text{Zr}_2\text{O}_7$  which were all synthesized using the sol-gel method. The findings were that all the materials were homogenous mixtures and when characterized using Rietveld refinement the conclusion was that the final products were phase pure. A further investigation was on the thermal coefficient of the materials and the findings were that all the materials had low thermal expansion coefficients. One of the most important findings from this chapter was the effect of the ionic size of the A atoms to the thermal expansion coefficient. The thermal expansion coefficient in these pyrochlore zirconates decreased with decreasing ionic size, the ions arranged in terms of decreasing ionic radii are as follows;  $\text{La}^{3+} > \text{Sm}^{3+} > \text{Y}^{3+}$ . And the observation was that  $\text{La}_2\text{Zr}_2\text{O}_7$  had the highest thermal expansion coefficient while  $\text{Y}_2\text{Zr}_2\text{O}_7$  had the lowest TEC.

Chapter 4 investigated the synthesis of  $\text{La}_2\text{Zr}_2\text{O}_7$  using the wet mechanochemical method. This has been done before using a zirconia pot; in this project a stainless steel pot was used. The product was analysed using PXRD before annealing at  $1200\text{ }^\circ\text{C}$ , this was impure and had the starting materials;  $\text{La}_2\text{O}_3$  and  $\text{ZrO}_2$ . Another interesting impurity was  $\text{La}(\text{OH})_3$ , this was identified on the PXRD pattern. The presence of  $\text{La}(\text{OH})_3$  was due to the hygroscopic behaviour of  $\text{La}_2\text{O}_3$ . The product was then analysed with PXRD after annealing and a phase of  $\text{La}_2\text{Zr}_2\text{O}_7$  was present but this was not pure. There were still traces of the starting materials, another phase was present in the final product and this was  $\text{LaFeO}_3$ . This was due to  $\text{La}_2\text{O}_3$  reacting with Fe that was part of the stainless steel pot. This was an interesting observation as it had not been documented before. A quantitative study using Rietveld refinement then followed to determine how much of the Fe was removed from the stainless steel and this was found to 0.1388 g. The material had a high thermal expansion coefficient and this was due to the presence of the impurities, these introduce disorder on the crystal structure of  $\text{La}_2\text{Zr}_2\text{O}_7$ .

In chapter 5 doped analogues of the zirconate pyrochlores were synthesized using the sol-gel method. All the products ( $\text{LaSmZr}_2\text{O}_7$ ,  $\text{LaYZr}_2\text{O}_7$  and  $\text{SmYZr}_2\text{O}_7$ ) were pure phases before annealing at  $1200\text{ }^\circ\text{C}$ .  $\text{LaSmZr}_2\text{O}_7$  and  $\text{LaYZr}_2\text{O}_7$  were unstable after annealing at  $1200\text{ }^\circ\text{C}$  and this was shown by the PXRD patterns of the materials.  $\text{SmYZr}_2\text{O}_7$  was the only material that was stable at the fore-mentioned temperature and this was shown by a phase pure PXRD pattern. The materials were analysed using Rietveld refinement and this confirmed the PXRD results. The phase pure  $\text{SmYZr}_2\text{O}_7$  was further analysed using variable temperature PXRD to study the thermoresponsive behaviour and determine the thermal expansion coefficient, the TEC of this material was between that of  $\text{Sm}_2\text{Zr}_2\text{O}_7$  and  $\text{Y}_2\text{Zr}_2\text{O}_7$ . This was the first report of TEC for  $\text{SmYZr}_2\text{O}_7$ . A study of elemental distribution of crystals of the final products followed using EPMA and this confirmed that  $\text{SmYZr}_2\text{O}_7$  was a solid solution while  $\text{LaSmZr}_2\text{O}_7$  and  $\text{LaYZr}_2\text{O}_7$  were mixtures.

## 6.2 Future work

The materials synthesized in this project find uses as electrolytes in solid oxide fuel cells. Studies on the ion conductivity of the materials would help in determining which material is the best between the pure zirconates and the doped analogues using impedance spectroscopy. This would then be followed by designing a proof-of-concept solid oxide fuel cell. It is recommended that the synthesis of zirconates using the mechanochemical method

be done using a zirconia pot instead of a stainless steel one so that the final product has no impurities as this was demonstrated in this research project. It would also be useful to synthesize some of the zirconates using mechanochemical route and compare their thermal expansion coefficients in order to determine if the synthetic route has effects on the structure. Another future recommendation would be to do a sequential study of doped zirconates to determine the exact temperature at which they become unstable.